Title
A Study of the Head Disk Interface in Heat Assisted Magnetic Recording - Energy and Mass Transfer in Nanoscale

Author
Wu, Haoyu

Publication Date
2018

Peer reviewed|Thesis/dissertation

A Study of the Head Disk Interface in Heat Assisted Magnetic Recording - Energy and Mass Transfer in Nanoscale

by

Haoyu Wu

A dissertation submitted in partial satisfaction of the
requirements for the degree of
Doctor of Philosophy

in

Engineering - Mechanical Engineering

in the

Graduate Division

of the

University of California, Berkeley

Committee in charge:

Professor David B. Bogy, Chair
Professor Eli Yablonovitch
Professor Oliver O'Reilly

Summer 2018

A Study of the Head Disk Interface in Heat Assisted Magnetic Recording - Energy and Mass Transfer in Nanoscale

Abstract

A Study of the Head Disk Interface in Heat Assisted Magnetic Recording - Energy and Mass Transfer in Nanoscale

by

Haoyu Wu

Doctor of Philosophy in Engineering - Mechanical Engineering

University of California, Berkeley

Professor David B. Bogy, Chair

The hard disk drive (HDD) is still the dominant technology in digital data storage due to its cost efficiency and long term reliability compared with other forms of data storage devices. The HDDs are widely used in personal computing, gaming devices, cloud services, data centers, surveillance, etc. Because the superparamagnetic limit of perpendicular magnetic recording (PMR) has been reached at the data density of about $1\,\mathrm{Tb/in^2}$, heat assisted magnetic recording (HAMR) is being pursued and is expected to help increase the areal density to over $10\,\mathrm{Tb/in^2}$ in HDDs in order to fulfill the future worldwide data storage demands.

In HAMR, the magnetic media is heated locally ($\sim$50 nm $\times$ 50 nm) and momentarily ($\sim$ 10 ns) to its Curie temperature ($\sim$750 K) by a laser beam. The laser beam is generated by a laser diode (LD) and focused by a near field transducer (NFT). But the energy and mass transfer at high temperature from the laser heating can cause potential reliability issues. The design temperature of the NFT is much lower than the media's Curie temperature. However, the distance between the NFT and the media is less than 10 nm. As a result, the heat can flow back from the media to the NFT, which is called the back-heating effect. This can cause undesired additional temperature increase on the NFT, shortening its lifetime. Additionally, depletion, evaporation and degradation can happen on the lubricant and the carbon overcoat (COC) layer of the media. The material can transfer from the media to the head at high temperature and cause solid contamination on the head, adversely affecting its reliability.

Since the laser heating in HAMR happens at nanoscale spatially and temporally, it is difficult to measure experimentally. In this dissertation, a comprehensive experimental stage, called the Computer Mechanics Laboratory (CML)-HAMR stage, was built to study different aspects of HAMR systems, including the heat and mass transfer in the head-disk interface during laser heating. The CML-HAMR stage includes an optical module, a spinstand module and a signal generation/acquisition module. And it can emulate the HAMR scenario.

The head's temperature was measured during the laser heating using the stage and heads with an embedded contact sensor (ECS). It was estimated, based on a linear extrapolation, that the ECS temperature rise is 139 K, 132 K, 127 K and 122 K when the disk is heated to the Curie temperature (∼750 K) and the head-disk clearance is 0 nm, 1 nm, 2 nm and 3 nm, respectively. The heating effect of the ECS was also studied and a related heat transfer experiment was performed. The normalized ECS self heating temperature rise, an indicator of the heat transfer in the head-disk interface (HDI), was measured. It was concluded that the heat transfer coefficient across the HDI strongly depends on the width of the gap size, especially when the gap size is smaller than 1 nm.

The head disk interaction during the laser heating was studied using a waveguide head, i.e., a HAMR head without the NFT. It showed that the laser heating can cause head surface protrusion. This lowers the fly-height (FH) and results in early touchdown (TD). It was shown that the ratio of touchdown power (TDP) change to the laser current is 0.3 mW/mA. The dynamics of the head also changes during the laser heating. It was found that the magnitude of the 1st-pitch-mode vibration on the head increases over time both in short term and long term. The accumulation of material transferred to the head was also investigated. It was found that the solid contamination caused by the laser heating forms in the center of the waveguide. The round-shaped contamination formed on the head surface after laser heating.

Finally the disk lubricant reflow after laser heating was studied. In the experiment, a beam of free space laser shines on the rotating disk at different laser powers, disk rotating speeds and repetitions. Then the disk was examined by an optical surface analyzer (OSA). It was found that 80% of the displaced lubricant recovers within 20 minutes. A simulation was also performed. The experiments and the simulation are in good agreement.

To my son Lucas

Contents

List of Figures

List of Tables

Acronyms

ABS air bearing surface. iv, 3, 87

AE acoustic emission. v, 21, 89

AFM atomic force microscope. vi, 46, 89

AI analog input. 40

AO analog output. 40

ASTC Advanced Storage Technology Consortium. xii

CML Computer Mechanics Laboratory. 1, 16, 87

CMR conventional magnet recording. 16

COC carbon overcoat. 1, 3, 89

DAQ data acquisition. 40

ECS embedded contact sensor. 2, 16, 18, 21, 87

EM electromagnetic. 13, 27

FDTD finite-difference time-domain. 28

FH fly-height. 2, 4, 87

FPGA field-programmable gate array. 35

FWHM full-width-half-maximum. 28, 88

HAMR heat assisted magnetic recording. 1, 12, 87

HDD hard disk drive. 1, 87

HDI head-disk interface. 2, 4, 87

HGA head gimbal assembly. iv, 3

HMS head-media spacing. iv, 6

LD laser diode. 1, 13, 27, 87

LE leading edge. 3

LPDS laser power delivery system. 16, 18, 27, 87

NFT near field transducer. 1, 13, 27, 87

OSA optical surface analyzer. 2, 82

PMR perpendicular magnetic recording. 1, 3

PSIM planar solid immersion mirror. 27

R/W read-write. 20

RAMAC Random Access Memory Accounting. 7

RMS root-mean-squared. vii, 65

SMR shingled magnetic recording. 9

SNR signal-to-noise-ratio. 12, 87

SSD solid state drive. 1

STFT short-time Fourier transform. vii, 89

TD touchdown. 2, 21

TDP touchdown power. 2, 21, 88

TE trailing edge. 4

TFC thermal fly-height control. v, 9, 18, 87

TMR tunnel magnetoresistance. 4

VCM voice coil motor. 1

Acknowledgments

First of all, I would like to thank my adviser, Professor David Bogy for guiding and supporting me through my PhD study at UC Berkeley. I am so glad that I had a chance to work and study with him. He is smart and charming, providing me important advice not only in study but also in life. His sharp opinions about academia, business, politics and lifestyle always enlighten me. It is my great honor and fortune to have had him as my adviser and mentor.

I would also like to express my appreciation to Professor Oliver O'Reilly and Professor Eli Yablonovitch for their valuable contributions and feedback to my dissertation.

I would like to thank my colleagues in CML. I have really enjoyed the free atmosphere to discuss and learn from each other with different backgrounds. It has been a great pleasure to work with them: Shaomin Xiong, Yung-Kan Chen, Alejandro Rodriguez Mendez, Soroush Sarabi, Yuan Ma, Tholfaqar "Dolf" Mardan, Amin Ghafari Zeydabadi, Siddhesh Sakhalkar, Dr. Bair Budaev, Dr. Yu Wang and Yueqiang Hu. Among them, I would like to especially thank Shaomin Xiong. He directly guided me during my first year study but his support never ended even after his graduation. Every time I struggled in the research, he is always on the other side of the phone. He also give me suggestions in career development which changed my life.

My PhD could not have been completed without the support of the Advanced Storage Technology Consortium (ASTC). Huan Tang from Seagate, Erhard Schreck, Shaomin Xiong, Sripathi Canchi and Robert Smith from Western Digital gave me great suggestions in both big directions of the projects and the technical details. I learned a lot communicating with them.

I would like to thank the TV series of The Big Bang Theory. The show portrays a vivid life of PhDs, which encouraged me to pursue a PhD degree.

I would like to thank my friends at Berkeley: Nan Yang, Changliu Liu, Xingxing Cai, Minghui Zheng, Xiao Liang and Xuance Zhou. You made the life at Berkeley memorable.

I want thank my parents Zepeng Wu and Yi Zhai for giving me life and raising me up. Their unconditional love and support helps me through my 29 years of life.

Finally, I would like to thank my wife Shiying Zhou. Thank you for experiencing the sweetness and bitterness in life with me. I don't know what I will be or where I will be without you. And I am glad I met you. I love you, for my life.

Chapter 1

Introduction

Data is essential to our life. It is generated and stored everyday whenever a photo or a video clip is uploaded to the server or the data center. In fact, it is predicted by the International Data Corporation that the worldwide data amount will be 163 ZB (1 ZB=1×10^{12} GB) in the year of 2025 [1]. There are several types of devices used for digital data storage: magnetic tapes, hard disk drives (HDDs), solid state drives (SSDs), optical disks, etc. Among these devices, the HDDs play the most prominent role mainly due to their reliability and low cost. As of June 2018, the ratio of the per-GB-price of SSD to HDD is still $\sim 10:1$. It is reported that 400 million HDDs were shipped in 2017 [2].

In order to fulfill the worldwide data storage demands, a new technology called heat assisted magnetic recording (HAMR) has been proposed by the HDD industry [3, 4, 5, 6]. In HAMR technology, the recording disk is heated by a laser based heating system such that the writing process is easier. This may help further increasing the capacity of the HDD and lowering the cost. However, a high temperature zone is created in a nanoscale which causes strong energy and mass transfer. This causes reliability issues in HAMR. In this dissertation, experiments were performed to study the energy and mass transfer in the nanoscale.

This chapter serves as an introduction to the dissertation. In Section 1.1, the basics of the HDD and the limitation of the existing technology are discussed. The HAMR technology is introduced in Section 1.2. The issues related to the technology are also addressed. The objective and the organization of this dissertation are presented in Section 1.3.

1.1 Hard Disk Drives

Working Principles

An internal view of an HDD is shown in Fig. 1.1. As seen in the figure, a HDD consists of a spindle, recording disks on the spindle, an actuator arm, suspensions and recording heads attached to the end of the suspensions, a voice coil motor (VCM) and a central controller (circuit board). The spindle can rotate the recording disks at a designed speed. The recording

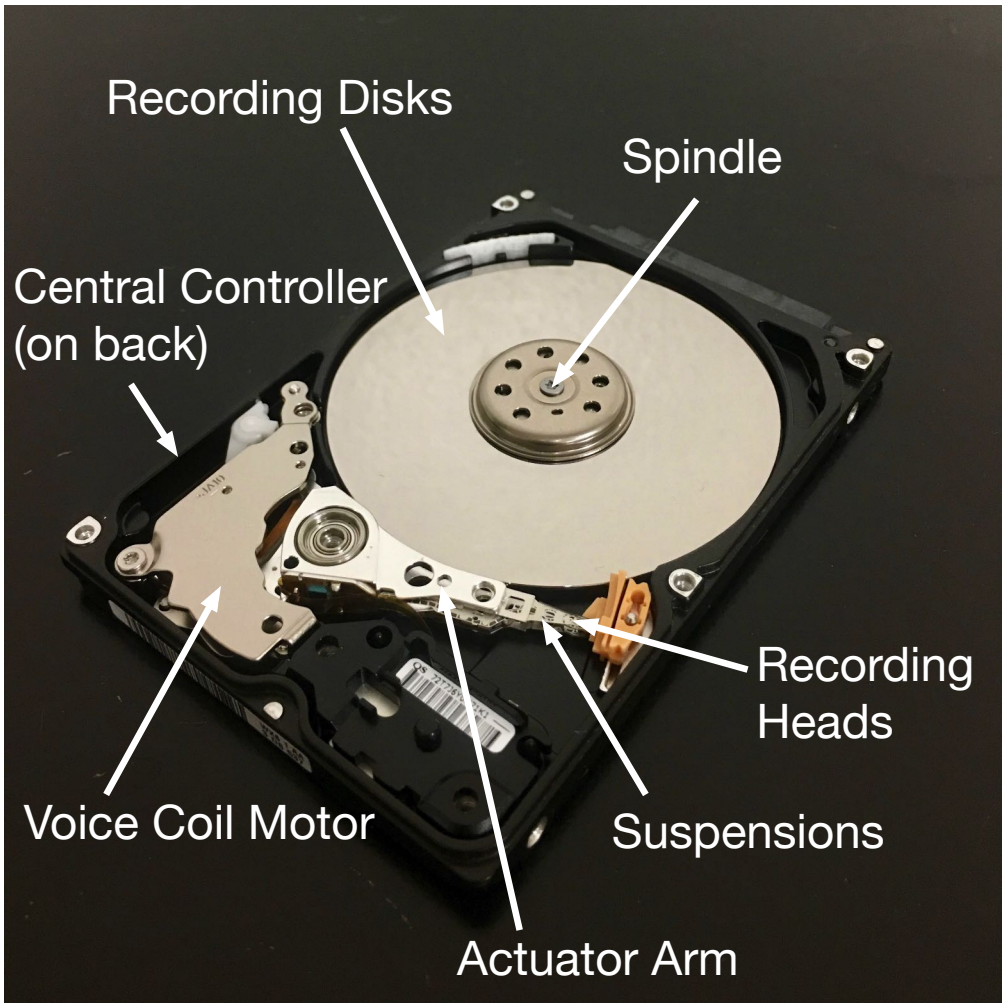

Figure 1.1: The internal view of a hard disk drive.

disks are used to store the data. They are also called magnetic disks, the media or simply the disks. The recording heads read/write the date from/to the disks. They are fixed at the end of the suspension. The VCM can move the actuator arm and the heads to a programmed position. The central controller is the brain of the HDD. It can send commands to the VCM, the spindle and the head. It also processes the read-back signal from the system.

The data is stored at different radial positions on the disk. During its operation, the computer instructs the HDD which file to read/write. The central controller determines the radial position on the disk where the data is stored and instructs the VCM to move the arm with the heads to that position. The head reads/writes the data from/to the rotating disk and sends the raw signal/feedback to the central controller. The controller then processes the signal and sends the data back to the computer. The date reading/writing process is shown in Fig. 1.2.

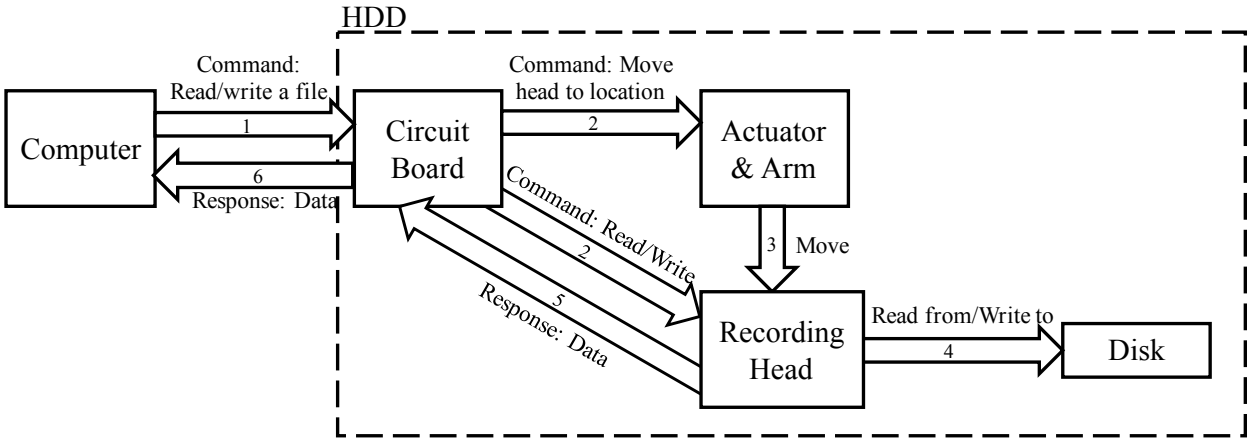

Figure 1.2: The process of a computer accessing/modifying the file stored on the HDD.

The HDD stores the data using magnetism. Fig. 1.3 shows the general structure of a disk. It is noted that some layers such as the soft magnetic underlayer [7] or the heat sink layer [8] have been omitted here for simplicity. As seen in the figure, there is a magnetic layer on top of the substrate. The data is represented by the magnetization of the magnetic material in this layer. For example, in modern HDDs, the magnetization aligns perpendicular to the disk surface (up and down) to represent 1 and 0 in digital recording, and this technology is called perpendicular magnetic recording (PMR). It is noted that the magnetization is not uniform across the entire disk, i.e., it is different at different locations. A number of magnetic grains cluster and form one magnetic bit. In this way, a large amount of data can be stored in a single drive. The formation of the magnetic bits is depicted in Fig. 1.3. On top of the magnetic layer, there is a carbon overcoat (COC) layer and a lubricant layer for performance and wear protection purposes.

The data on the disk is accessed/modified by the recording head. A photo of the head is shown in Fig. 1.4. The head is part of the head gimbal assembly (HGA) in the HDD. The HGAs consists of a metal suspension, a flexible cable and a black block called the slider. The suspension is attached to the actuation arm so the head is suspended relative to the arm. The flexible cable is used to connect the electric signal out of the head. The slider is a small block attached near the end of the suspension. The current production slider design has the "femto" form factor, with the dimensions of $0.85\,\text{mm} \times 0.70\,\text{mm} \times 0.23\,\text{mm}$ [9]. The back surface of the slider is attached to the suspension by a gimbal that permits pitch, roll and yaw rotational motions of the slider. The front surface, called the air bearing surface (ABS), faces the disk. A photo of the slider on the ABS side is shown in Fig. 1.5. It can be seen that the ABS has a complex designed profile. During HDD operation, the slider is brought close to the rotating disk. The disk's moving direction relative to the slider is approximately along the long edge of the slider depending on its radial position. The edge that faces the approaching disk is called the leading edge (LE) of the slider. The opposite edge is called

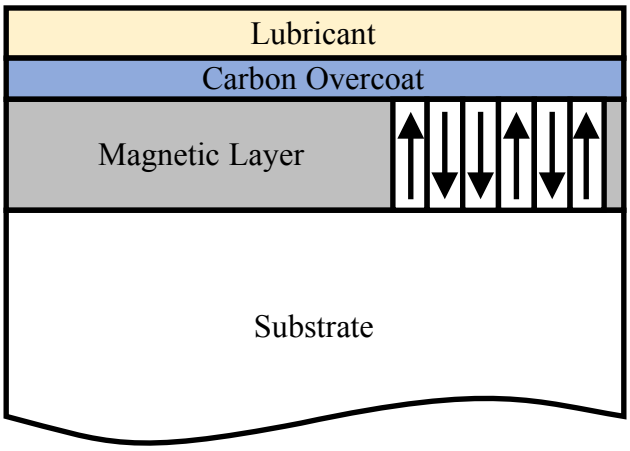

Figure 1.3: A layer profile of a disk. The arrows in the magnetic layer show the direction of the magnetization.

the trailing edge (TE). The leading edge, the trailing edge and the disk moving direction relative to the slider are labeled in Fig. 1.5. As the slider is brought close enough to the rotating disk, it "flies" on an air bearing above the disk with a certain pitch angle. This is because the surrounding air dragged by the disk is brought into the gap between the ABS and the disk surface. With the help of the ABS design, the air is compressed in the gap and forms a strong pressure that pushes the slider away from the disk. The air bearing pressure and the spring force of the suspension are balanced such that the slider maintains a certain distance away from the disk. The space between the ABS and the disk surface is called the head-disk interface (HDI). The minimum distance between the ABS and the top surface of the disk is called the fly-height (FH). Nowadays the FH is less than 10 nm [10]. A schematic of the slider flying on the disk is shown in Fig. 1.6.

In the center of the TE of the ABS, there are two electrical components, called the reader and the writer. The reader is a magnetic field sensor which can sense the reversal of magnetization of the magnetic material on the disk. In current HDD design, the magnetization sensing is based on the tunnel magnetoresistance (TMR) effect [11, 12]. On the other hand, the writer generates an inductive gap magnetic field based on Ampere's law. The generated magnetic field orients the magnetic material on the disk, causing its magnetization to align with the head's writing magnetic field. In this way, the writer erases any prior data stored at this location and writes the new data. The locations of the reader and the writer are annotated in Fig. 1.5. Their positions relative to the disk are depicted in Fig. 1.6. A schematic of the HDD operation is depicted in Fig. 1.7.

The term areal density is used in the HDD industry as a measure of the capacity of a HDD. The areal density is defined as the number of bits of data stored on a unit area of the disk. With higher areal density, more data can be stored in one drive with the same form factor. What is more, since the disk rotating speed is constant at 5400 RPM or 7200 RPM,

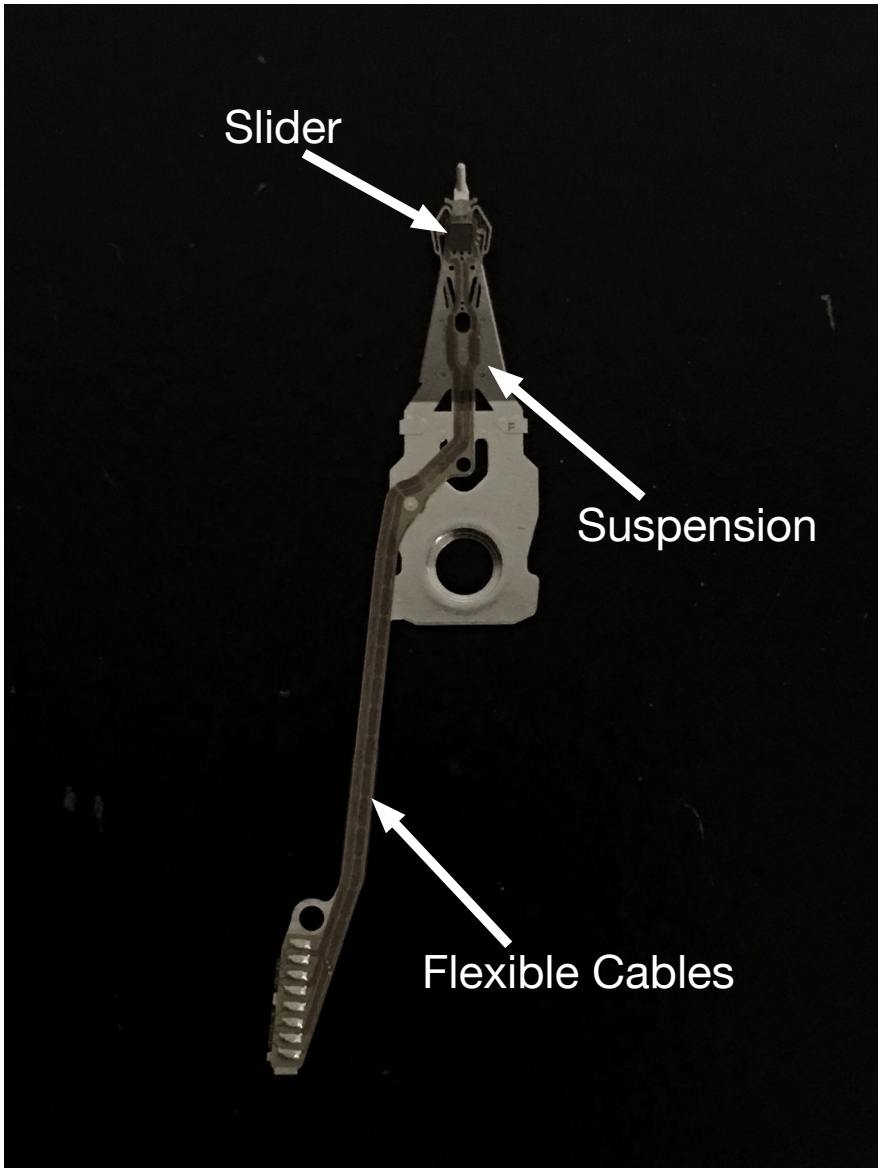

Figure 1.4: ABS view of the HGA.

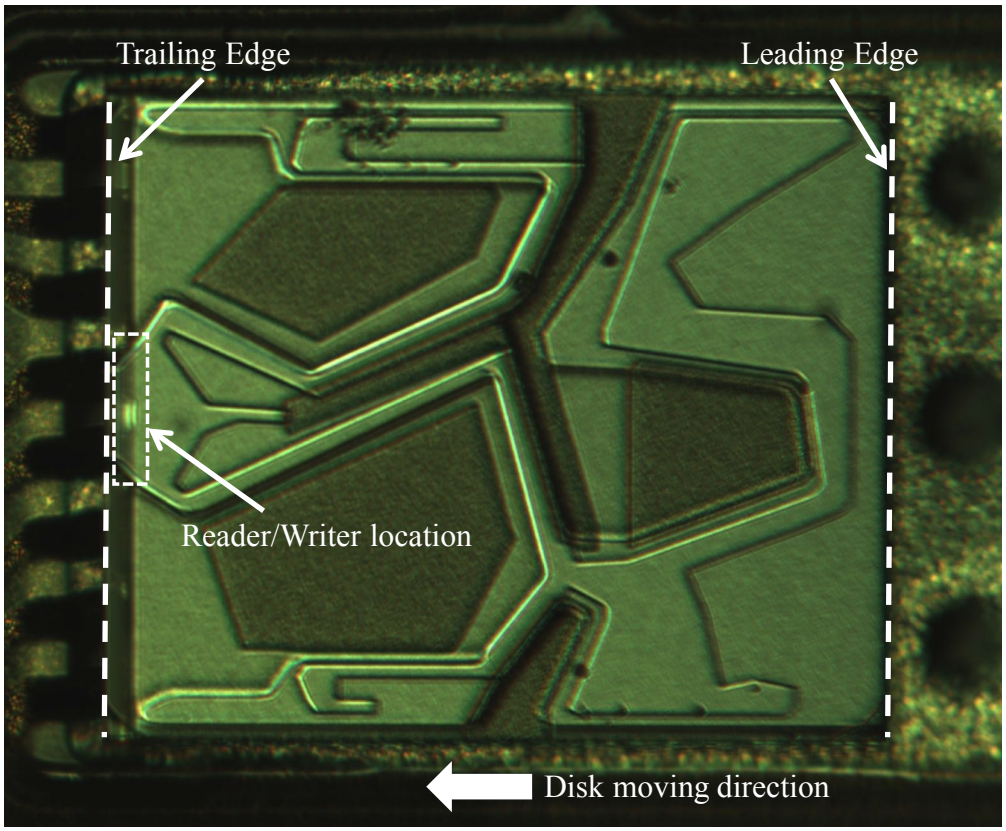

Figure 1.5: A view of the ABS in the microscope.

higher areal density means the head can pass through more bits during the same time, improving the read/write speed. Therefore, increasing the areal density has been one of the main goals of the HDD industry. A typical drive sold in 2017 has an areal density of $\sim$1 Tb/in^2 [13].

The term head-media spacing (HMS) is used to describe the distance between the head and the disk, similar to the fly height. However, there is an important distinction between the HMS and the FH [14]. As shown in Fig. 1.8, the HMS is the distance between the head's reader/writer and the magnetic layer of the disk. Since there is a COC layer, a lubricant layer and surface roughness on the disk and an overcoat layer on the head, the relation between the HMS and the FH is:

$$\text{HMS} = d_{\text{head overcoat}} + \text{FH} + d_{\text{lubricant}} + d_{\text{COC}} + d_{\text{roughness}}, \tag{1.1}$$

where $d_{\cdot}$ means the thickness of the corresponding layer. When the HMS >100 nm, HMS $\approx$ FH, since the thickness of the protective layer is only a few nanometers thick. However, the difference between the HMS and the FH cannot be neglected when the FH is $\sim$10 nm. In the experiments to be discussed, the term FH is usually used since this is what is directly measured by the "touchdown" method.

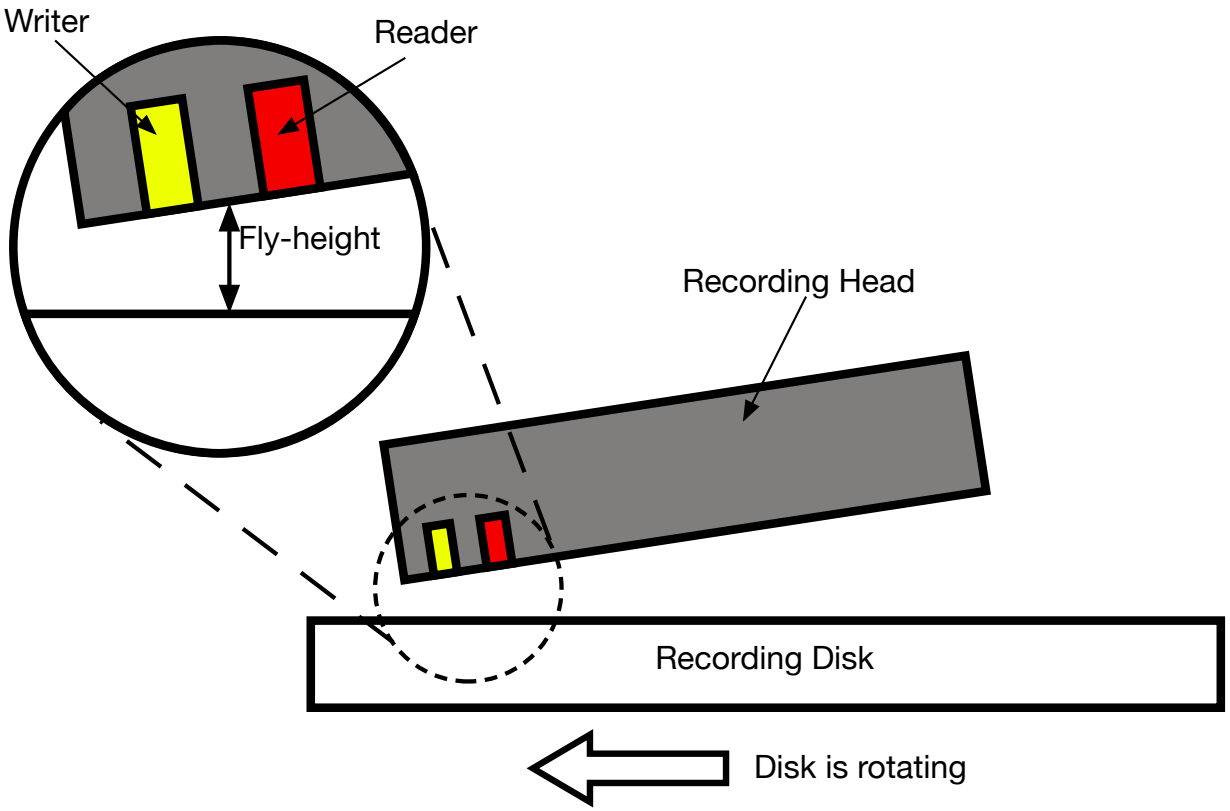

Figure 1.6: The schematic of the HDD's recording head and recording disk. The head has a reader and a writer, facing the disk. The head and the disk are moving relatively. The head and the disk are not in contact. The details of the reader and the writer are omitted.

The HMS and the areal density are strongly correlated. This is because when the areal density increases, the size of individual magnetic bits decreases, resulting in smaller magnetic flux. Therefore the head must be closer to the disk to pick up the signal. As can be seen in Fig. 1.9, the historical relation between the HMS and the areal density follows roughly the equation,

$$(\text{HMS in nm}) = 85.1 \times (\text{Areal Density in Gb/in}^2)^{-0.354}. \tag{1.2}$$

Technology Development

The first HDD, the IBM 350 Disk Storage (IBM-350), was introduced in September 1956 by IBM. It was a part of the IBM 305 Random Access Memory Accounting (RAMAC) system which was one of the last vacuum tube systems designed by IBM [15]. Each IBM-350 unit was 60 inches (1.52 m) long, 68 inches (1.73 m) high and 29 inches (0.74 m) deep with a capacity of 5 MB. The disks rotating speed was 1200RPM and the areal density was 2000 b/in^2. The HMS was 20 µm. Compressed air was supplied between the head and the disk to maintain

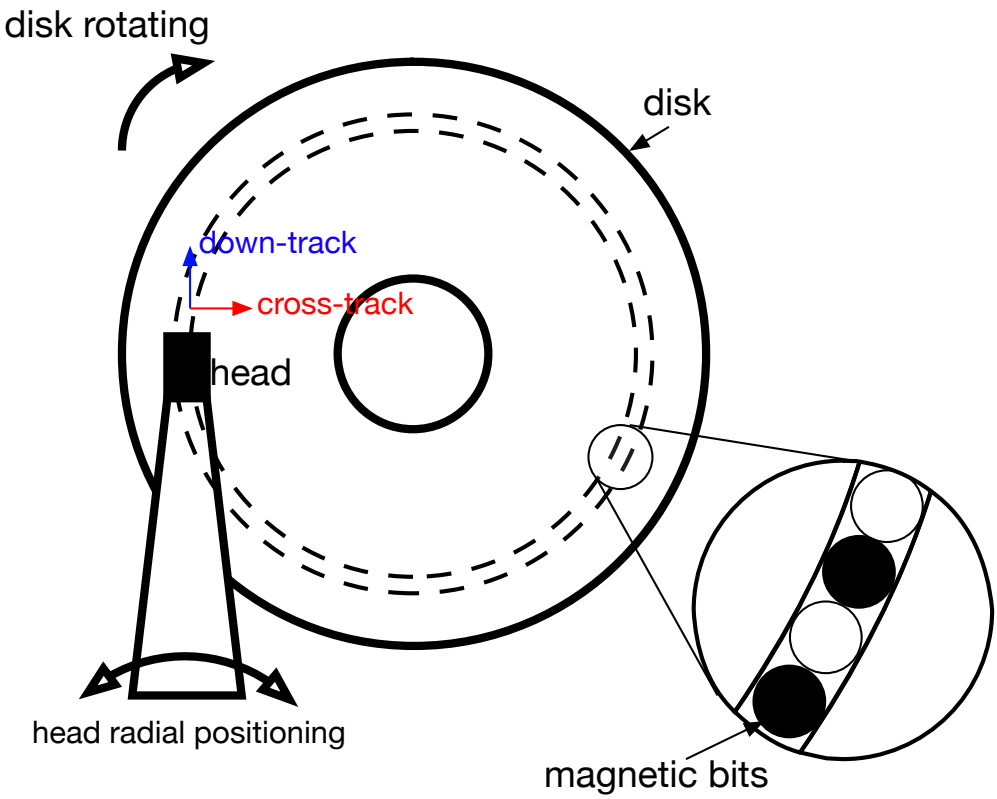

Figure 1.7: A schematic of the HDD operating. The disk rotates at a certain speed while the head "flies" above the disk. The head's reader and writer (not shown) can access or modify the magnetic bits written on the disk. The head's radial position can change to seek data in different tracks. The down-track direction is pointing towards the end of the head. The cross-track direction is perpendicular to the down-track direction.

the head-disk spacing, which required a complex air compressor [16]. The average seek time was 600 ms. The lease price for the unit was $750 per month [17] while the entire RAMAC system was leased for $3200 per month [18].

In 2016, the HGST Ultrastar He^{12} drive was introduced by Western Digital [19]. Its capacity is 12 TB, with the dimension of 101.6 mm $\times$ 147 mm $\times$ 26.1 mm. Its max areal density is 864 Gb/in^2. The typical seek time is 8.0 ms/8.6 ms for read/write. The sale price for the drive is about $500.

A comparison between the two drives can also be seen in Table 1.1. It is seen that within the past 60 years, the capacity of a single drive has improved by a factor of 10^6 while the volume has shrunk by $\sim$ 5000 times. What is more, the seek time also reduces by $\sim$ 100x and an individual drive is even more affordable to own today than to lease for one month 60 years ago, regardless of the inflation. All of these are due to the dramatic increase of the drive's areal density, which increased by a factor of 10^9.

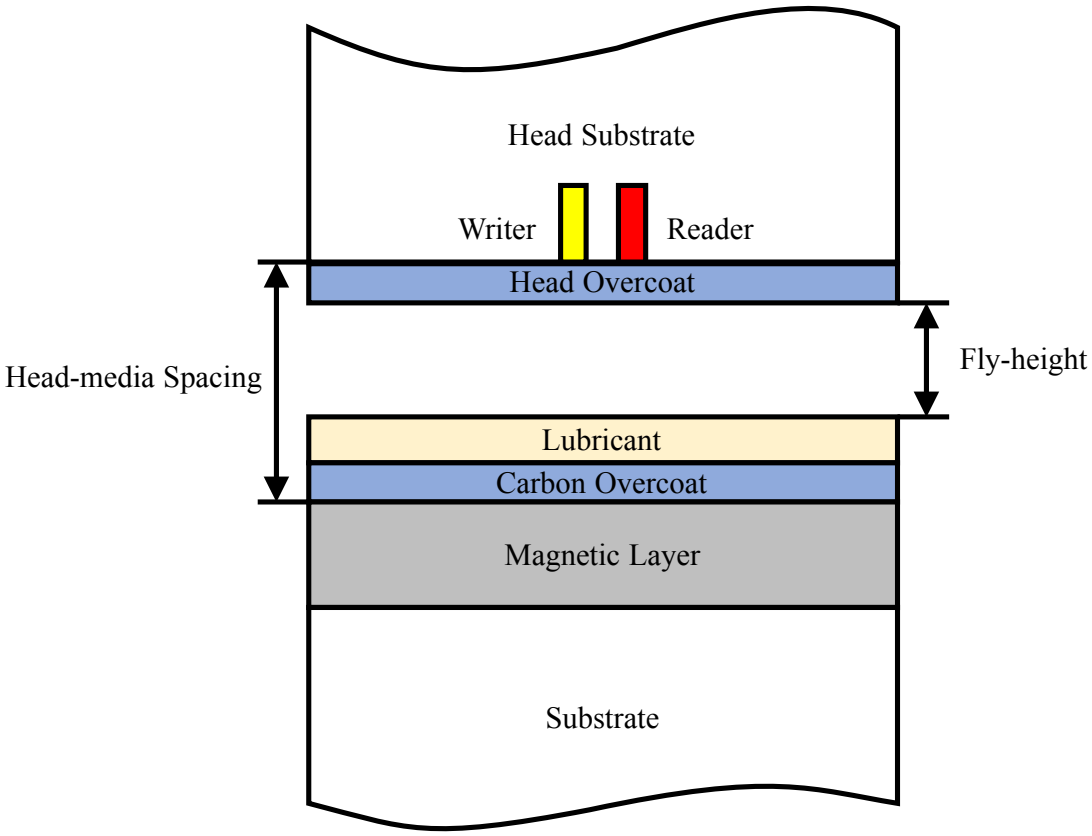

Figure 1.8: The distinction between the FH and the HMS.

There are several recent important technologies that led to the impressive HDD development progress, such as the thermal fly-height control (TFC) technology [20, 21], shingled magnetic recording (SMR) technology [22, 23], helium technology [24], dual-stage technology [25], etc. The TFC technology uses thermal expansion to lower the FH and the HMS. It will be introduced in detail in Section 2.1. In the SMR technology, the magnetic bits on adjacent tracks are overlapped, like the roof shingles on buildings. A schematic of the SMR technology is shown in Fig. 1.10. With SMR, the areal density can be increased by 25% compared with the conventional PMR technology [26]. In helium drives, the gas environment inside the HDD is helium instead of air. The HDD is encapsulated so the helium gas will not escape. With helium, the disk platters can be thinner so that more disks can fit into a single drive, increasing the capacity. The gas dragging force to the disk is also reduced so less power is required for HDD operation. In the dual-stage technology, a second actuator is attached to the suspension in addition to the VCM actuator. In this way, the heads are able to find the desired track in a shorter time and the system is more stable to external disturbances [27, 28, 29].

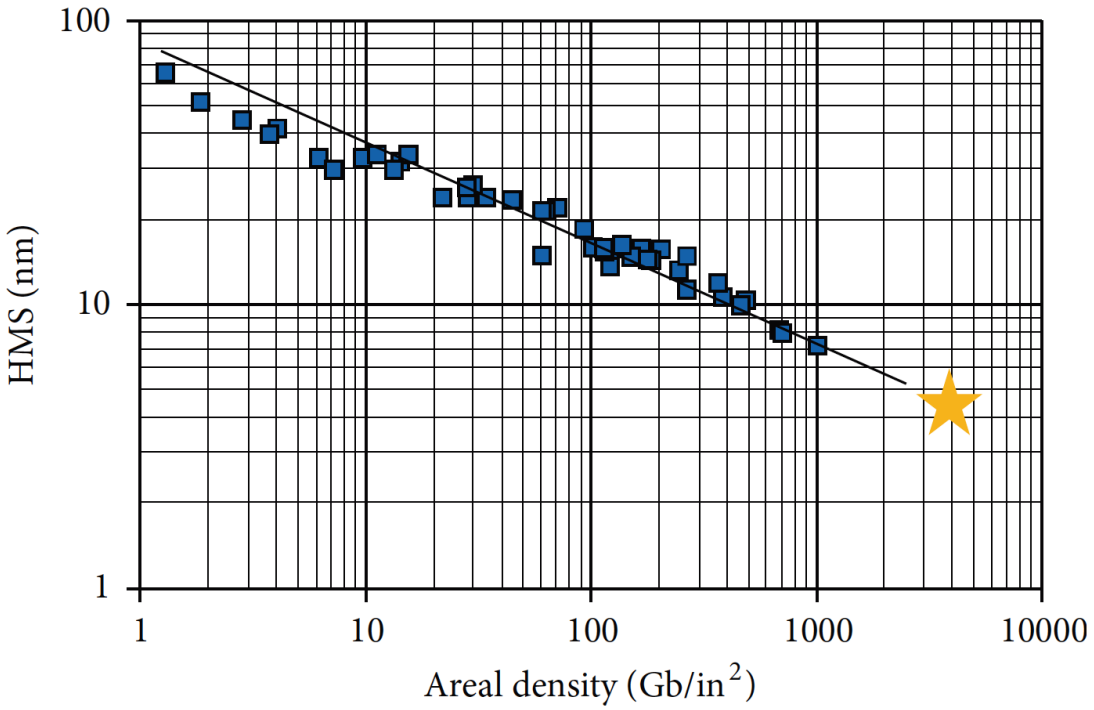

Figure 1.9: The historical HMS versus the areal density. The yellow star is the extrapolation at 4 Tb/in^2. From Fig. 3 of Ref. [14].

Item Name	IBM-350	HGST Ultrastar He^{12}	Ratio (IBM:HGST)
Year Introduced	1956	2016	-
Capacity	5 MB	12 TB	$2.4 \times 1 : 10^6$
Dimensions [mm]	$1524 \times 1727 \times 737$	$101.6 \times 147 \times 26.1$	4976 : 1
Areal Density [b/in^2]	2000	8.64×10^{11}	$1 : 4.32 \times 10^8$
Seek Time (read) [ms]	600	8.0	75 : 1
Seek Time (write) [ms]	600	8.6	70 : 1
Price [$]	750/month (lease)	500 (sale)	-

Table 1.1: A comparison between two drives, IBM-350 and HGST Ultrastar He^{12}.

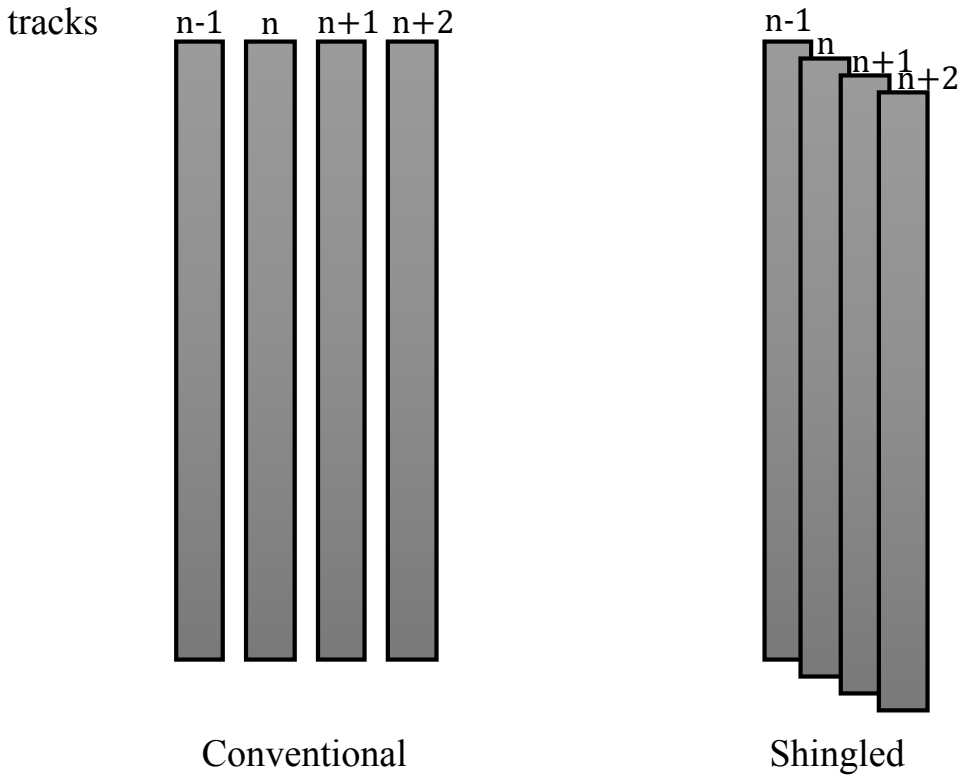

Figure 1.10: Schematics of the conventional magnetic bits alignment and the shingled alignment.

1.2 Heat Assisted Magnetic Recording Technology

The magnetic grain is the smallest unit of the magnetic material where the magnetization is in the uniform direction. In order for the HDD to achieve an acceptable signal-to-noise-ratio (SNR), a single magnetic bit needs to contain a sufficient number of magnetic grains. On the other hand, to push the areal density higher, the volume of a single magnetic bit needs to be smaller, requiring a reduction of the magnetic bit's volume. This pushes the magnetic bit towards the superparamagnetic limit [30].

The superparamagnism occurs in the nanoscale magnetic grain, causing the magnetization to randomly flip its direction under the influence of temperature [31]. The mean time between flips follows the Néel-Arrhenius equation:

$$\tau_N \propto \exp\left(\frac{KV}{k_B T}\right), \tag{1.3}$$

where τ_N is the mean time of the flip, K is the magnetic anisotropy energy density, depending on the material, V is the nanoparticle's volume, k_B is the Boltzmann constant and T is the absolute temperature. Therefore, for the data in an HDD to be thermally stable for 10 years, it is required that [3]:

$$\frac{KV}{k_B T} \geq\sim 70. \tag{1.4}$$

As seen in Eq. 1.3, when the volume V decreases, τ_N decreases for fixed K and T which causes the magnetic grain to be thermally unstable. One way to compensate for this is to find a magnetic material that has higher magnetic anisotropy K, such as $L1_0$-FePt [8]. But high magnetic anisotropy material usually has high magnetic coercivity, which means it is harder to flip the magnetization with an external magnetic field. Therefore, magnetic recording faces a trilemma with increasing areal density: adequate SNR (requires small grain size or V), thermal stability (requires large KV) and write-ability (requires small K) [32]. In this trilemma, only two out of three can be achieved with current PMR technology. An illustration of the trilemma is shown in Fig. 1.11.

Heat assisted magnetic recording (HAMR) technology was proposed by the HDD industry to overcome this trilemma. In HAMR, the magnetic material in the media is chosen to have high K. Therefore, the grain size of the material can be shrunk further. As a result, the magnetic bits size can shrink proportional to the grain size shrinkage without compromising the SNR. The areal density can thus increase. It is estimated that with HAMR technology, the areal density can reach $10\,\mathrm{Tb/in^2}$.

But the problem with high K material is poor write-ability. This difficulty is overcome by introducing a heating element. During data writing, the magnetic bits to be written are heated to the Curie temperature of the media such that its coercivity is reduced to near zero. Then the magnitude of the external magnetic field required to flip a bit is reduced and the write-ability is regained. The writer on the head element supplies such a magnetic field and the magnetic re-orientation is accomplished. Lastly, the magnetic bit is moved

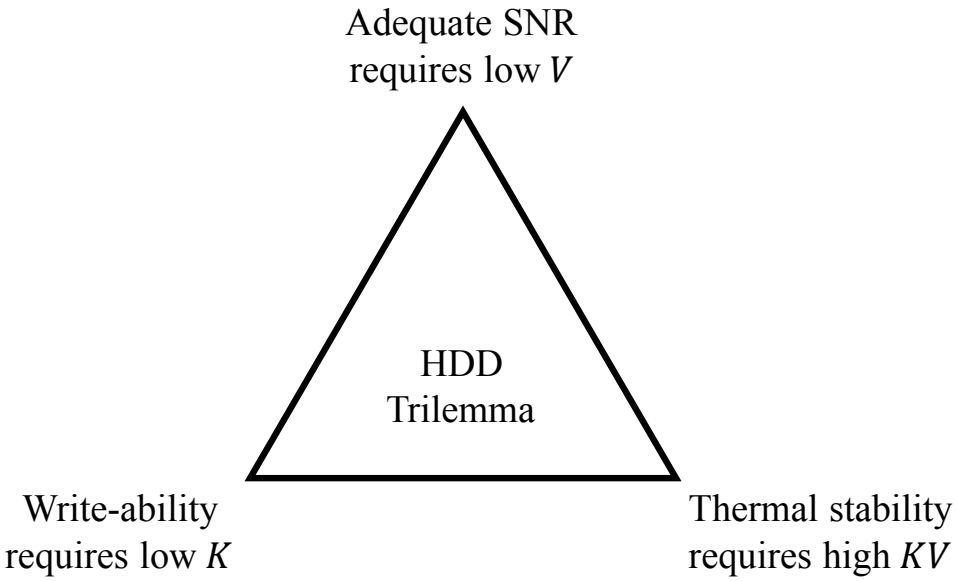

Figure 1.11: The trilemma that prevents the continuous areal density increase of the HDD with conventional magnetic recording method. The figure is reproduced based on Fig. 1 of Ref. [32].

away from the heating element such that it can cool down. The coercivity increases again to "freeze" the magnetic bit to achieve thermal stability. The relation between coercivity and temperature is shown in Fig. 1.12 and the process of writing in HAMR is shown in Fig. 1.13.

The heating in HAMR writing is achieved by the use of a laser. In the HAMR head, a laser diode (LD) is embedded on the back of the slider, as shown in Fig. 1.14. The light generated by the LD passes through a waveguide, shrinking the laser beam size from microns to ∼500 nm. However, due to the diffraction limit, the size of the laser spot cannot be shrunk further with far field optics. Therefore, a metallic antenna called a near field transducer (NFT) is attached at the end of the waveguide for final focusing. The NFT further shrinks the laser beam size from ∼500 nm down to ∼50 nm through the plasmonic effect [4]. Finally the electromagnetic (EM) energy is partially absorbed by the magnetic layer in the media, generating heat and causing its increase in temperature.

The HAMR media profile is also different from that in PMR. Firstly, the magnetic material in the magnetic layer needs to have high anisotropy and relatively low Curie temperature. $L1_0$-FePt is the present media of choice. $L1_0$-FePt has a magnetic anisotropy energy density of 7×10^6 J/m^3 and a Curie temperature of 750 K [33]. Secondly, the thermal profile of the heated magnetic material needs to be contained within one bit size to avoid adjacent bit erasing. Therefore, a heat-sink layer is needed underneath the magnetic layer to create a narrow temperature profile in the lateral direction [34]. Thirdly, the COC layer and the

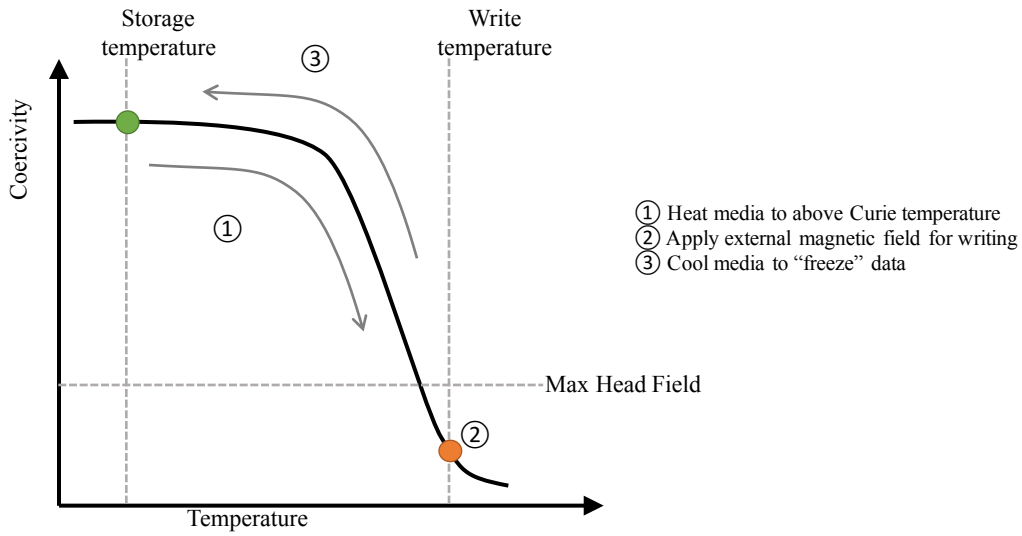

Figure 1.12: An illustration of the magnetic material's coercivity vs. the temperature. Inspired by Fig. 1 of Ref. [4].

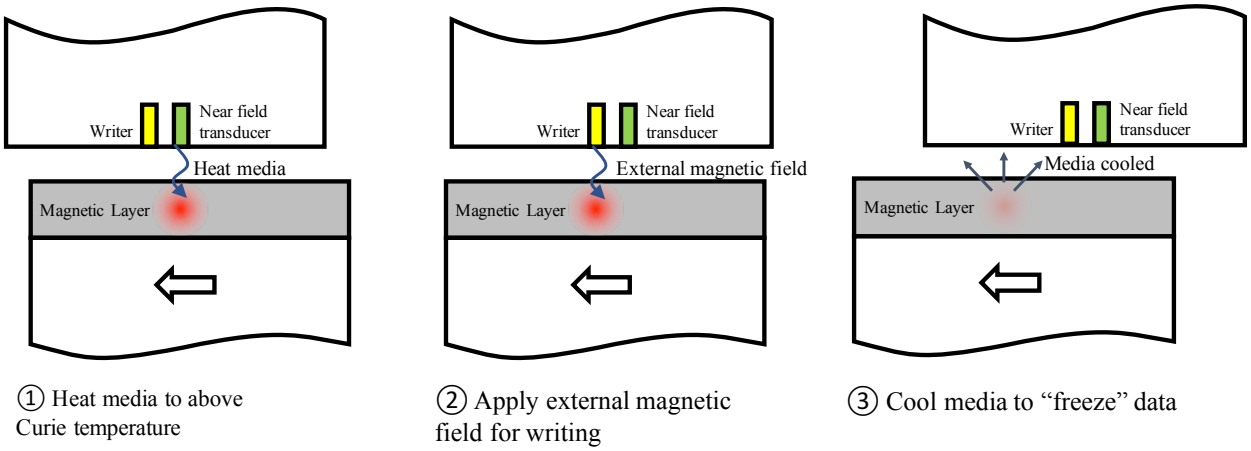

Figure 1.13: The writing process in HAMR. Certain layers such as lubricant, COC and heatsink are omitted.

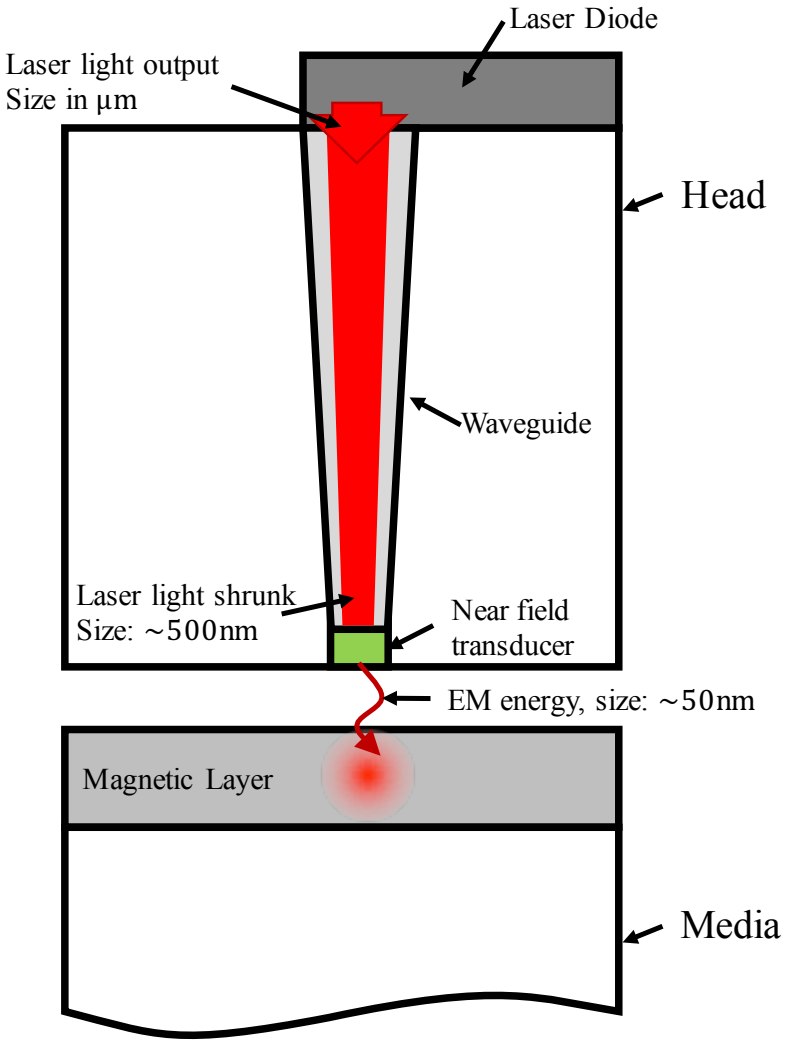

Figure 1.14: A schematic of the optical energy delivery in HAMR.

lubricant layer experience high temperature since they are close to the magnetic layer. The materials in these layers are subject to evaporation, decomposition and thermal depletion, and therefore these issues need to be addressed.

The high temperature in the HAMR technology can cause unprecedented problems compared with the conventional magnet recording (CMR) technology. The material surrounding the heated magnetic bits will also be heated. The COC can degrade and the lubricant can evaporate and decompose. Most importantly, since the NFT's design temperature is much lower than the media's Curie temperature, it is unavoidable that the media heat can flow back from the media to the NFT. This is called a "back-heating" effect. Since the distance between the NFT and the media is only a couple of nanometers, the back-heating effect could be very strong and cause undesired additional temperature increase on the NFT, shortening its lifetime. Recently, it was reported that solid contamination appears on the ABS of the slider near the NFT location after flying with laser heating [35, 36]. The contamination can block the optical path of the NFT and cause additional NFT overheating. The mechanism of the contamination's formation also needs investigation.

Overall, undesirable mass and energy transfer happens during the HAMR writing process. It is noted that the transfer happens at the nanoscale, both spatially and temporally. It causes reliability issues, and it can shorten the lifetime of the HDD. However, the mechanism behind the transfer is still unclear and needs more investigation.

1.3 Objectives and Organization

In this dissertation, some experimental studies of the mass and energy transfer in the nanoscale HDI are studied. These experiments were performed based on state-of-the-art design of HDDs. An experimental stage, called the Computer Mechanics Laboratory (CML)-HAMR stage was built in order to perform the experiments. The CML-HAMR stage can emulate HAMR conditions, with a disk spindle, a head fixture and a laser generator. Some innovative elements in the head, such as the TFC heater and the embedded contact sensor (ECS), were used for generating and sensing the heat. The "waveguide" heads with embedded laser and waveguide, which can heat the media in nanoscale, were also used to emulate HAMR conditions. These experiments can quantify the severeness of the mass and energy transfer in the HDI, which can be used as a guideline for HAMR drive design.

This dissertation is organized as follows. Chapter 1 (this chapter) presents the working principle of the HDD and the HAMR technology. The existing issues of HAMR are explained. Chapter 2 gives a more detailed introduction of the HDD. Some important elements in the head, such as the TFC heater, the ECS and the laser power delivery system (LPDS) are briefly introduced. Chapter 3 introduces the experimental stages for the studies. The stages include a comprehensive stage - the CML-HAMR stage - which is used for most of the experiments, and a calibration stage for the ECS. Chapter 4 presents the measurement of the head's temperature where it is heated by a beam of free space laser, the so-called "back heating" experiment. Chapter 5 introduces a study of the heating effect of the ECS, and

explains how this effect can be used to measure the heat transfer across the HDI. Chapter 6 discusses the experiments related to the waveguide heads. The powering of the laser in the waveguide head can cause several issues including an additional protrusion on the ABS and solid contamination on the head, which are addressed in this chapter. In Chapter 7, the lubricant behavior, especially its reflow, is studied both experimentally and by numerical modeling. Finally, Chapter 8 concludes the dissertation and has a look at future work.

Chapter 2

A Detailed View of the HDI in HAMR

In this chapter, a more detailed view of the HDD will be given. The thermal fly-height control (TFC) heater was designed to decrease the HMS such that higher areal density can be achieved according to Eq. 1.2. The embedded contact sensor (ECS) was developed in order to detect the head-disk contact. The laser power delivery system (LPDS) is an essential part of HAMR technology. These three components are all either generating or detecting heat when in operation. Therefore, they can be used in the heat transfer study of the HDI. The TFC technology, the ECS and the LPDS will be introduced in Sections 2.1, 2.2 and 2.3, respectively. The chapter is summarized in Section 2.4.

2.1 Thermal Fly-height Control Technology

The FH was continuously brought down to ∼10 nm over all the years by optimizing the ABS geometry design. In order to bring down the FH to 1 nm, the thermal fly-height control (TFC) technology was introduced [37].

In the earlier conventional recording head the only two electrical components were the reader and the writer, but in the later TFC technology, a micrometer scale resistor, called the TFC heater, is also embedded in the center of the TE of the slider. A cross-sectional view of a slider with the TFC heater is shown in Fig. 2.1. As seen in the figure, the TFC heater is buried beneath the surface of the ABS, close to the reader.

The TFC heater, a resistor, is electrically connected to an external circuit. It is controlled by a DC voltage supply. When the voltage is applied, it heats up according to the Joule's heating law,

$$P = VI = I^2R = \frac{V^2}{R}, \tag{2.1}$$

where P is the generated power of the heater, called the TFC power, V is the voltage, I is the current and R is the resistance. The heat generated by the TFC heater causes the

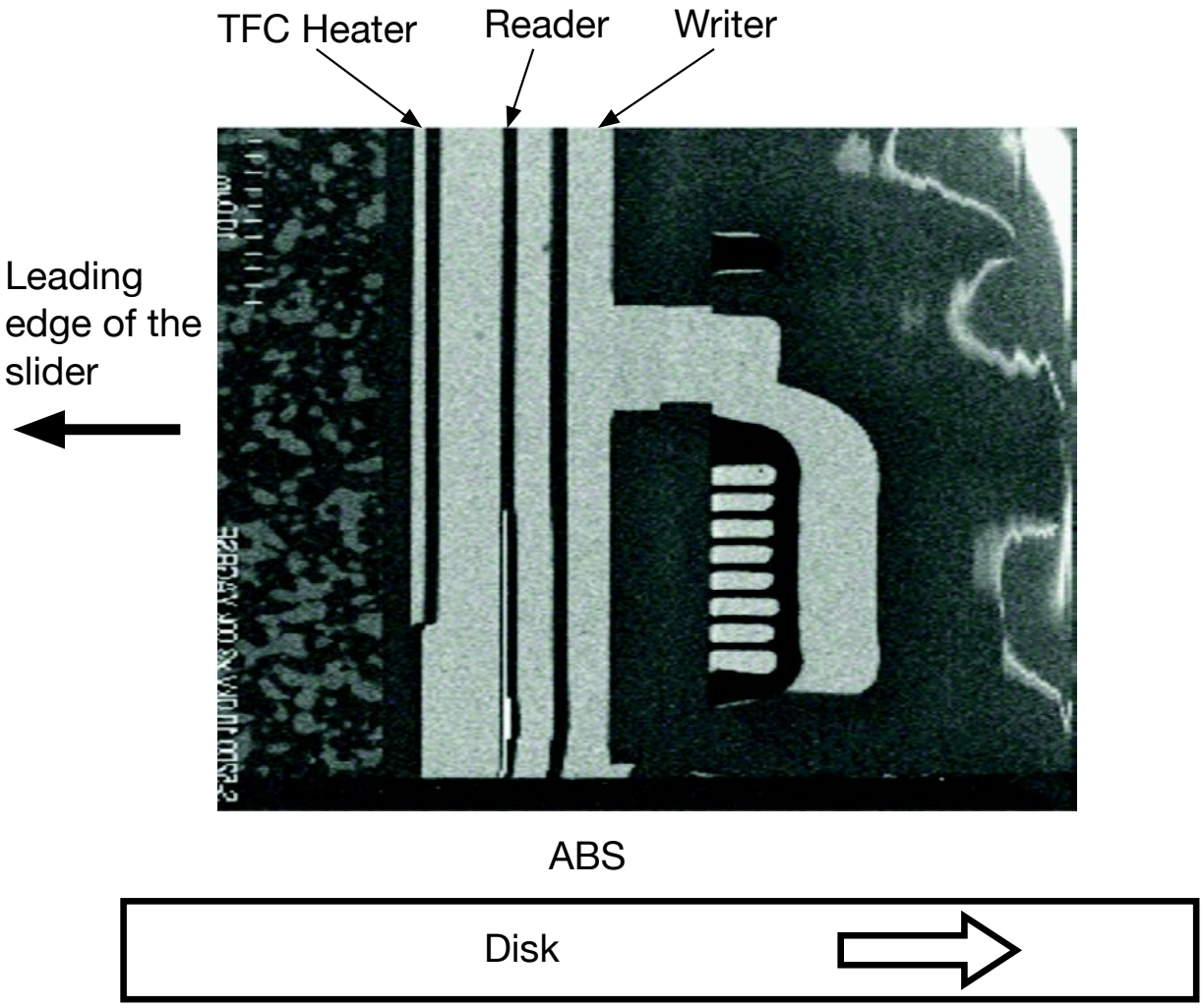

Figure 2.1: A cross sectional view of a slider with the TFC heater. The light colored thin bar-shaped metal is the TFC heater. The rest are either the reader or the writer. It is noted that the TFC heater might be at different locations in different designs. The photo is from Ref. [38] with additional annotations.

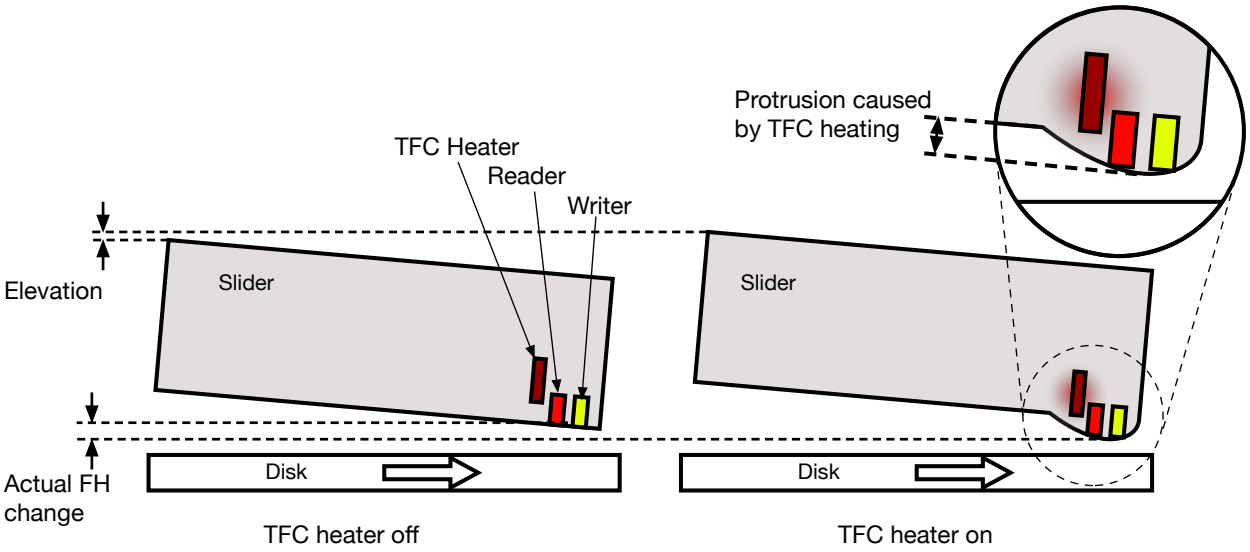

Figure 2.2: A schematic of the TFC heater actuation. The left figure shows the case when the TFC heater is off, while the right on shows the TFC-heater-on case. The TFC heater causes thermal protrusion on the slider's surface. The protrusion causes FH decrease. It is noted the head is elevated due to the increase of the air bearing pressure.

temperature to increase surrounding it, subsequently leading to a local thermal expansion of the slider's body. The thermal expansion results in a local surface protrusion on the TE of the slider's surface, optimally at the location of the read-write (R/W) elements. As a result, the R/W elements are brought closer to the disk by the protrusion, which lowers the effective FH and increases the SNR. Fig. 2.2 shows the working principle of the TFC actuation.

It is noted that when the heater is active, the ABS profile changes due to the surface protrusion. As a result, the flying dynamics of the slider also changes. A direct result of the reduced spacing is that the average pressure on the slider is increased at the area of protrusion. This pressure increase and the local FH decrease are two competing factors determining the FH at the R/W elements location. Therefore, the effective FH decrease is less than the absolute surface protrusion [21]. This effect is depicted in Fig. 2.2.

After the HGA with embedded TFC heater is designed and manufactured, the relation between the FH decrease and the TFC power can be characterized experimentally [39]. Similar numerical models were also created to compare with the experiment [40]. One set of characteristic curves is shown in Fig. 2.3. It can be seen that the FH decrease is almost linear with the TFC power, although some non-linear effects appear as the slider comes closer to the disk. Therefore, the FH-TFC power ratio can be defined as the absolute value of the slope of the linear regime of the curve. The design of the TFC heater has been optimized such that the FH-TFC power ratio is about $0.1\,\mathrm{nm/mW}$.

It is also noted that as the TFC power continues to increase, the FH continues to decrease. Finally, the FH can decrease to zero, causing the slider to drag on the disk, which is called

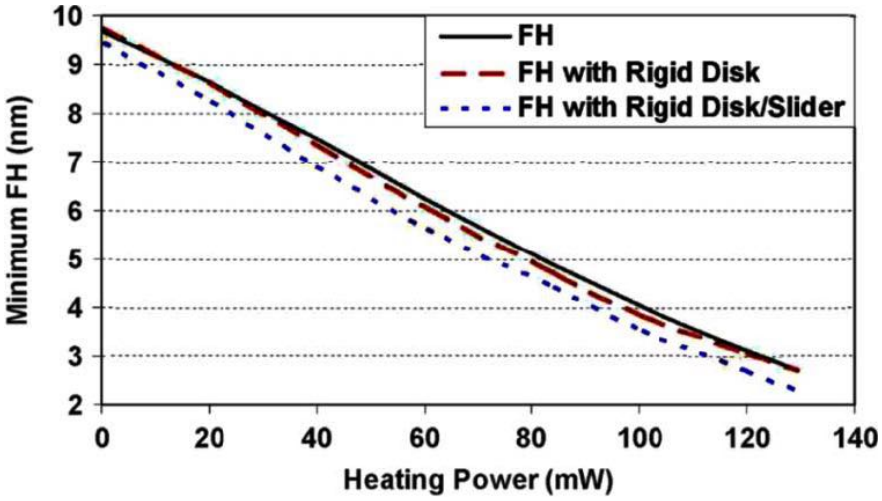

Figure 2.3: The FH decrease vs. the TFC power. Fig. 10 from Ref. [39].

touchdown (TD), or head-disk contact. In component level testing, the head-disk contact can be detected by an acoustic emission (AE) sensor, which detects the vibration caused by the contact. In the drive level, the head-disk contact is detected by the ECS, which is introduced in Section 2.2. The TFC power that causes head-disk contact is called the "touchdown power" (TDP). The TFC power should always be below the TDP to avoid wear on the head and the disk. When the TFC power exceeds the TDP, the slider is in the "overpush" regime.

Overall, turning on the TFC heater during reading and writing enables the temporary decrease of the HMS to improve the SNR. While idling, the TFC power is turned off such that the head-disk spacing is large enough to minimize unnecessary head-disk contact. Since heating is involved in the TFC system, it can be used in the experimental study of heat transfer across the HDI. The details of this will be discussed in Chapters 4, 5 and 6.

2.2 The Embedded Contact Sensor

When the TFC heater is active, the FH is often as low as 1 nm. Since the FH is so small, the HDDs are more prone to external disturbances which can cause head-disk contact, such as operational shock. Moreover, if the TFC power is too high, TD can happen. Unexpected contact can cause large shear stress on both the head and disk, causing wear and shortening the HDDs' lifetime. Therefore, it is important to know the exact condition for which contact happens. In commercial drives, the embedded contact sensor (ECS) is used for contact detection.

The ECS is a resistor located at the surface of the center of the TE of the slider, between the reader and the writer as shown in Fig. 2.4. It is made of a temperature sensitive material such as NiFe [41]. The ECS is nominally 1 to 2 µm wide, 0.2 to 0.5 µm high and 20 to 60 nm

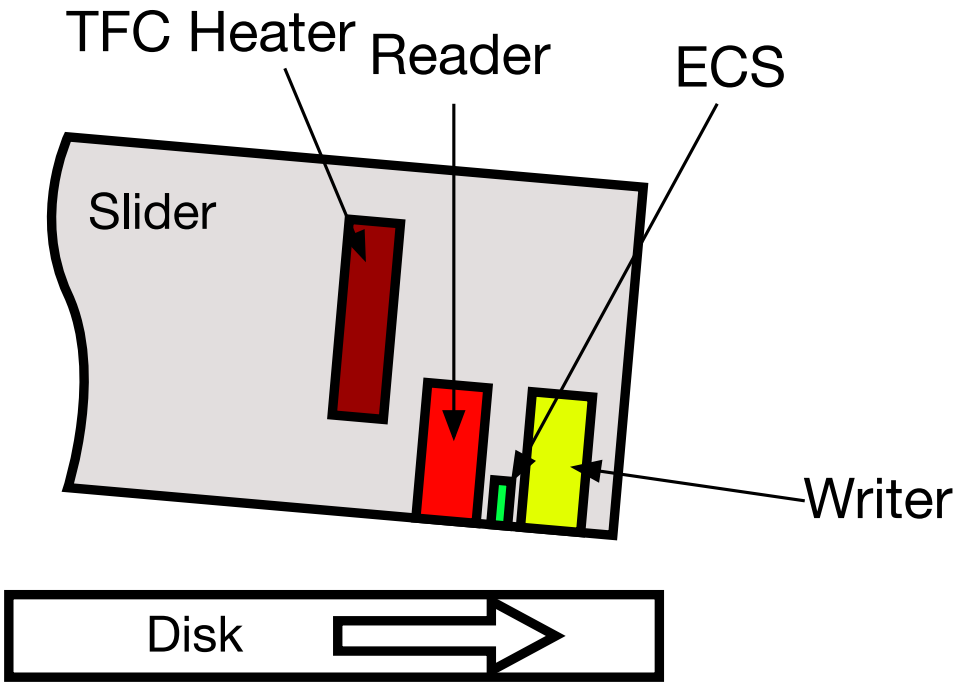

Figure 2.4: A schematic of the cross-sectional view of a slider with an ECS. The ECS is located on the surface of the slider between the reader and the writer.

thick, but it can vary with the design of the head [42]. It's resistance changes with its temperature according to the relation:

$$R_T = R_0(1 + \alpha_0(T - T_0)), \tag{2.2}$$

where T and T_0 are any temperature and room temperature, R_T and R_0 are the resistances of the ECS at T and T_0 respectively, and α_0 is the temperature coefficient of resistance of the ECS at T_0. α_0 is generally unknown and needs calibration. The experimental setup for the calibration will be discussed in Section 3.2, and the calibration process and result will be discussed in Section 4.3. Therefore, by measuring the resistance change of the ECS, the temperature change surrounding it can be detected.

When the FH changes, due to the TFC actuation or operational shock, the heat transfer coefficient in the HDI changes. More specifically, there is more cooling of the ABS when the FH decreases, causing a temperature drop of the ECS. On the other hand, if the TFC actuation is the cause of the FH decrease, since the TFC heater generates heat, the ECS temperature increases. Therefore, the TFC heating and the increase of the air bearing cooling are two competing factors that cause temperature changes of the ECS before the TD. When the TD happens, the contact sliding on the disk causes frictional heating of the slider and additional heating of the ECS.

The relations between the temperature of the ECS and the TFC power, called the ECS temperature curves, are shown in Fig. 2.5. Different curves represent the relations at different disk rotating speeds. It can be seen that each curve has three regimes. In the first regime, the ECS temperature increases as the TFC power increases. However, the rate of the temperature change decreases, i.e., the slope of the curve decreases. Since the TFC power is the sole heat source, the decrease of the rate indicates that the heat transfer coefficient in the HDI increases. However, the TFC heating still dominates the ECS temperature increase. This regime is called the "far-field" regime, indicating the slider is still some distance ($>\sim$2 nm) away from the disk. In the second regime, the temperature of the ECS decreases as the TFC power increases. This indicates that the heat transfer coefficient is so strong that the cooling dominates. This regime is called the "proximity" regime, where the slider is very close to the disk ($\sim$1 nm). In the third regime, when the TFC power continues to increase, the temperature of the ECS suddenly increases again. And the rate of the ECS temperature increase is again high. This is because the head and the disk are in contact. Therefore, the frictional heat contributes to the temperature increase of the ECS. This regime is called the "overpush" regime. The three regimes are annotated in Fig. 2.5.

It is also noted from Fig. 2.5 that at different disk rotating speeds, the ECS temperature curves are different. The ECS temperature curves at low disk speeds start to enter the proximity and overpush regimes earlier than those at high disk speeds. This is mainly because the initial FH is lower when the disk rotating speed is lower. Since the FH-TFC power ratio is similar at different disk rotating speeds, the TDP at lower speed is also lower.

It is usually considered that a TD happens the moment the ECS temperature curves enter the "overpush" regime [43]. This is when the ECS temperature curve reaches its local minimum as shown on the second dash line in Fig. 2.5. However, this is often hard to detect during the experiment. Another approach is to use the derivatives of the ECS temperature curves, as shown in Fig. 2.6, where the y-axis is the temperature change rate with the unit of K/mW. The curves start from positive values but gradually decrease with the TFC power. They then reach the value zero, corresponding to the first local maximum point shown in Fig. 2.5. This is the boundary between the far-field regime and the proximity regime. The value continues to decrease until it reaches the minimum. Then it starts to increase until it again reaches zero, corresponding to the local minimum point shown in Fig. 2.5. This is the boundary between the proximity regime and the overpush regime. This point is defined as the TD point and the corresponding TFC power is the TDP. In this figure it can be seen that each curve has three key points: the first zero point, the minimum point and the second zero point. In the component level or drive level experiment, if early TD detection is desired, the first zero point or the minimum point can be used as the TD criteria. This way, the TD detection is more conservative, and therefore the head-disk contact is less likely and the HDD's lifetime can be prolonged. The TD detections using different methods at different disk rotating speeds are shown in Fig. 2.7.

The ECS is a recent development of the HDD industry. It is an elegant structure embedded in the slider to detect head-disk contact. The physical principle behind it is detecting the temperature change caused by Joule heating, frictional heating, interfacial heat transfer

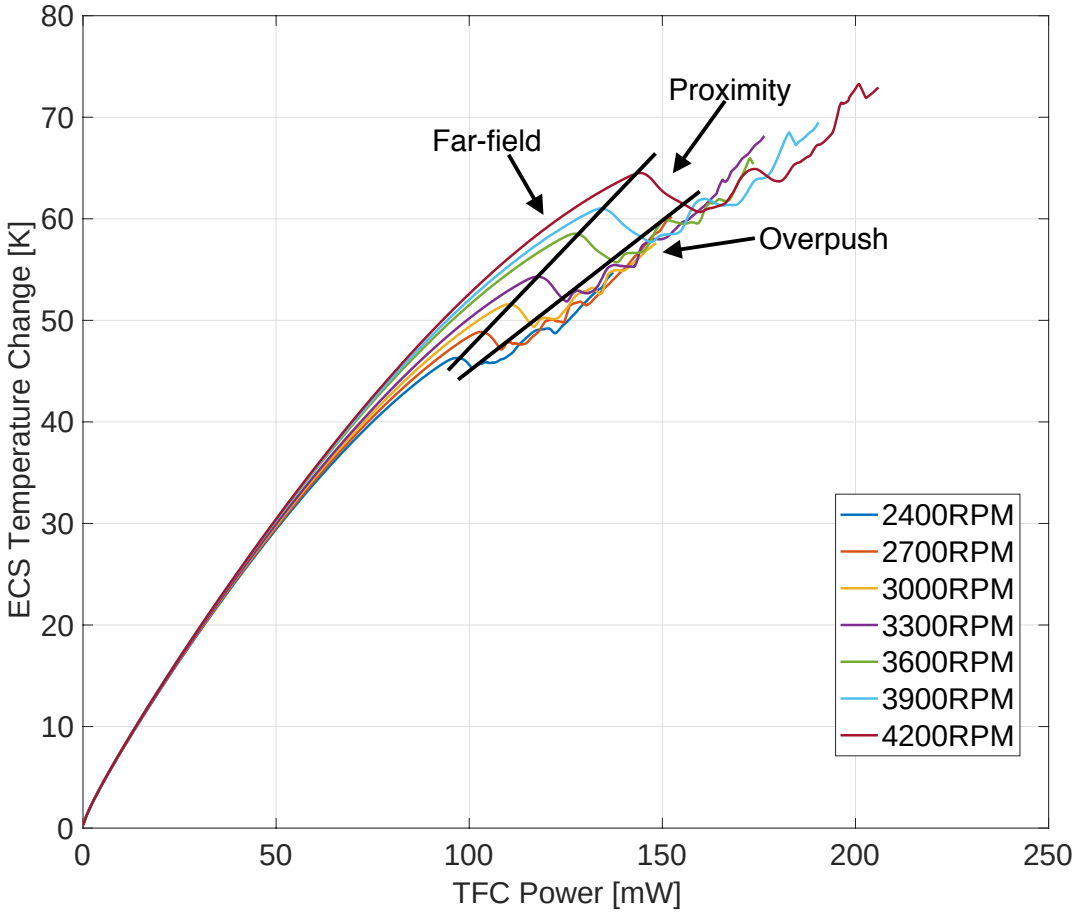

Figure 2.5: The temperature increase of the ECS vs. the TFC power. Different curves represent different disk rotating speeds.

coefficient. It has a very high bandwidth thus it has a fast response to the dynamic change of the HDI. Therefore it can also be used to detect disk defects such as asperities, pits, voids, lubricant moguls, etc. [43, 44, 45]. In this report, the ECS is mainly used as a temperature sensor on the slider's surface. The experiments related to it is discussed in Chapters 4 and 5.

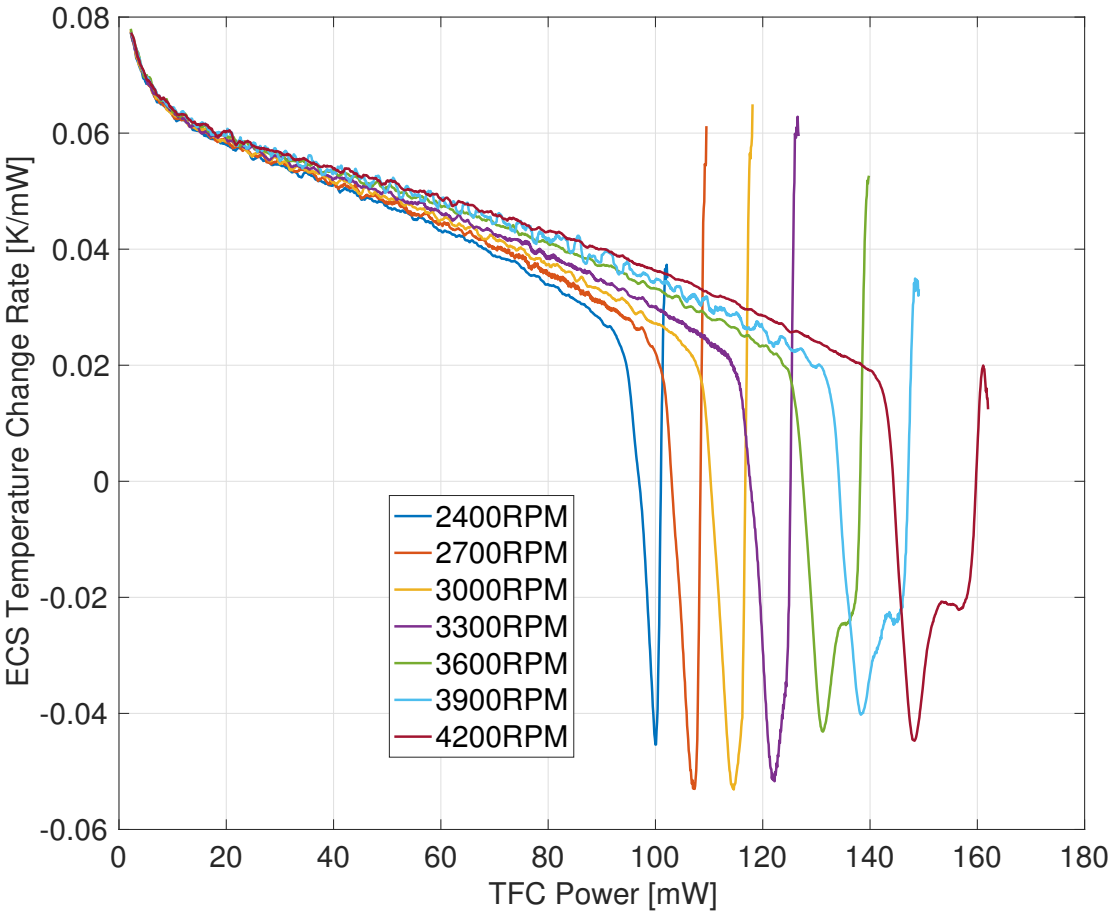

Figure 2.6: The rate of temperature increase of the ECS vs. the TFC power. Different curves represent different disk rotating speeds.

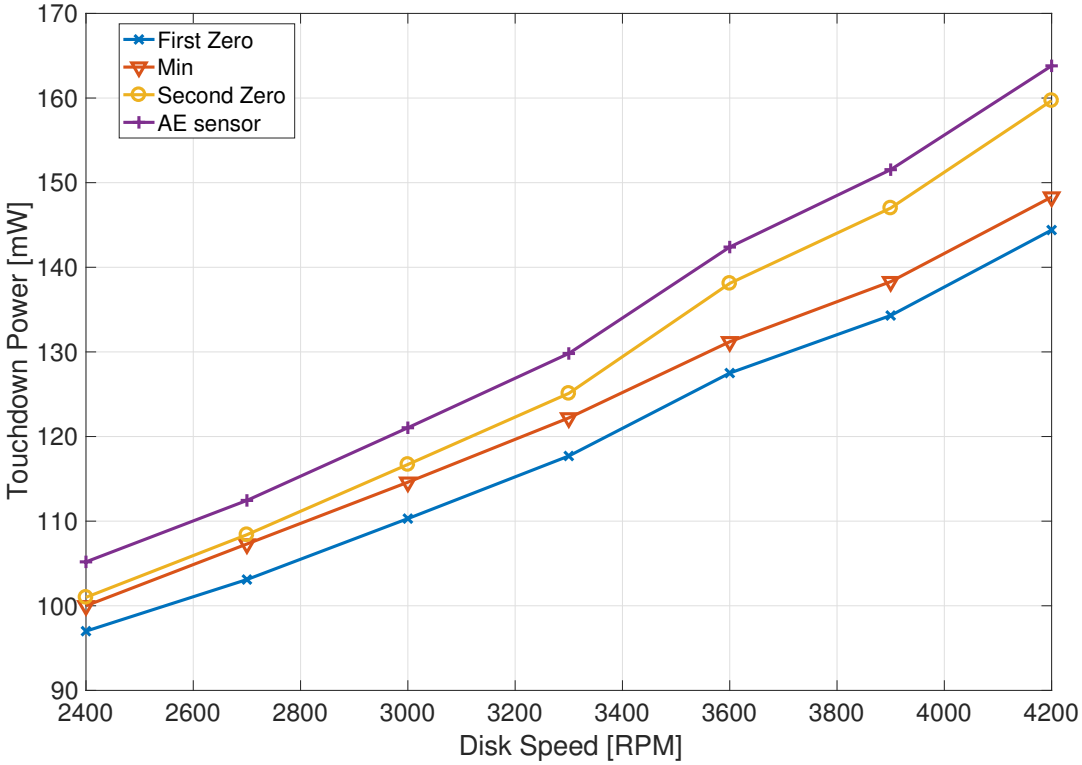

Figure 2.7: The TD detection using different methods. "First Zero", "Min" and "Second Zero" correspond to three key points in the derivative curves. "AE sensor" is the detection method using AE sensor.

2.3 Laser Power Delivering System

The laser power delivery system (LPDS) consisting of a laser diode (LD), a waveguide and a near field transducer (NFT) is an essential part of the HAMR system. Its function is heating the magnetic media to its Curie temperature during data writing. The basic introduction of the LPDS was discussed in Section 1.2. Its illustration is shown in Fig. 1.14.

NFT

The NFT is a critical part of the LPDS. There are several types of NFTs proposed for HAMR systems, mainly divided into two categories, apertures and antennas. Some designs of apertures include a circular hole with concentric grooves, C-shaped, L-shaped, bowtie-shaped, etc. Some designs of antennas include the lollipop-shape, beaked triangle, dual nanowires, etc [3]. The bowtie aperture type NFT and the lollipop antenna type NFT will be discussed here.

A top-down view of the bowtie NFT is shown in Fig. 2.8(a), which explains its naming. The two triangular components are placed symmetrically and tip to tip. The tip regions of the triangles are flat and there is a small gap between the two tips. Such a design can enhance the field intensity in the central region via the dual-dipole effect.

A detailed view of the lollipop type NFT is shown in Fig. 2.8(b). The lollipop NFT is designed by combining a circular disk with a peg. The NFT is located at the focus of a planar solid immersion mirror (PSIM), which plays a role as the waveguide [46]. The light is delivered to the NFT through the PSIM. Then the electromagnetic (EM) wave propagates on the circular disk and transfers the energy to the peg. The surface charge oscillates along the peg and finally generates an EM field at the tip via the lightning rod effect. Finally, the energy is delivered to the magnetic medium through coupling [4, 47]. In order to reduce self-heating of the lollipop NFT [48], a heat sink is attached to it through a bridge.

The EM field transmission and absorption in the NFT are modeled by the Maxwell equations,

$$\boldsymbol{\nabla} \cdot \mathbf{D} = \rho_V, \tag{2.3}$$

$$\boldsymbol{\nabla} \cdot \mathbf{B} = 0, \tag{2.4}$$

$$\boldsymbol{\nabla} \times \mathbf{E} = -\frac{\partial \mathbf{B}}{\partial t}, \tag{2.5}$$

$$\boldsymbol{\nabla} \times \mathbf{H} = -\frac{\partial \mathbf{D}}{\partial t} + \mathbf{J}, \tag{2.6}$$

where $\mathbf{D}$ is the electric displacement field, $\mathbf{E}$ is the electric field, $\mathbf{B}$ is the magnetic field, $\mathbf{H}$ is the magnetizing field, $\mathbf{J}$ is the electric current density, ρ_V is the electric charge density and t is time. For a linear and homogeneous medium, $\mathbf{D} = \varepsilon\mathbf{E}, \mathbf{B} = \mu\mathbf{H}$, where ε, μ are the medium's permittivity and permeability. For conductors, Ohm's law is assumed to apply: $\mathbf{J} = \sigma\mathbf{E}$, where σ is the electric conductivity. Ohm's law is not valid at the $\sim$2 nm-thick

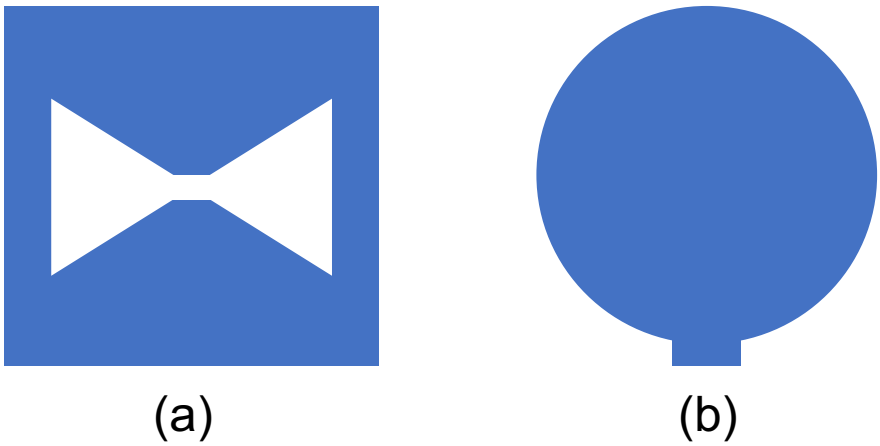

Figure 2.8: (a) Bowtie NFT profile. (b) Lollipop NFT profile

layer of the metal surface [49]. However we neglect this effect here and assume Ohm's law applies in the entire body.

When EM waves propagate in a lossy medium such as metal, some EM energy is converted to heat. The general expression of such a conversion is [50]

$$\dot{q}_{abs} = \frac{1}{2}\,\mathrm{Re}(\sigma)|\mathbf{E}|^2 = \frac{1}{2}\varepsilon_0\omega\,\mathrm{Im}(\varepsilon_r)|\mathbf{E}|^2, \tag{2.7}$$

where $\dot{q}_{abs}$ is the absorbed power density, ε_r and ε_0 are the relative and vacuum permittivities, respectively, and ω is the angular frequency of the EM wave.

A simulation was performed using the finite-difference time-domain (FDTD) method, solving the Maxwell equations using the finite difference method in the time domain. One advantage of the method is that it deals with a wide frequency range with one simulation run. It is widely used in NFT modeling [48, 51].

The simulation domain includes the waveguide, the NFT and the media stack, since the EM field intensity in these regions is much larger than in their surroundings. The domains with the lollipop NFT and the bowtie NFT are shown in Figs. 2.9(a)(b), respectively. In both cases, we assume that the laser light comes into the waveguide with a 2D Gaussian distribution. The wavelength is 800 nm. The EM field generated by the head's writer and the magnetic layer in the media are neglected. The NFTs material is chosen as gold (Au), and the geometry of the NFT is optimized to deliver a hot spot with the size of $\sim 50 \times 50\,\mathrm{nm}^2$ in full-width-half-maximum (FWHM). The simulations were performed using the Lumerical FDTD Solutions, a commercial FDTD Maxwell equation solver.

The results of the EM field simulations are shown in Fig. 2.10. Figs. 2.10(a)(b)(c) show the normalized power absorption profiles in the HDI region for the bowtie NFT design in different views. Fig. 2.10(a) is the cross-sectional view of both the bowtie NFT and the media. It shows that the media has more power absorption than the NFT. Fig. 2.10(b) shows

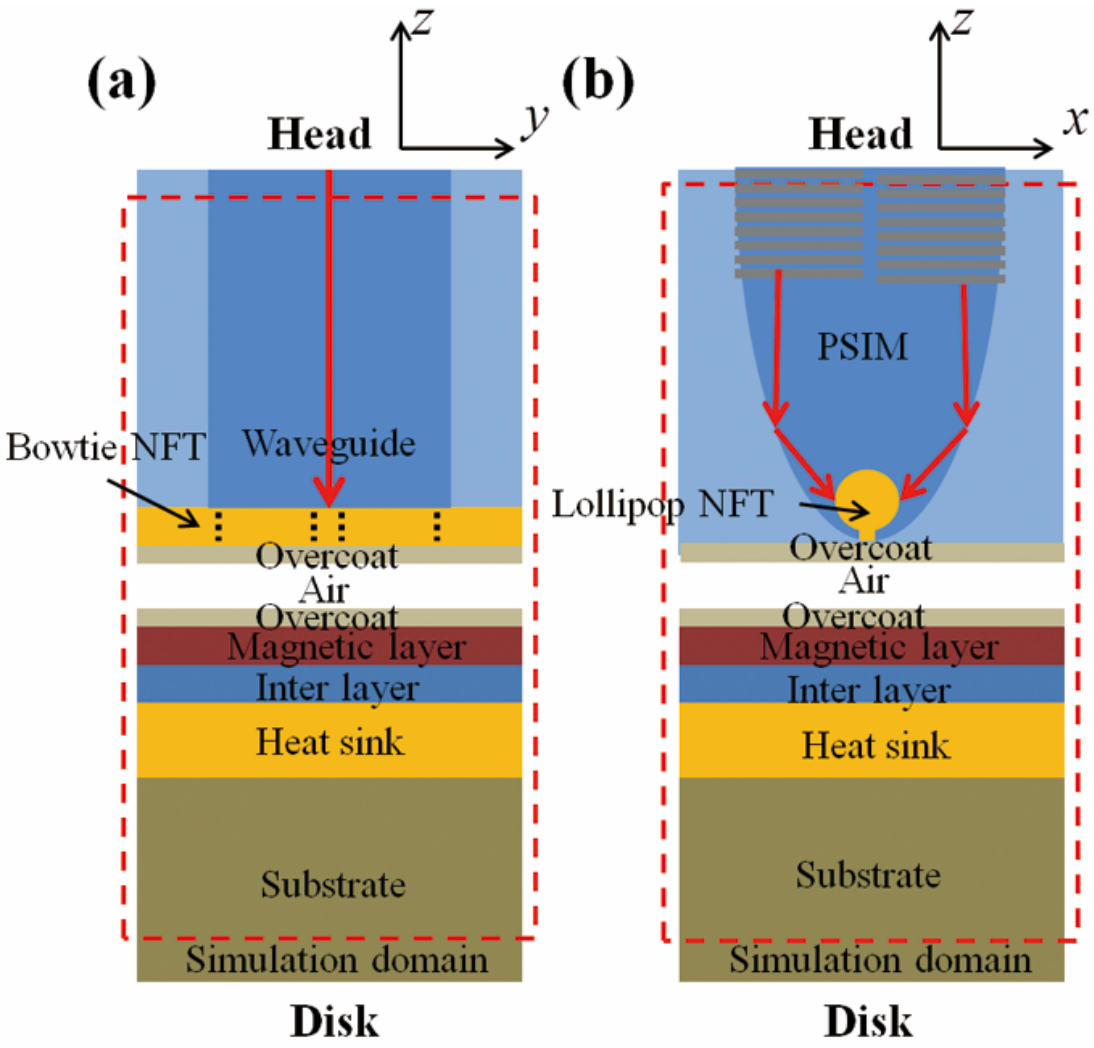

Figure 2.9: (a) EM field simulation domain with bowtie NFT. (b) EM field simulation domain with lollipop NFT.

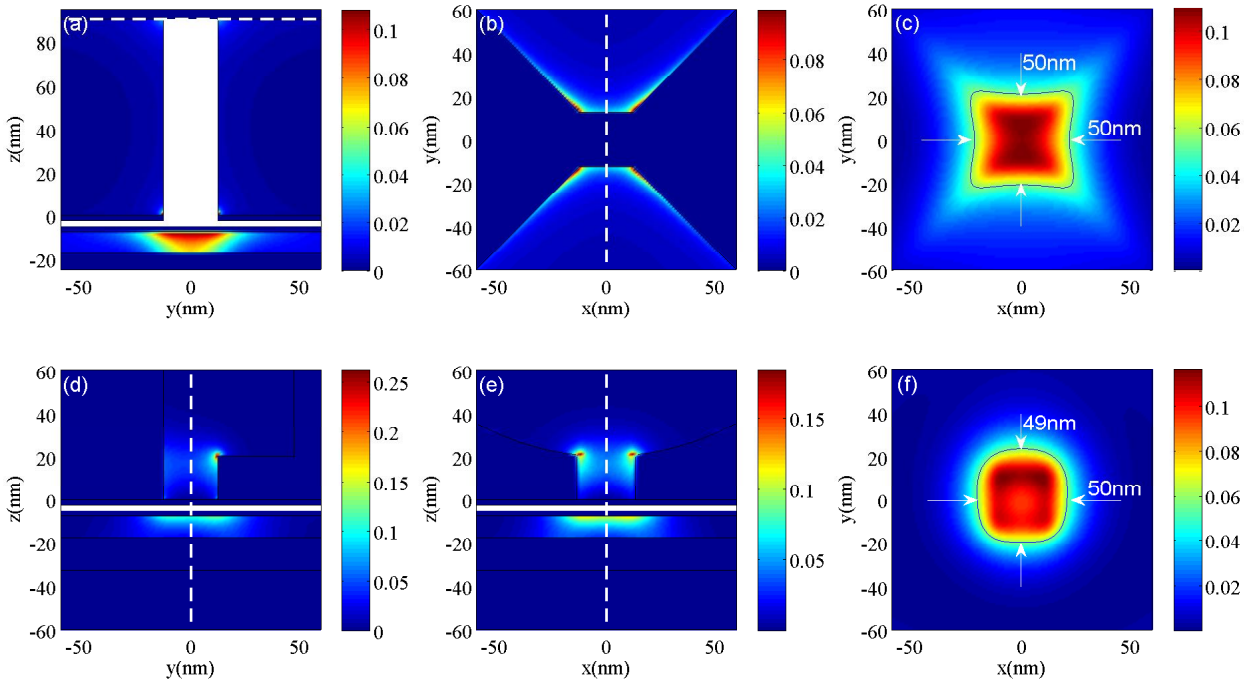

Figure 2.10: (a)(b)(c) show the normalized absorbed power profiles of the NFT and the media in the bowtie NFT. (a) shows one cross-sectional view, while the direction and the position of the cut is shown at the dashed line in (b). (b) shows the view of the surface of the NFT, which is not facing the media. The position of the surface is indicated as the dashed line in (a). (c) shows the view of the surface of the magnetic layer of the media. (d)(e)(f) show the normalized absorbed power profiles of the NFT and the media in the lollipop NFT. (d)(e) show two cross-sectional views of the NFT and the media, while the directions and the positions of the cuts in (d) and (e) are shown as the dashed lines in (e) and (d), respectively. (f) shows the view of the surface of the magnetic layer of the media. It is noted that the colorbars have different scales.

the view of the top surface (the non-ABS surface) of the NFT. The absorption is intense at the tips. Fig. 2.10(c) shows a view of the top surface of the media's magnetic layer. The FWHM of the hot spot induced by the NFT is $50 \times 50\,\mathrm{nm}^2$. The coupling efficiency, defined as the ratio of the absorbed power on media to the total laser power, is 3.4%.

Figs. 2.10(d)(e)(f) show the normalized power absorption profile in the HDI region with the lollipop NFT design in different views. Figs. 2.10(d)(e) show the cross-sectional views in different directions. It can be seen that the absorption of the lollipop NFT is comparable to that of the media, and it is mainly concentrated in the connection between the peg and the disk, which may cause a strong self-heating in the NFT, in addition to the back-heating from the media. That is why the heat sink is needed in the lollipop design. Fig. 2.10(f)

shows a view of the top surface of the media's magnetic layer. The FWHM of the hot spot induced by the NFT is $49 \times 50\,\mathrm{nm}^2$. The coupling efficiency is 5.7%.

Since the NFT is only a few nanometers away from the heated media, strong back-heating can occur which can cause additional heating on the NFT. For more about how the back-heating can affect the NFT, please refer to Refs. [52, 53, 54].

Waveguide Heads

The recording heads with a partial LPDS were provided to CML for the experiments. Each head has an embedded LD and a waveguide, but no NFT is attached at the end of the waveguide. Therefore, the laser light at the end of the waveguide reaches the media directly. To distinguish these heads from the heads used in the actual HAMR application, they are called "waveguide" heads. Although there were no NFTs in the heads, they can still generate a laser beam and focus the beam to the scale of 500 nm. Without the blocking of the NFT, 100% of the optical energy out of the waveguide is passed to the media. Therefore, the waveguide heads can be used to simulate the HAMR condition.

The LD in the waveguide head is controlled by constant current or voltage. The property of the LD is similar to a normal diode. To protect the LD from excessive current, a resistor of $50\,\Omega$ is connected to it in series. By measuring the voltage drop of the LD and the total supplied voltage, the current through the LD can be calculated. The electrical connection of the LD is shown in Fig. 2.11.

The LD's equivalent resistance and its consumed power vs the laser current are shown in Fig. 2.12. It is seen that the LD's equivalent resistance drops from infinity to about $50\,\Omega$ as the laser current increases from zero to 60 mA. It is also seen that the LD's consumed power is 180 mW when the laser current is at 58 mA. It is noted that the LD's consumed power is not equivalent to its optical power, since some heat loss occurs when powering the LD.

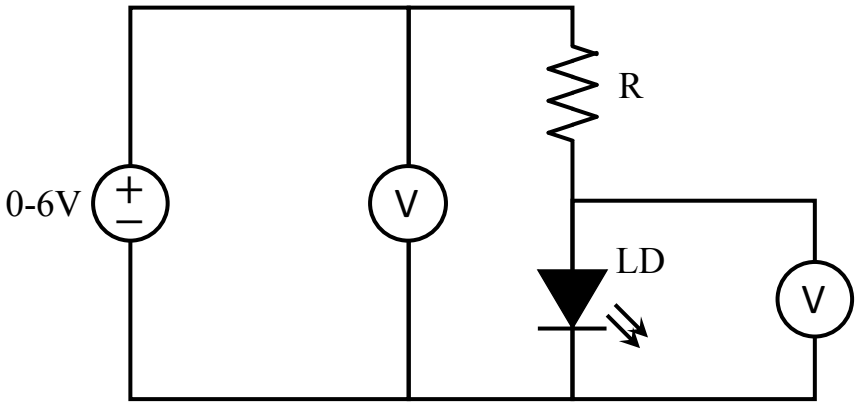

Figure 2.11: The electrical circuit to measure the equivalent resistance of the laser diode.

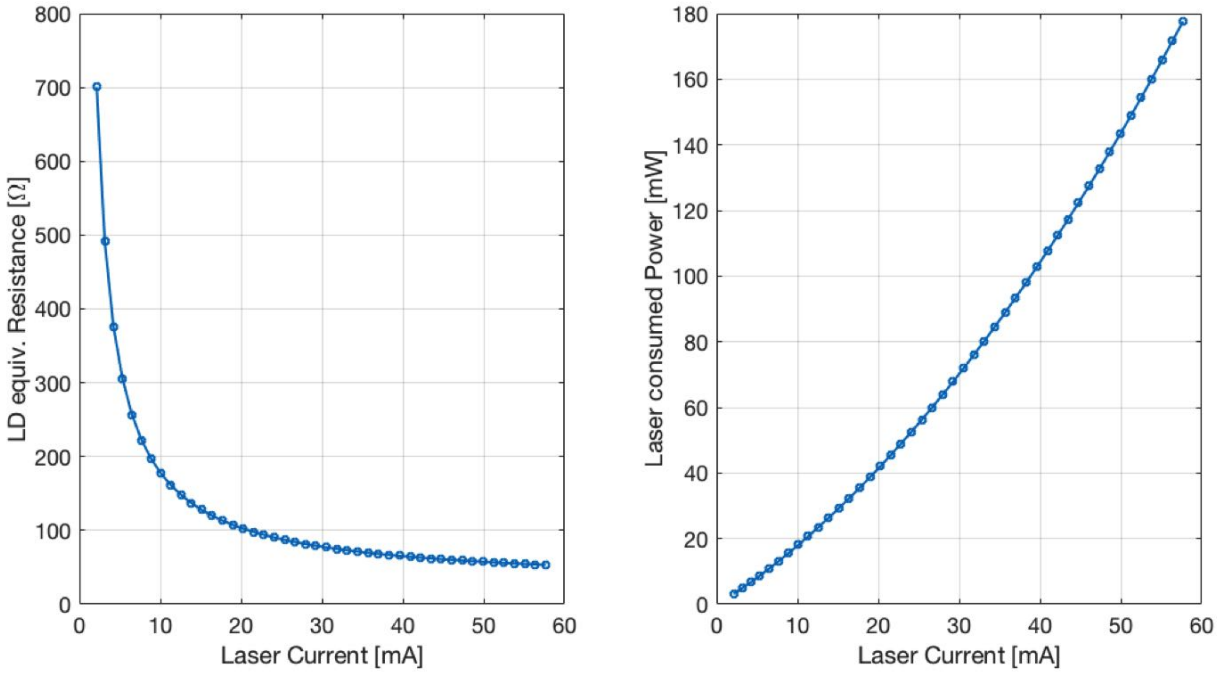

Figure 2.12: The characteristics of the laser diode.

2.4 Summary

In this chapter, three electrical components in the HAMR slider were introduced. They are the TFC heater, the ECS and the LPDS. The TFC heater is a resistor in the slider's body to lower the FH using the thermal expansion effect. The ECS is a temperature sensor located at the ABS to detect head-disk contact. The LPDS is a complex optical system that is essential in HAMR. It consists of the LD, the waveguide and the NFT to generate and focus the EM energy on to the magnetic media into the sub-diffraction regime. In our experiments, the TFC heater, the ECS and the partial LPDS without NFT are available.

Chapter 3

The Experimental Setup

This chapter briefly introduces the experimental stages and devices used in the HDI study. Among all the equipments, the in-house developed HAMR stage plays an essential role, carrying out most experiments, as introduced in Section 3.1. The ECS calibration stage introduced in Section 3.2 is a special purpose stage used for the calibration of the temperature coefficient of resistance of the ECS. The chapter is summarized in Section 3.3.

3.1 The HAMR stage

An experimental stage that is capable of emulating the HAMR condition was designed and developed in CML, called the CML-HAMR stage. The majority of the components in the stage sit on an air table under a clean hood. Some electrical components that are not prone to microscale particle contamination sit outside the clean hood due to space limitation. An overview photograph of the stage is shown in Fig. 3.1.

A schematic view of the stage, including these modules, is shown in Fig. 3.2. As can been seen in the figure, the stage consists of an optical module, a spinstand module and a signal generation/acquisition module. The optical module is designed to generate and deliver a beam of free-space laser light with FWHM of $\sim 2\,\mu m \times 5\,\mu m$ focused on the surface of the rotating disk. The spinstand module is used to control the spinning of the disk and the position of the HGA. The signal generation/acquisition module is used to generate the control signal to power different actuators such as the TFC heater and the laser, and to record electrical signals from the system such as the ECS and the AE sensor. Each module will be introduced below.

The Optical Module

The optical module of the CML-HAMR stage consists of a laser generator, a series of intermediate optical lenses and a final focusing lens. A schematic of the optical module is shown in Fig. 3.2. The laser generator emits a laser beam with the optical power up to 1 W at the

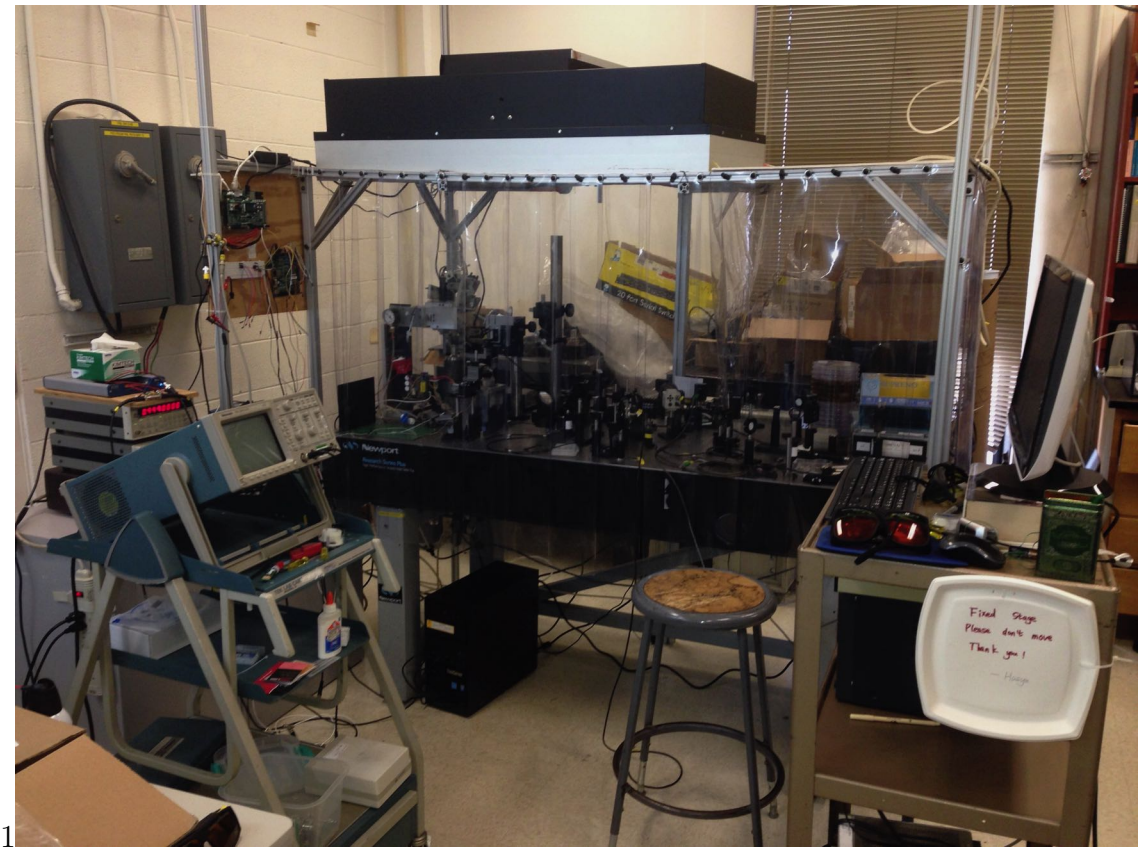

Figure 3.1: An overview picture of the CML-HAMR stage.

wavelength of 780 nm. The laser beam passes through a series of optical lenses such that the beam is parallel (neither convergent or divergent) before reaching the final focusing lens. The final focusing lens has a relatively small focal length of 50 mm and is very close to the rotating disk. The distance between the focusing lens and the disk is finely adjusted such that the laser beam is well focused on the disk. A digital camera with an optical splitter is used to check the focusing. If a clear image of the laser beam profile shows on the camera's image, it means the laser is well focused. Fig. 3.3 shows an example of a well focused beam and Fig. 3.4 shows an example of an unfocused beam.

The Spinstand Module

The spinstand module is the mechanical part of the stage. As seen in Fig. 3.2, the module consists of two parts, a disk spindle with speed control and a head positioning assembly.

The disk spindle system consists of a disk holder, a motor with a motor driver, an optical encoder and a field-programmable gate array (FPGA) board. The disk holder can clamp the disk platter concentric to the motor's shaft. Once the disk platter is fixed properly on

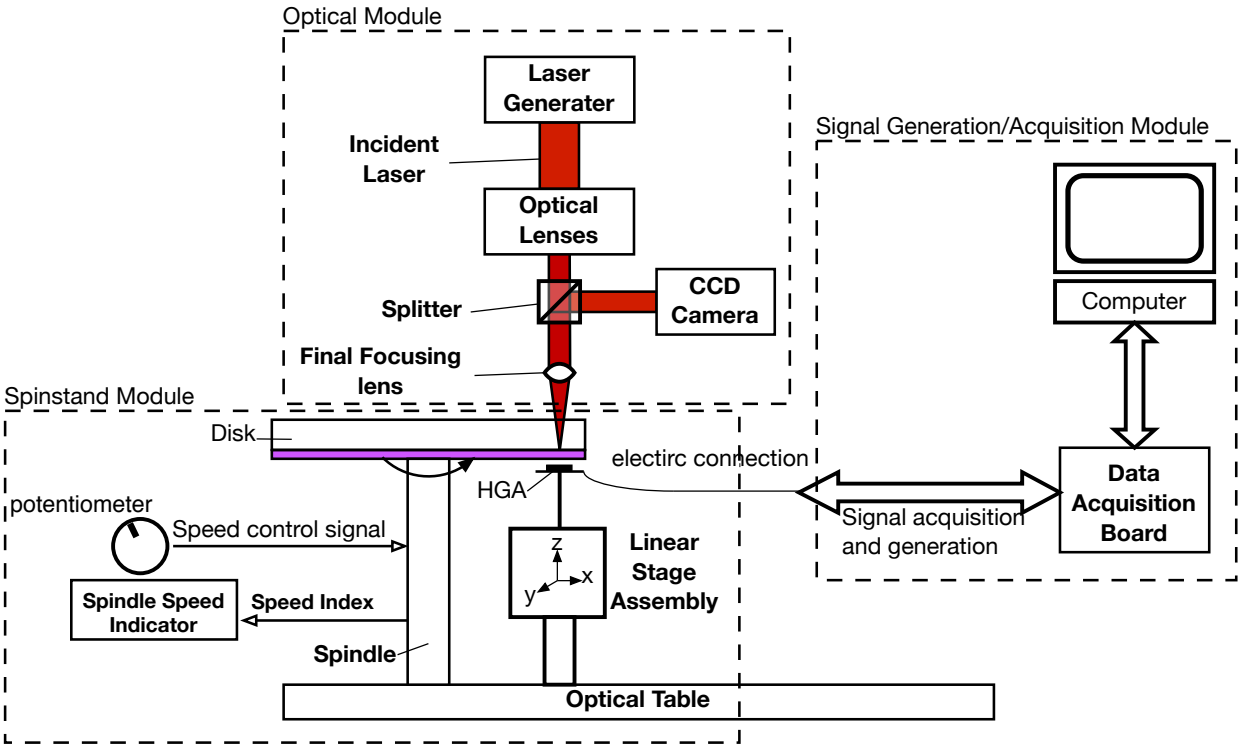

Figure 3.2: Schematics of the CML-HAMR stage.

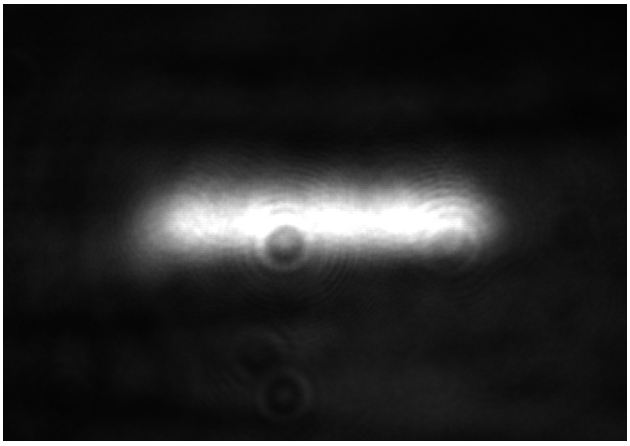

Figure 3.3: The image of a focused laser beam captured by the camera.

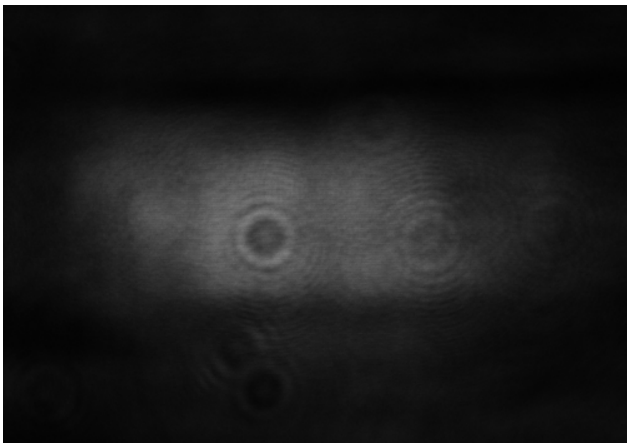

Figure 3.4: The image of an unfocused laser beam captured by the camera.

the spindle, the motor attached to the spindle is turned on, spinning the disk. An optical encoder is embedded on the motor such that the rotating speed of the motor can be acquired by counting the rising/falling edge of the encoder's signal. The encoder used in the stage has 1024 teeth therefore every 1024 counts of the rising/falling edges of the encoder's signal represents one revolution of the disk. A National Instrument FPGA board is used to process the encoder's signal, and the disk rotating speed is shown on the on-board display in real time. A potentiometer attached to the motor's driver is used to adjust the disk rotating speed. Therefore, the disk's rotating speed can be controlled in the range of 60 to 5800 RPM.

The HGA's position needs to be set properly relative to the disk's position, including the flying radius, the yaw angle and the Z-height. In the system, the HGA is first attached to an HGA fixture, as shown in Fig. 3.5. Then the HGA fixture is attached to an assembly consisting of three linear translation stages, the so-called linear stage assembly. The three stages are used for positioning the head in three directions, X, Y and Z. The three linear stages are assembled perpendicular to each other and they are fixed on a plane parallel to the air table. The three axes of the linear stage assembly are finely adjusted such that the head has proper Z-height, radial position and yaw angle with respect to the disk. The entire assembly, including the linear stage assembly and the HGA fixture, is called the head positioning assembly. A picture of the head positioning assembly is shown in Fig. 3.6. On the other hand, the HGA fixture also has an electric connection port that is used to connect the electric components of the HGA (the TFC heater, the ECS, the LD, etc) to the external circuit. Therefore, the electric components in the head can be connected to and controlled or monitored by the signal generation/acquisition module.

In summary, the disk can rotate at a desired rotating speed and the head can be positioned properly. The electric components inside the head can also be controlled and monitored. The system is setup both mechanically and electronically.

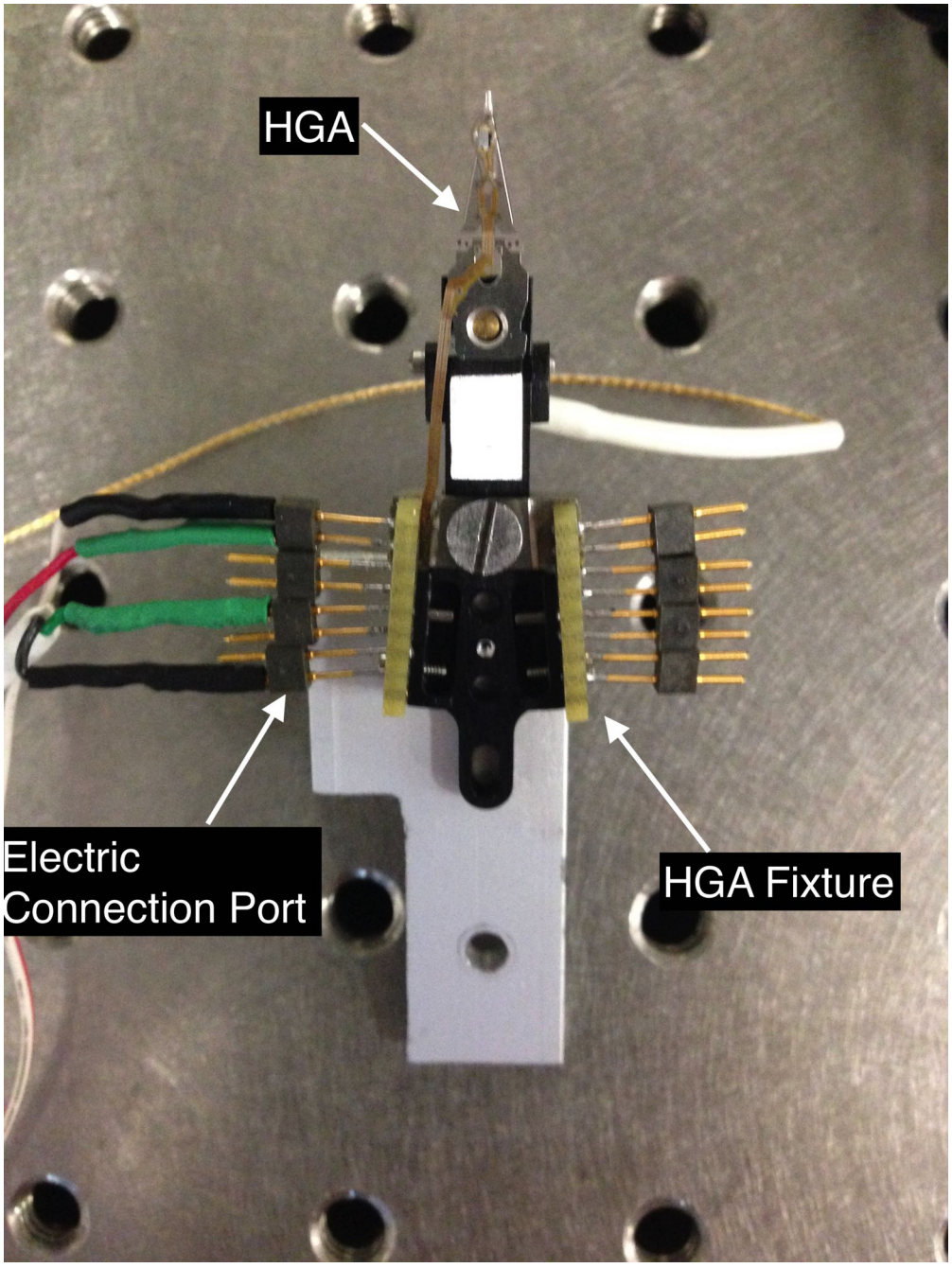

Figure 3.5: A picture of the HGA fixture.

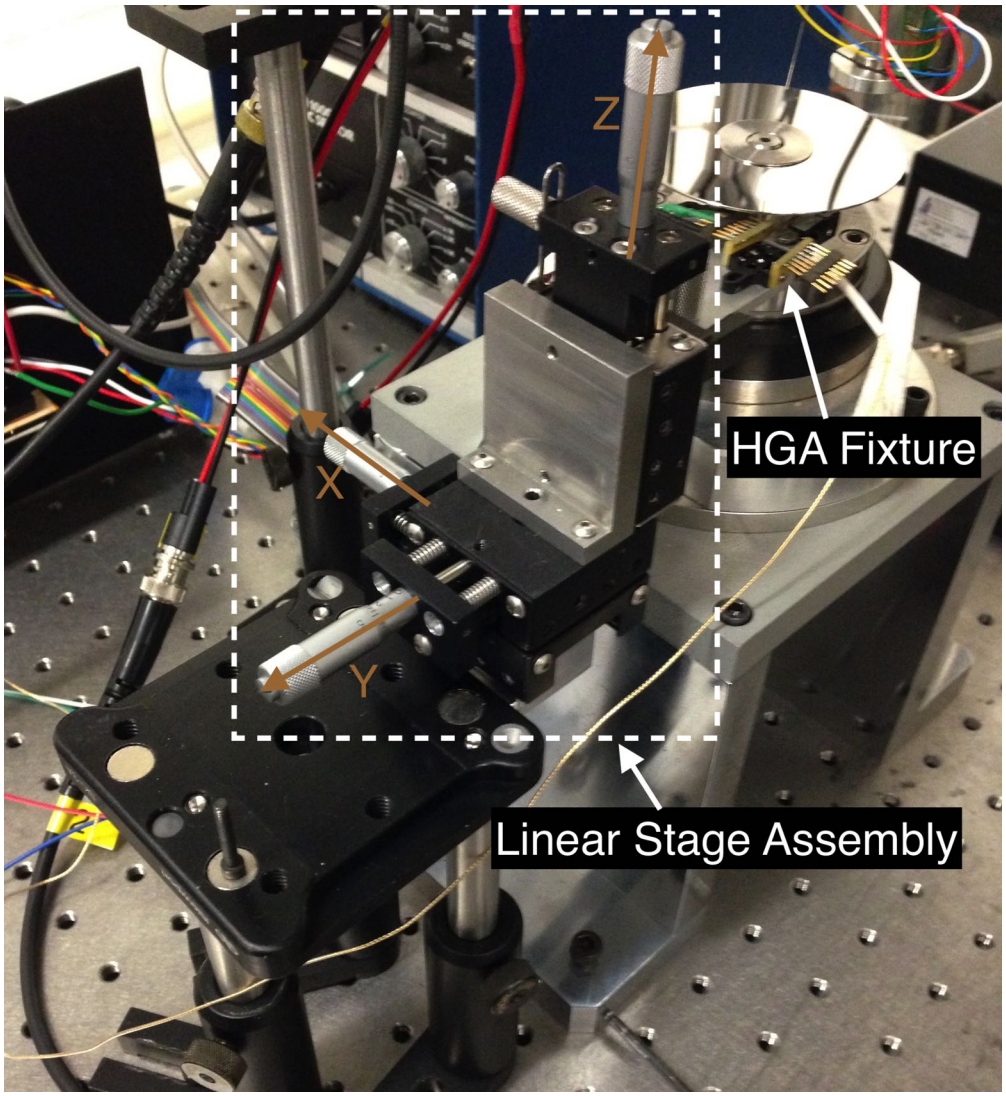

Figure 3.6: A picture of the head positioning assembly. The HGA (not shown in the picture, hidden by the disk platter) is attached to the HGA fixture. The HGA fixture is fixed on the linear stage assembly. The linear stage assembly consists of three linear translation stages, which are used to adjust the position of the HGA in three axes. The linear stage assembly sits on an elevated platform which is parallel to the air table. The disk spindle can also be seen in the picture.

Signal Generation/Acquisition Module

While the stage is setup properly in the mechanical, electrical and optical aspects, the experimental procedures need to be controlled and the data from the experiment needs to be gathered. Therefore, the signal generation/acquisition module is setup in a software for controlling and monitoring.

The signal generation/acquisition module consists of a National Instruments data acquisition (DAQ) board (Model PCIe-6353) attached to a desktop computer, as shown in Fig. 3.2. The board has 16 analog input (AI) channels and its max acquisition rate is 1.25 MS/s for single channel. It also has four analog output (AO) channels which can be used for controlling the TFC heater and the laser diode. It is noted that the DAQ board's power is not adequate to maintain a high TFC power or laser power since it also requires high current through the electrical components. Therefore, a voltage follower is needed between the DAQ board's AO port and the electric components to avoid the load effect.

During the experiments, all components whose signals are to be acquired, such as the ECS or the AE sensor, are connected to the AI channels, and all components to be controlled, such as the TFC heater and the laser diode, are connected to the AO channels. The experimental procedures are designed in the National Instruments LabView software to perform tasks such as the touch-down procedure or constant laser heating procedure. The LabView programs can save the acquired signal data from the DAQ board into digital files on the computer for further data processing.

3.2 ECS Calibration Stage

The ECS calibration stage is designed to calibrate the temperature coefficient of resistance of the ECS. It is a thermally controlled chamber with a hot plate used to heat the air inside the chamber, as shown in Fig. 3.7. In the chamber, there is a HGA fixture, a fan and an optical barrier. During the calibration, the HGA is attached to the fixture, while its ECS is connected to an ohmmeter. The hot plate is set to a certain power. The fan is turned on to circulate the air in the chamber in order to create a uniform air environment. The optical barrier sits between the hot plate's surface and the HGA fixture to avoid direct radiative heating. A thermometer is placed beside the HGA to measure the air temperature. When the temperature inside the stage is stable, the environment's temperature and the ECS' resistance are recorded. Then α_0 can be calculated based on Eq. 2.2. The details of the ECS calibration result are discussed in Section 4.3.

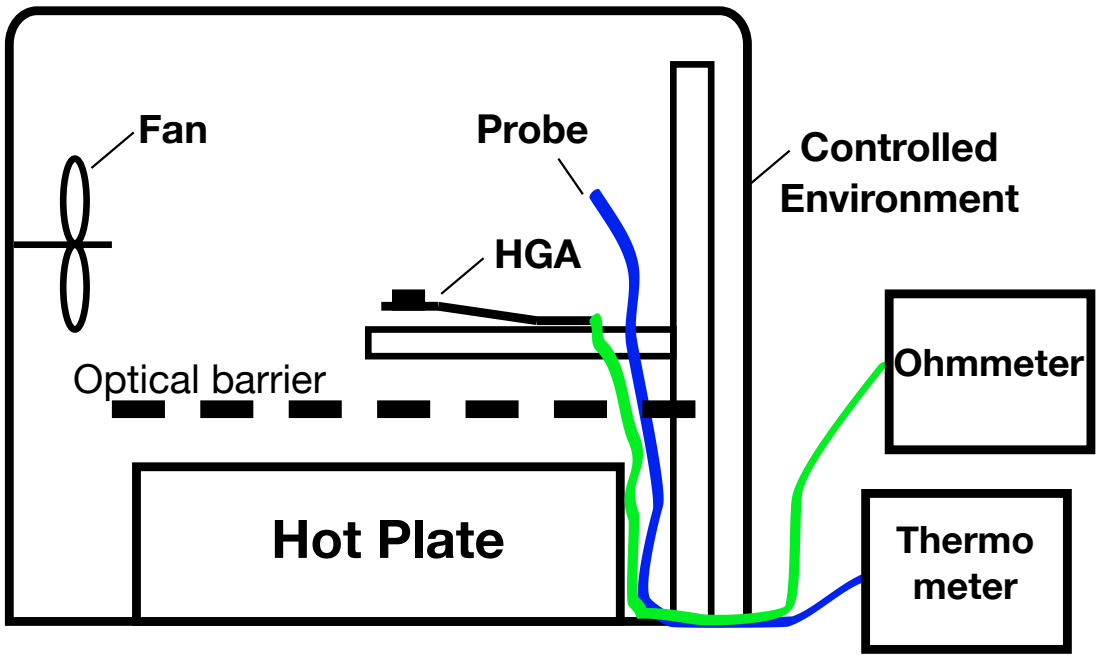

Figure 3.7: A schematic of the ECS calibration stage.

3.3 Summary

In this chapter, two experimental stages designed and setup in CML, the CML-HAMR stage and the ECS calibration stage, were introduced. While the ECS calibration stage is specially made for the ECS calibration, the CML-HAMR stage is designed to be generic with great flexibility. The CML-HAMR stage is comprehensive including the optical, mechanical and electrical systems controlled by the software. With the CML-HAMR stage, the head-disk interface experiments can be done for both PMR and HAMR. With the free space laser focused on the disk, the HAMR condition can be emulated. As will be seen in Chapter 6, when a waveguide head is used, the HAMR scenario can be achieved without the external free space laser. Nevertheless, the full setup of the CML-HAMR stage creates high flexibility for the experiments.

Chapter 4

Measuring the Head's Temperature When Heated by a Free Space Laser

4.1 Introduction

As introduced in Section 2.3, the NFT is made of a metal such as gold (Au) and rhodium (Rh), and it requires precise geometry for efficient EM coupling. Therefore the NFT should remain at a relative cool temperature to avoid deformation and material diffusion caused by the heat. However, the NFT is only ∼1 to 10 nm away from the media which is heated to the magnetic layer's Curie Temperature (∼ 450 °C). Therefore, heat flows back from the disk's heated spot to the NFT thus raising the temperature of the NFT by an unknown amount. This phenomenon is called "back-heating". As the gap between the NFT and the hot media approaches a couple of nanometers, the back-heating from the hot media will be significantly enhanced and may cause an undesired temperature rise on the NFT, which could cause a reliability issue for the entire HAMR system.

Therefore, it becomes vital to understand the heat transfer between two surfaces with nanoscale separations. A few theoretical models have been proposed and some experiments have been performed to verify the models [21, 43, 55, 56, 57, 58, 59, 60, 61]. Chen et al. [55] used an air bearing cooling model to predict the heat transport and the temperature distribution on the slider surface. This model holds for most cases when the temperature difference is around or less than 100 K and has been used for several different applications in the past ten years [21, 43, 56]. However, this model only takes air conduction into account and may become less applicable when a significant amount of radiation and conduction occurs. Narayanaswamy and Chen [57] set up a radiative heat transfer model between two spheres and corresponding experiments were performed [58]. However, the model is only examined for gaps greater than 30 nm. Recently, Budaev and Bogy [59, 60, 61] established a phonon tunneling model to predict nanoscale heat transport. They pointed out that the correlations between two surfaces cannot be neglected when the distance between the two surfaces is within the range of the radiation's wavelength, and therefore it may contribute to

the heat transport. Since the nanoscale heat transfer mechanism is still actively investigated, it is hard to create an accurate numerical model to predict the NFT's temperature during the HAMR heating process. Therefore it is vital to measure its temperature experimentally.

In this chapter, a recording head with the ECS and the TFC heater and a rotating disk are used to create two flat surfaces that are a few nanometers apart [62, 63]. A beam of free space laser is focused onto the back side of the disk to heat it to the HAMR writing condition. The TFC heater is used to control the gap separation and the ECS is used to sense the temperature on the head. With this experiment, the temperature rise on the head due to the laser heating of the disk can be estimated. Such an estimate can also contribute to the understanding of the nanoscale heat transfer mechanism.

The rest of the chapter is organized as follows. Section 4.2 discusses the basic principle of the system setup. It explains how the HAMR condition is simulated by the current stage design and how the head's temperature is estimated. Section 4.3 discusses how the ECS is calibrated and how to measure the disk's temperature. Section 4.4 introduces the process of the experiment. Section 4.5 discusses the experimental result and the prediction of the head's temperature in the HAMR condition. The chapter is summarized in Section 4.6.

4.2 System Setup

Usually, it is hard to maintain a nanoscale air or vacuum gap between two large (at least in microscale) flat surfaces. However, this happens inherently in HDDs, where the FH can be maintained in a range of several nanometers with a modern production head. Moreover, the FH can be controlled at 1 nm with the TFC heater .

In HAMR conditions, the temperature of the media is higher than that of the head. In order to simulate this condition, a free space laser is focused on a one-side coated glass disk, while a recording head is flying. The side of the disk that is facing the head (front side) is coated with a 100 nm thick NiTa layer, which is commonly used for HAMR media study [64]. Then a COC layer and a lubricant layer are deposited on it to ensure flyability [65, 66, 67]. The other side of the disk (back side) is left with no further processing. The free space laser light of 780 nm is illuminated on the back side of the disk, passing through the glass substrate and focusing on the metal layer. The metal layer of the disk is thick enough to ensure that no laser light leaks through the layer. As a result, the focused spot is heated by absorbing the optical energy from the laser. This setup is called the "back-heating" setup, as shown in Fig. 4.1.

Although the laser heating spot is on the order of a few microns in our experiment, which is much larger than the heated spot in the real HAMR system, the heat transfer mechanism in our experiment and the HAMR system should be the same, regardless of the size of the heated spot as long as the heated area is much larger than the gap. In that case the heat transfer can be modeled by two flat plats separated by a constant gap. In fact, such a micron sized heating spot is beneficial for studying the mechanism as the temperature profile is more uniform across the temperature sensing location.

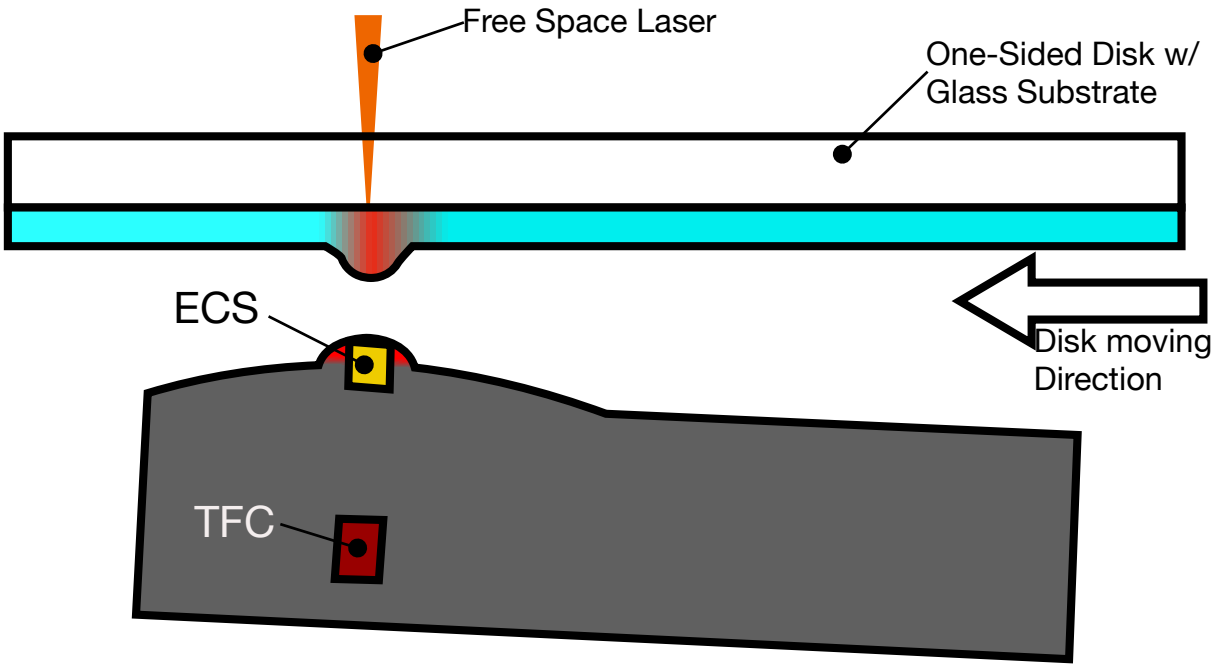

Figure 4.1: A diagram of the back-heating experiment. The head is flying on the one-side disk. The ECS and the TFC are explicitly shown but other components are omitted. The free space laser is illuminated from the back of the disk and focused on the metal-coated side.

As the disk is heated by the free space laser, the temperature difference between the head and the disk is created. Since the ECS is located on the surface of the head, it can detect the laser heating when its position aligns well with the hot spot. Additionally, the FH is controlled by powering the TFC heater. It is noted that the TFC heater inside the head also raises the temperature of the slider and the ECS senses this as well. In other words, the ECS is heated by the TFC heater in the head, which is referred to as "TFC-heating", and by the heat flow from the hot spot on the media which is called "back-heating". Or in equation,

$$\theta_E = \theta_E^L + \theta_E^T, \tag{4.1}$$

where θ_E is the total temperature increase of the ECS from T_0 ($\theta_E = T_E - T_0$, where T_E is the current temperature of the ECS). The superscripts $\cdot^L$ and $\cdot^T$ indicate that the temperature change is caused by the laser heated spot on the disk or the TFC heater, respectively. In the experiment, θ_E can be acquired by ECS measurements with the laser turned on for a fixed TFC power (P_T). On the other hand, θ_E^T can be acquired with the laser turned off for the same TFC power. And the difference is the portion of the temperature rise caused solely by the laser heating of the disk.

4.3 Temperature Calibration of the Head and Disk

The temperatures of both the ECS and the disk heated spot need to be known in order to investigate the relationship between the temperature rises of the two surfaces. Therefore, the temperatures of both surfaces need calibration.

The disk is heated by the free space laser allowing the temperature of the disk surface (T_D) to be controlled by applying different laser powers (P_L). It has been shown that the peak temperature rise on the rotating disk surface is linearly proportional to the laser power when the disk rotating speed is constant [64, 68].

As a consequence, this linear relationship can be easily calibrated by using a thin phase change film the microstructure of which changes when the phase change temperature is reached.

A glass disk coated with a 20 nm phase change material which has a phase change temperature at 300 °C was used for the calibration [69]. The laser was focused on the metal surface through the disk's glass back side at the room temperature of 25 °C. The topography of the phase change material also changes as the disk temperature approaches the phase change temperature. The topography change can be measured by an atomic force microscope (AFM). Fig. 4.2 shows the disk temperature calibration results. It can be seen that phase change shows at the laser power of 275 mW. This calibration indicates that the equivalent disk temperature increases by 1 K when the laser power increases by 1 mW.

The temperature coefficient of resistance of the ECS (α_0) also needs calibration according to Eq. 2.2 in order to convert its resistance to its temperature. α_0 was calibrated in the ECS calibration stage as described in Section 3.2. During the calibration, the head with the ECS was located in the stage while the ECS' resistance was monitored. The hot plate was turned to a certain temperature. When the temperature inside the stage was stable, the environment's temperature and the ECS' resistance were recorded. Different temperatures were set by the hot plate to get a series of data.

The result of this calibration is shown in Fig. 4.3. A linear regression of the measurement yields $\alpha_0 = 3.5 \times 10^{-3}/\mathrm{K}$.

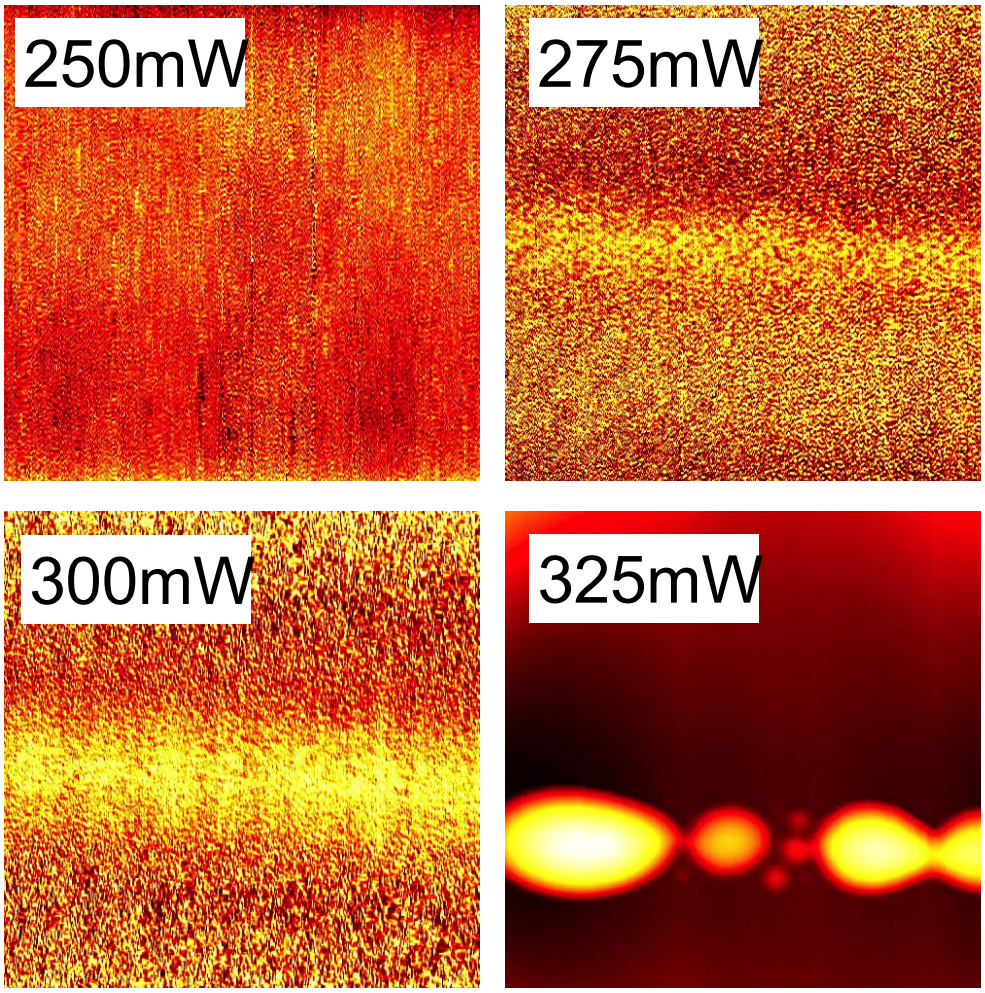

Figure 4.2: AFM images of the phase change disk after laser heating. Different subplots show different laser powers.

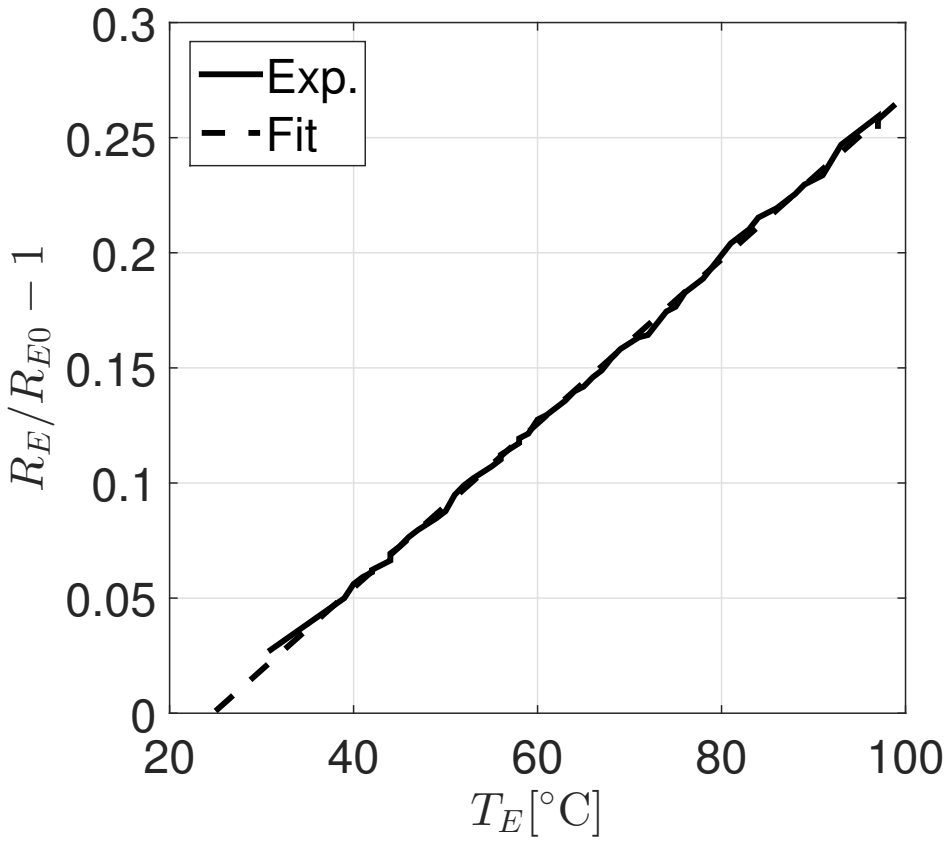

Figure 4.3: The calibration curve for the ECS. The solid line is the experimental curve and the dash line is the fitted curve.

4.4 Experimental Procedure

With the head and disk temperature calibration data available, the back-heating experiment can be done. As discussed above, a beam of laser illuminates the back of the disk with the beam size in microns. As the disk rotates at 4200 RPM and the head flies stably around the outer radius of the disk, the position of the laser beam is finely adjusted such that the ECS on the ABS is positioned directly above the heated spot on the disk. This also gives the maximum temperature increase of the ECS. The temperature of the ECS increases due to the heat transfer between the disk and the ABS. When this setup is completed, only the laser power (or equivalently disk temperature T_D) and TFC power (P_T) will change. Therefore, Eq. (4.1) leads to

$$\theta_E^L = \theta_E(T_D, P_T) - \theta_E^T(P_T) = \theta_E^L(T_D, P_T). \tag{4.2}$$

It is to be noticed that θ_E^T is a function of only the TFC power (P_T), because θ_E^T represents the ECS temperature rise solely caused by the TFC heater when there is no laser power, i.e., $P_L = 0\,\text{mW}$. So θ_E^L is a function of disk temperature (T_D) and TFC power (P_T).

During the experiment, the laser was adjusted initially to a certain power and remained fixed during one set of experiments. For each value of laser power, the voltage of the TFC heater was controlled as a ramp function. The AE signal was monitored to detect the head-disk contact [70, 71]. In this way the ECS resistance (R_E) was acquired.

When the laser is turned off, the ECS is only heated by the TFC heater and θ_E^T can be acquired. When the laser is at non-zero power, then θ_E can be acquired. θ_E^L can then be calculated accordingly by Eq. (4.2).

4.5 Result and Discussion

The ECS temperature increase (θ_E) is plotted versus the TFC power (P_T) in Fig. 4.4 for different fixed values of the laser power (P_L), where the laser power was set to 0 mW and 75 to 400 mW. The corresponding value of the disk temperature (T_D) is indicated at the end of each curve. The curve with the dashed line corresponds to laser power $P_L = 0\,\text{mW}$, representing the TFC-heating-induced ECS temperature increase ($\theta_E^T(P_T)$), which is called the TFC-heating curve. The other curves represent the total ECS temperature increases ($\theta_E(T_D, P_T)$), which are called back-heating curves. In Fig. 4.4, each curve has a start and an end. The curve starts when the head is at the passive flying status or initial state. It is marked by 'o', at which point $P_T = 0\,\text{mW}$. The curve ends when head-disk contact occurs. The corresponding TFC power is the TDP. This is marked by 'x'. It can be seen that TDP decreases as the disk temperature increases. This is because the laser heating causes a local thermal bump on the disk at the position of the slider. The disk bump acts similarly to the TFC-induced slider protrusion to reduce the fly height, which lowers the initial passive FH, resulting in the decrease of TDP.

θ_E^L can be calculated according to Eq. (4.2), by subtracting the TFC-heating curve from the back-heating curves. Also, the back-off method [56] is used to calculate FH. FH = 0 nm

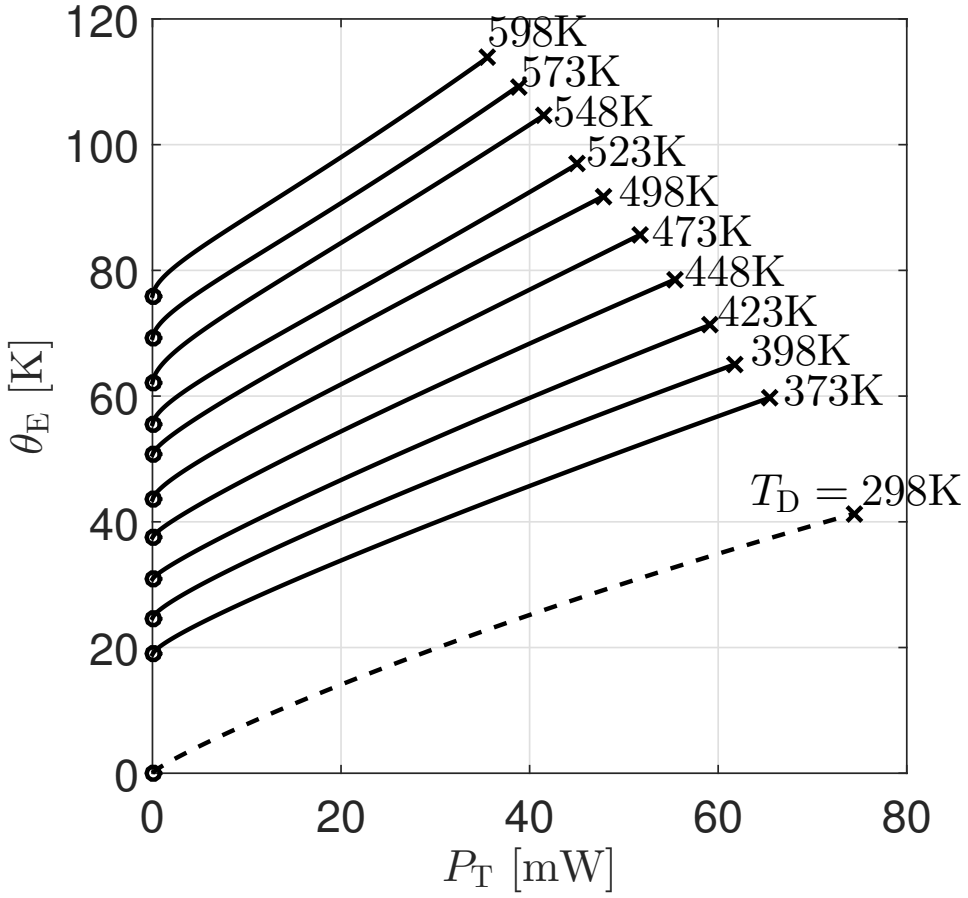

Figure 4.4: The total ECS temperature increase as a function of the TFC power at fixed laser powers. Each curve represents a certain laser power or equivalently disk temperature as indicated at the end of each curve.

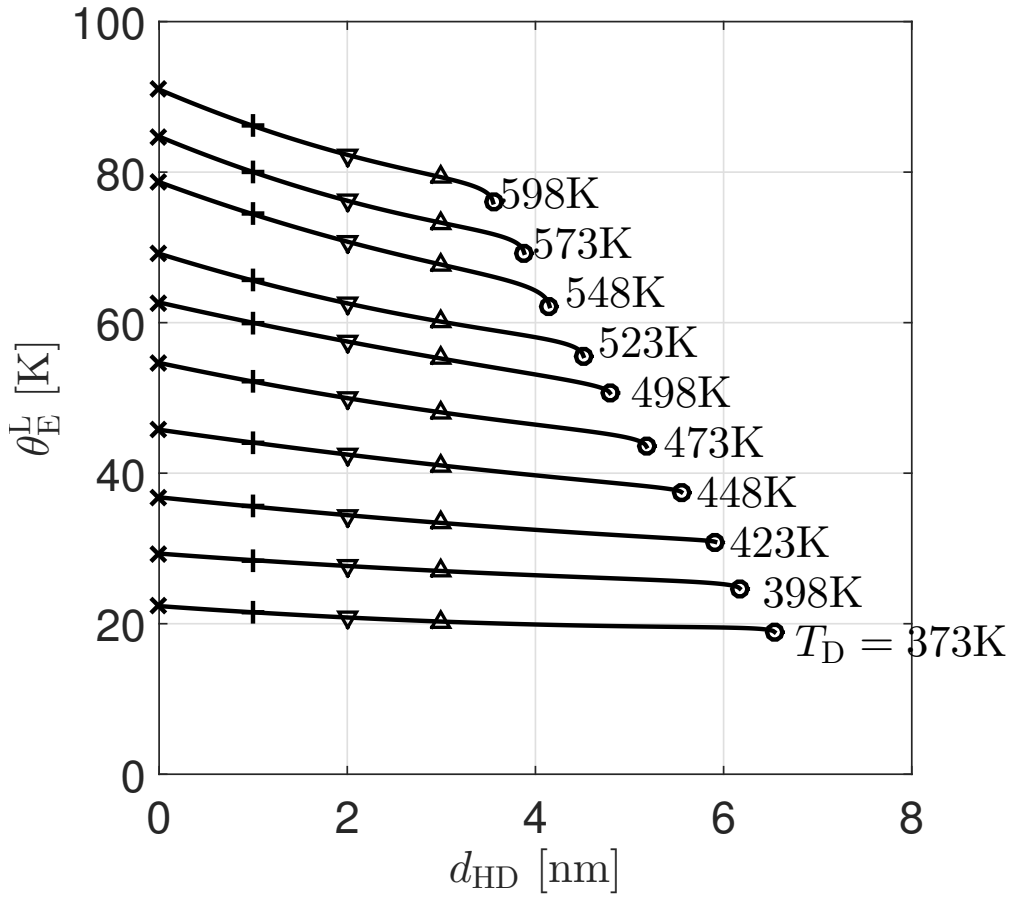

Figure 4.5: The laser-heating-induced ECS temperature increase as a function of the TFC power at fixed laser powers. Each curve represents a certain laser power or equivalently disk temperature as indicated at the end of each curve. These curves are the results of subtraction from Fig. 4.4. d_{HD} means the FH.

when the TDP is reached and increases by 0.1 nm per 1 mW decrease of the TFC power. Fig. 4.5 shows the results of the data processing. Notice that θ_E^L is plotted in reverse order, being shown as a function of FH, at each fixed value of disk temperature.

In Fig. 4.6, several points of each curve are extracted from Fig. 4.5 and plotted with respect to disk temperature increase θ_D. These points include the contact points and points with FH =1 nm, 2 nm and 3 nm. It is clear that the θ_E^L values at these three states are proportional to θ_D.

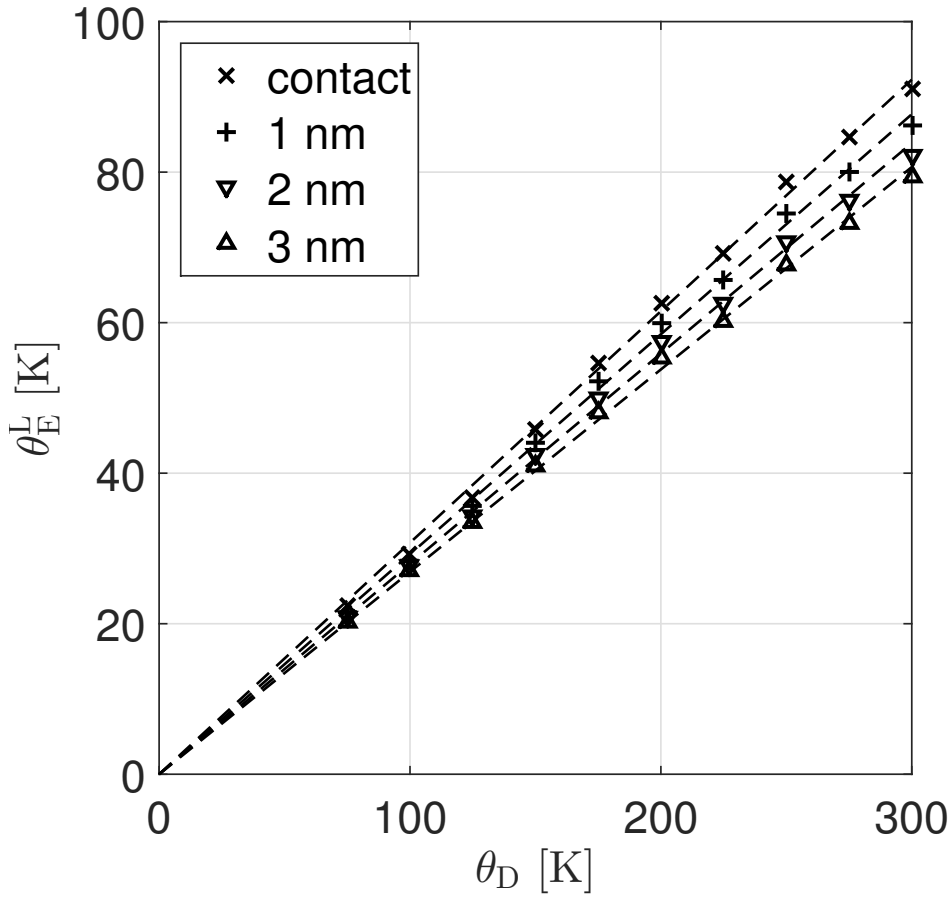

Figure 4.6: The laser-heating-induced ECS temperature increase as a function of the disk temperature. Each curve represents a certain FH.

The head-disk temperature rise ratio (η) is defined as

$$\eta = \frac{\theta_E^L}{\theta_D}. \tag{4.3}$$

Therefore, with linear regressions, η_0, η_1, η_2 and η_3 are 0.308, 0.292, 0.280 and 0.269 respectively, where η_x stands for η with FH = x nm. The reason of $\eta_0 > \eta_1 > \eta_2 > \eta_3$ is because a smaller gap between the head and the disk produces a larger heat transfer coefficient, causing more heat to be transferred from the disk back to the head.

The disk temperature in the experiment was restricted to the range of 298 to 553 K. However, the operating temperature in a HAMR system is $\sim$ 750 K. Since there is no explicit non-linear effect in the system, linearity can be assumed for extrapolation based on Eq. (4.3).

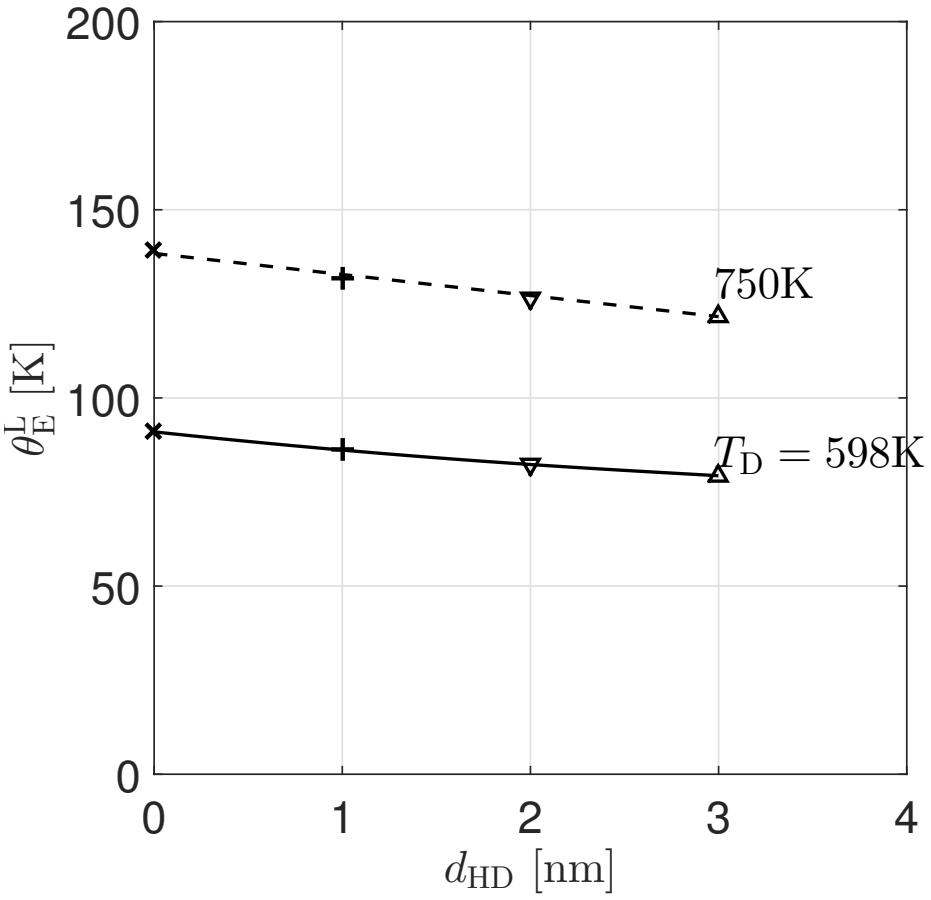

Figure 4.7: The prediction of the ECS temperature when the disk reaches Curie Temperature. d_{HD} means the FH.

If $\theta_D = 452\,\mathrm{K}$ is substituted into to Eq. (4.3), we can conclude that if the free space laser were to heat the disk to its Curie Temperature, the corresponding temperature rise on the ECS would be 139 K, 132 K, 127 K and 122 K when FH = 0 nm, 1 nm, 2 nm and 3 nm respectively, as shown in Fig. 4.7 as the dash line. This is considered a high back-heating temperature [72]. Clearly the temperature increase is a function of the gap distance between the head and the disk. This implies that the heat transfer is a strong function of the gap. Recent results in thermal modeling in references [56, 61, 60, 59] show such a dependence. More modeling still needs to be done for the head-disk interface to get a better prediction of NFT back-heating, but this experiment indicates that back-heating is significant for nanoscale gaps when the disk is at the Curie Temperature in HAMR systems.

4.6 Summary

In this chapter, a nanoscale heat transfer experiment is reported based on the current HDD design. The key to the study relies on the gap between the head and the disk being in the scale of 1 to 10 nm. The study shows that the temperature increase of the heated slider surface is a linear function the temperature rise of the heated disk surface. It also shows that the protrusion on the disk significantly decreases the passive flying height. This study is an indicator of the strength of the heat transfer in a nanoscale gap.

Chapter 5

Investigation of the ECS self heating

5.1 Introduction

In Chapter 4, a recording head with an ECS and a TFC heater, a free space laser and a one-sided disk were used to perform the back-heating experiment. The ECS resistance was measured and converted to the temperature rise based on the calibration as described in Section 4.3. Since the ECS is very sensitive to electrostatic charge, R_E is usually measured by a voltmeter-ammeter method, where a constant current bias (I_E) is applied through the ECS, the voltage of the ECS (V_E) is measured and the resistance R_E is calculated using Ohm's law,

$$R_E = V_E / I_E \tag{5.1}$$

Then the temperature increase of the ECS ($\theta_E = T_E - T_0$) is calculated based on Eq. (2.2). However, since the ECS is also a resistor, applying a bias current through it causes an additional Joule heating, which is sensed by the ECS itself. This is called the ECS self heating. The ECS self heating was neglected in Chapter 4, since the bias current was very low in that case. However, if the bias current is purposely set high, then the ECS becomes a heat source. In this way, even when the disk is not heated by the laser, the temperature difference between the two surfaces is created, and the nanoscale heat transfer can be investigated.

In this chapter, the ECS self heating effect is investigated experimentally [73, 74]. Similar to Chapter 4, the recording head with an ECS and a TFC heater flies on a rotating disk. However, here no free space laser is involved. The TFC heater is used to control the gap's distance and the ECS is used to sense the temperature on the head. Different ECS current biases were used to create the ECS heating scenario. This experiment can help understand the heat transfer dependence on the head-disk spacing.

The rest of this chapter is organized as follows. Section 5.2 discusses the basic principle of the system. Section 5.3 discusses the ECS self-heating effect when it is the sole heat source. Section 5.4 introduces the ECS-TFC heating experiment. A comparison between this experiment and another static experiment is also discussed. The chapter is summarized in Section 5.5.

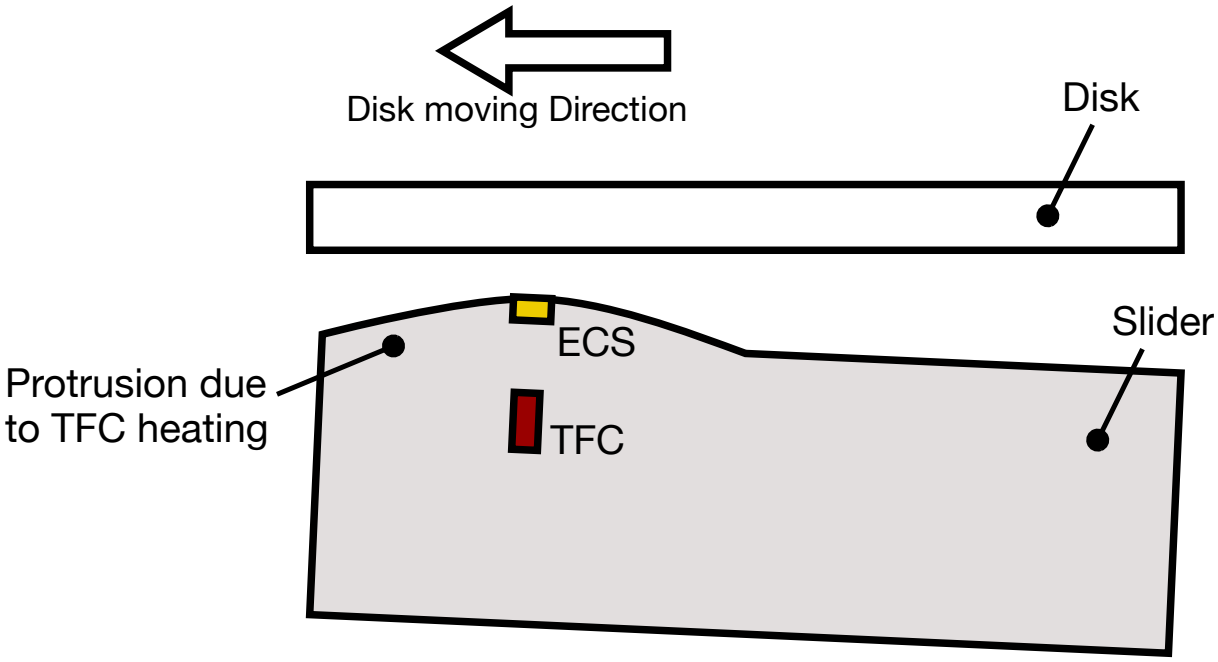

Figure 5.1: A schematic diagram of the TFC heater and the ECS in the slider. The heater is embedded inside the slider while the ECS is on the surface of the slider. Powering on the TFC heater leads to the protrusion of the slider, lowers the fly height. It also heats the local region. Schematic not to scale.

5.2 System Setup

The CML-HAMR stage was used for the experiment. The disks were of the 2.5-inch format with glass substrate. The head with the TFC heater and the ECS was flying on the disk. The AE sensor was used for head-disk contact detection.

Since no laser was involved, the only two heat sources were the TFC heater and the ECS. As a result, θ_E is a combination of the TFC heating and the ECS self heating. Since there are no explicit nonlinear factors, this is expressed as:

$$\theta_E = \theta_E^E + \theta_E^T \tag{5.2}$$

where θ_E^E is the ECS temperature increase due to ECS self heating and θ_E^T is the ECS temperature increase due to TFC heating. A schematic of the heating effect is shown in Fig. 5.1. It is important to separate the two heat sources. Therefore, two series of experiments were designed, the ECS self heating experiment and the ECS-TFC combined heating experiment.

5.3 ECS Self-heating Experiment

When the TFC power (P_T) is set to zero, the head flies on the disk passively. In this case, the ECS is only self heated, and $\theta_E = \theta_E^E$. Therefore, by changing I_E and measuring θ_E, the temperature increase of the ECS due to ECS self heating can be obtained. In the experiment, I_E was selected as 0.5 mA, 1 mA, 1.5 mA and 2 mA. The corresponding R_E was measured and converted to θ_E according to Eq. (2.2). Then the electric power supplied to the ECS (P_E) was calculated based on Joule's Law,

$$P_E = I_E^2 R_E. \tag{5.3}$$

The relation between θ_E and P_E when the head flies passively is shown in Fig. 5.2. It can be seen that θ_E is a linear function of P_E. This is because in the passive-fly state, there is no TFC heating, i.e., the ECS is the only heat source. This leads to a simple linear heat transfer problem in which the temperature field is linear with the power density of the sole heat source. The slope of the curve is defined as the ECS self heating rate with the value 200.2 K/mW. This agrees with published simulation results [42]. It can also be seen that $\theta_E = 4.6$ K when $I_E = 0.5$ mA (or $P_E = 0.028$ mW) but $\theta_E = 124.8$ K when $I_E = 2$ mA (or $P_E = 0.637$ mW). This means that if I_E is sufficiently low θ_E^E is minimal and can be neglected, while that is not the case if I_E is too high. It is also to be noticed that the experiment was done for various disk rotation speeds (ω): 3000 RPM, 4000 RPM and 5000 RPM. Each data point shown in Fig. 5.2 consists of three points taken at the three different speeds. This means that ω has no effect on R_E and θ_E when the head is passively flying. This is because when the head is far enough away (FH $>$ 2 nm) from the disk, the heat transfer change across the HDI is so small that it does not affect θ_E.

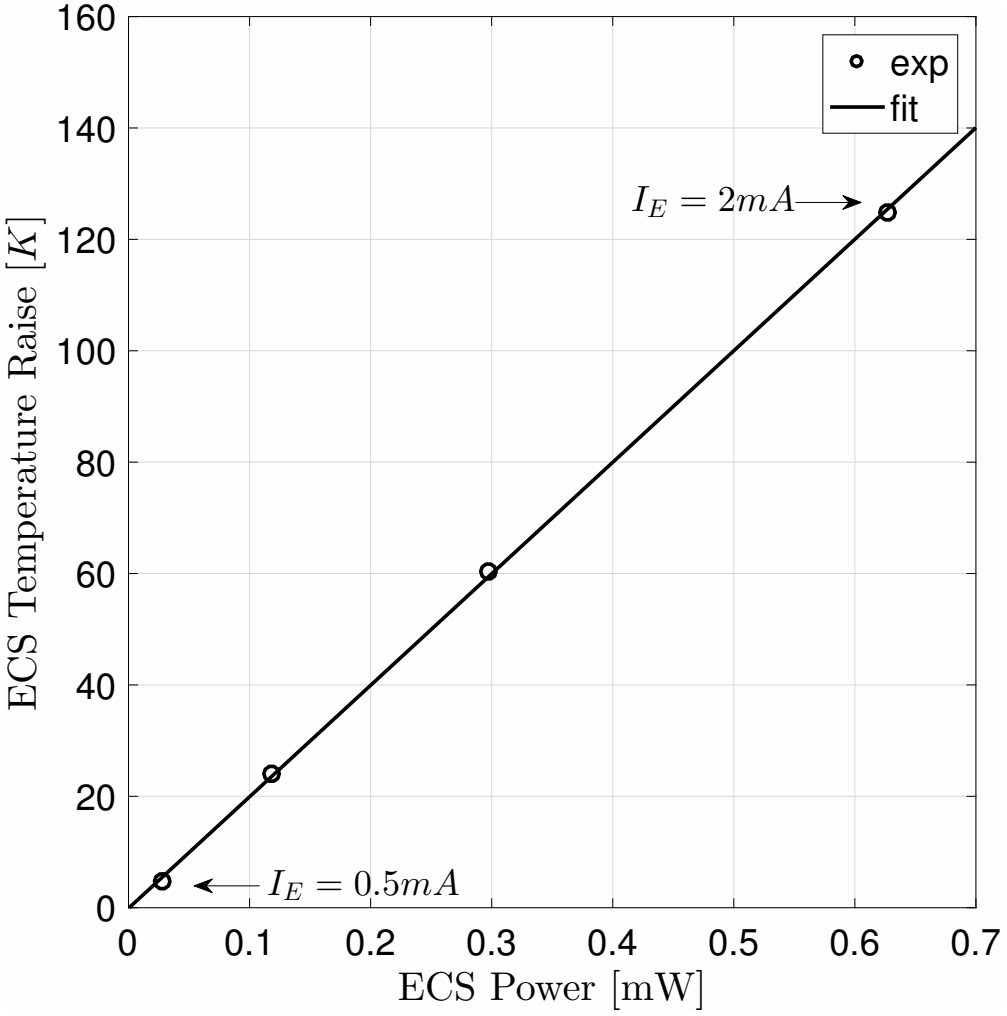

Figure 5.2: The dependence of the ECS temperature on the ECS power. The figure shows that the relation is linear.

5.4 ECS-TFC Heating Experiment

In the ECS self-heating experiment, the ECS is the sole heat source and θ_E^E can be measured. In the ECS-TFC heating experiment, the TFC heater is turned on as the second heat source. After the ECS self-heating experiment was completed, the TFC heater was powered on to adjust the FH. When the head was flying on the disk, P_T was increased from 0 mW in steps of 0.25 mW. The increase of P_T caused the decrease of the FH, in which 1 mW increase of P_T caused about 0.1 nm decrease of FH. This relation between P_T and FH is essentially linear down to a proximity condition where there is some strong increase in the heat transfer between the slider and the disk [39, 56]. Head-disk contact happened when FH = 0, which was detected by the AE sensor. Then P_T was reset to zero. As in the ECS self-heating experiment, three rotation speeds were used here also: 3000 RPM, 4000 RPM and 5000 RPM. Different values of I_E were applied to the ECS, and R_E was obtained and converted to θ_E. Also, the values of I_E were selected from 0.5 mA, 1 mA, 1.5 mA and 2 mA.

Fig. 5.3 shows the experimental results. Figs. 5.3(a)(b)(c) show the AE sensor signal versus TFC power, P_T, for ω of 5000 RPM, 4000 RPM and 3000 RPM, respectively. Each plot consists of four curves, representing experiments with $I_E = 0.5$ mA, 1 mA, 1.5 mA and 2 mA. It can be seen from the figures that the AE signal remains constant initially as P_T increases. In this regime, the slider is actively flying on the disk without making contact. Then at a certain power, the AE signal suddenly rises. This is when the slider starts to make contact with the highest asperities of the disk. As P_T continues to increase, the contact becomes more intense, and the mode shape of the slider's vibration may also change [70]. Then the AE signal reaches a peak value before it starts to decrease. This peak is defined here as the contact point where FH = 0. It can also be seen that when ω is fixed, the AE signal curves at different I_E have similar shapes. This means that the thermal deformation caused by the ECS heating is minimal and does not affect the slider's fly-height [75, 42].

Figs. 5.3(d)(e)(f) show the total ECS temperature increase, θ_E, vs P_T. The organization of the figures is the same as those for the AE signal. The vertical dashed lines in each figure represent the power for the contact point. It can be seen from the figures that the curves start from $P_T = 0$ and the values of θ_E at the starting points are approximately equal to the values in Fig. 5.2. At these points, there is only ECS self heating. As P_T increases, the ECS temperatures increase as a result of increasing TFC heating. The curves end when head-disk contact occurs. From the curves with $I_E = 0.5$ mA, it can be seen that the portion due to the ECS self heating is small compared with TFC heating. As a result, the ECS self heating effect is usually neglected when I_E is low [41]. And so these curves can be considered as a result of TFC heating only, called TFC heating curves. However, the ECS heating effect cannot be neglected when $I_E \geq 1$ mA. It can be seen that when $I_E \geq 1$ mA, the ECS self heating is at least 50% of θ_E. Therefore, θ_E is influenced by both TFC heating and ECS self heating. These curves are called ECS-TFC heating curves. It can also be seen that the curves in each plot are almost parallel to each other. However, the curves differ when the head and the disk are close to the contact point. When $I_E = 0.5$ mA, the curve tends to rise with P_T near the contact point; but when $I_E \geq 1$ mA, the curves tend to drop near the

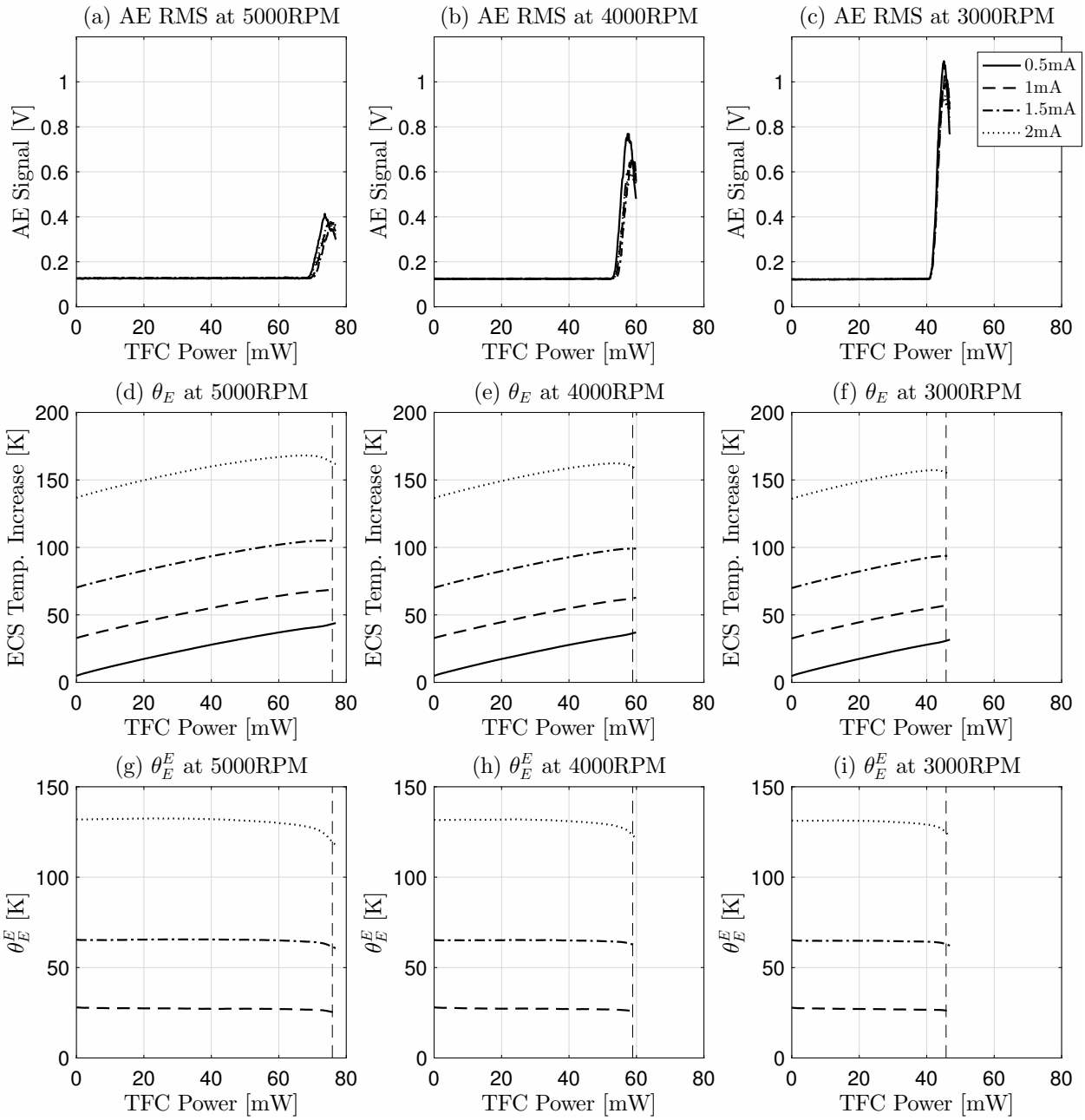

Figure 5.3: (a), (b) and (c) show the AE sensor signal versus the TFC power at different ECS currents and disk rotating speeds. The ECS temperature increases as the TFC power increases at different ECS currents and disk rotating speeds. (d), (e) and (f) show the temperature increase of the ECS versus the TFC power of the corresponding experiments. (g), (h) and (i) show the temperature increase of the ECS due to the self ECS heating effect. 10 mW of TFC power increase is equivalent to about 1 nm decrease of head-disk spacing. The legend is the same for all figures, as shown in the upper right corner.

contact point.

In order to study the effect of ECS heating, the TFC heating only curves (curves with $I_E = 0.5\,\text{mA}$) are subtracted from the ECS-TFC heating curves (curves with $I_E \geq 1\,\text{mA}$), according to Eq. (5.2). The result of the subtraction is the ECS temperature increase due to ECS heating, θ_E^E, as shown in Figs. 5.3(g)(h)(i). In these figures, only θ_E^E with $I_E \geq 1\,\text{mA}$ are left. It can be seen that θ_E^E remains constant initially as P_T increases. However, θ_E^E starts to decrease when the head-disk spacing is within 1 nm. This means that when FH $> 1\,\text{nm}$, there is not much change in the total heat transfer between the ECS and disk. This agrees with the passive-fly experiment. However, when FH $< 1\,\text{nm}$, the heat transfer is much more significant.

If ω and I_E are fixed, the heat generated by the ECS and transformed to the disk due to its rotation remains unchanged. As a result, the heat flow across the HDI can be assumed to be constant and the FH is the only factor that is changed. Therefore, the change in θ_E^E indicates the change of the heat transfer across the HDI. To exclude the effect of different ECS power, we normalize θ_E^E by

$$\hat{\theta}_E^E = \frac{\theta_E^E}{\theta_{E0}^E}, \tag{5.4}$$

where θ_{E0}^E is θ_E^E at the point $P_T = 0$. Fig. 5.4 shows the average $\hat{\theta}_E^E$ for different bias with respect to FH, where FH is obtained from P_T by the known relationship between them. It can be seen from the figure that as the slider approaches the disk, $\hat{\theta}_E^E$ decreases slowly initially. When FH $< 1\,\text{nm}$, $\hat{\theta}_E^E$ starts to decrease rapidly. The decrease of $\hat{\theta}_E^E$ is an indication that the heat transfer across HDI becomes stronger. This is a clear indication that the model for calculating heat transfer across the gap should predict a strong dependence on the width of the gap, especially when FH $< 1\,\text{nm}$. As $\hat{\theta}_E^E$ decreases more, the correlation between the heat transfer and the gap becomes stronger.

Recent results of thermal modeling in Refs [61, 60, 59] show such a strong dependence. It is also noticed that the rate of decrease is different at different ω. $\hat{\theta}_E^E$ decreases more with lower FH as ω is higher. This is because when the disk rotation speed is higher, more heat dissipates from the rotating disk, resulting in cooler head temperature.

Although the experiment was done using PMR heads and disks, the heat transfer mechanism across the HDI remains the same whether the setup uses PMR or HAMR heads and disks. Therefore, the results obtained in the experiment can be directly used to check different heat transfer models for HAMR.

It is interesting to compare the results obtained here on rotating disks and flying heads with the experiment reported in Ref. [76]. There, a slider sat on a stationary disk. The position of the slider was adjusted such that the initial distance between the ECS (called TS in that reference) and the disk was ~10 to 12 nm. Then the TFC heater (called TA in that reference) was powered on and the temperature of the ECS was measured. The experiment showed that the ECS temperature first increased and then dropped sharply as the TFC power increased. The drop is much steeper there than the result shown in Fig. 5.4. The initial impression might be that the result of this paper and the reference are contradictory.

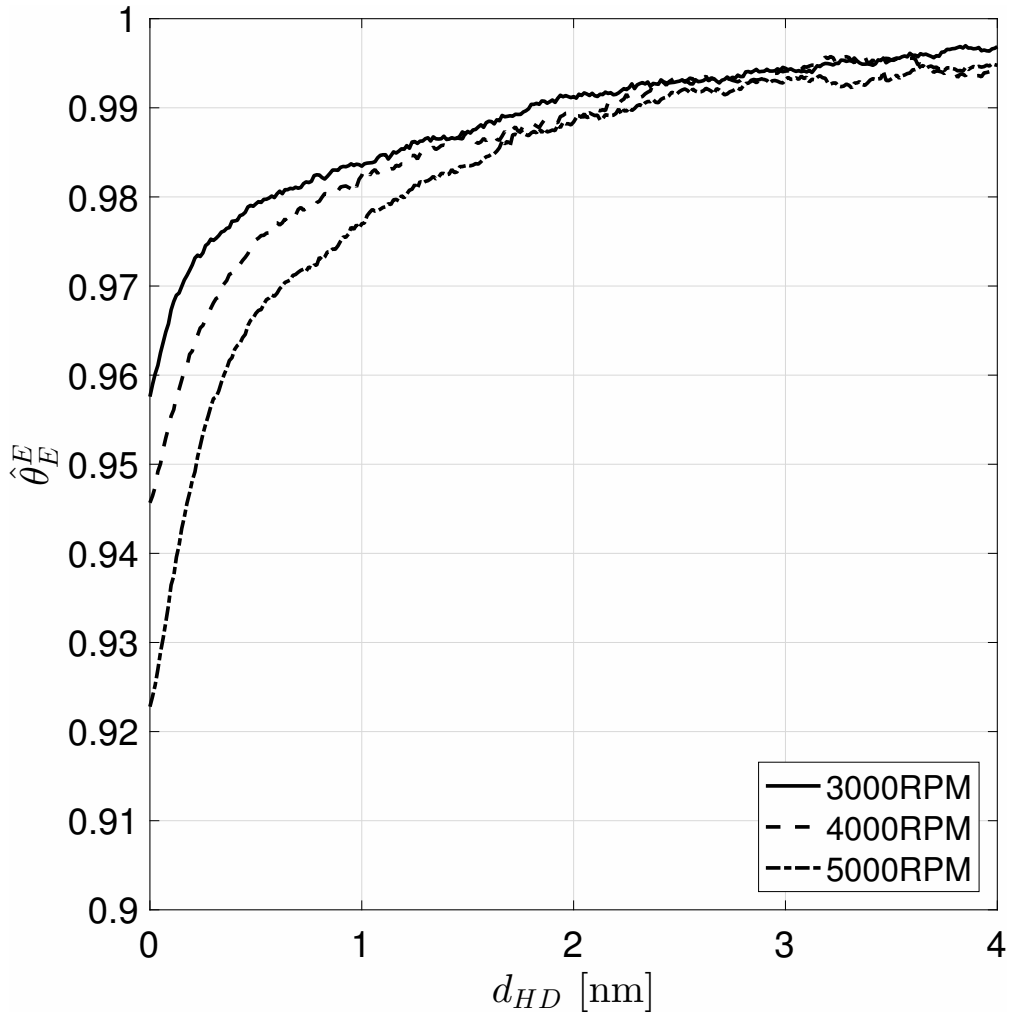

Figure 5.4: The average normalized ECS temperature increase due to self heating versus the head-disk spacing at different disk rotation speeds. d_{HD} is the FH.

However, it should be noted that the two experiments are under quite different scenarios. A detailed comparison of the two experiments is shown in Table 5.1. In our experiment, the head and the disk were in relative motion. Therefore the heat transfer coefficient when the TFC power is zero is much larger than that in Ref. [76], in which the head and the disk were stationary relatively. As a result, when the slider approaches the disk, the heat transfer across the HDI increases by $\sim$ 1000 times in Ref. [76]. However, in our case, the heat transfer only increases by $\sim$ 10 times. That is the reason why the ECS temperature drops steeper in the reference compared with our experiment.

	This paper	Ref. [76]
Experimental Setup	Slider flies on rotating disk	Slider sits on stationary disk
Convection Models	Air bearing cooling	Free air convection
Radiation and Conduction Models	Models from Refs. [59, 60, 61]	
Convective coefficient [77] [W/(m^2 K)]	$\sim 10^6$	< 100
Conductive and Radiative coefficient [78] [W/(m^2 K)]	$\sim 10^3$ (FH = 10 nm), $\sim 10^6$ (FH = 0.5 nm)	
Total coefficient at FH = 10 nm [W/(m^2 K)]	$\sim 10^6$	$\sim 10^3$
Total coefficient at FH = 0.5 nm [W/(m^2 K)]	$\sim 10^6$	$\sim 10^6$
Total coefficient increase from FH = 10 nm to 0.5 nm	< 10	$\sim 10^3$

Table 5.1: The comparison between experiment in this paper and in Ref. [76].

5.5 Summary

In this chapter, the ECS self-heating experiment and the ECS-TFC heating experiment were performed to understand the heat transfer change with head-disk spacing change. The study shows that the ECS has a strong self heating effect when it is used with high current bias, and the heating effect is linear with the power of the ECS. It is also shown that the ECS temperature increase due to the self heating decreases with the head-disk spacing. This study indicates that the heat transfer across the HDI is a strong function of the head-disk spacing. The difference between this and a prior experiment is also discussed.

Chapter 6

Head Disk Interaction in HAMR

6.1 Introduction

In HAMR, the magnetic material on the disk is heated to near its Curie temperature (∼450 °C) momentarily (∼10 ns) by the LPDS. As discussed in Section 2.3, the coupling efficiency of the LPDS is ∼ 5%, even neglecting manufacturing tolerances. This means that the majority of the laser power remains in the head and converts to heat. This can cause unwanted thermal expansion in the head and FH change, the effect of which is similar to the mechanism of the TFC heating. Additionally, since the media is at a very high temperature and the COC and lubricant layers are adjacent to the magnetic layer, material transfer from disk to slider and thermal degradation unavoidably happens. It is been reported that solid contamination appears at the location of the NFT after the head flies on the disk for a short while with laser heating [35, 36]. This contamination can block the optical path from the head to the media, which further reduces the coupling efficiency. It also causes problems such as overheating of the NFT and insufficient heating of the media. Therefore, it is important to understand the mechanism of the contamination formation and the severeness of the thermal expansion of the head caused by the laser heating.

The waveguide heads were provided to CML by the HDD industry for the experiments. The waveguide head does not have the NFTs attached to the end of the waveguide. The size of the laser beam coming out of the waveguide is ∼500 nm. It is noted that since there is no NFT, more EM waves can pass through the HDI and reach the media. It is estimated that 10% of the total laser power can reach the outlet of the waveguide head [79]. But similar to the NFT case, the majority of the power still stays in the head.

Three different experiments were designed to study the head's performance due to the laser heating. In Section 6.2, the head's thermal protrusion caused by the laser heating is investigated. The head's dynamic change caused by the laser heating is reported in Section 6.3. In Section 6.4, the accumulation of solid contamination on the head is studied. Section 6.5 concludes the chapter.

6.2 Head Protrusion due to Laser Heating

The waveguide head's thermal protrusion caused by the laser heating was investigated on the CML-HAMR stage using a PMR disk. This disk was of the 2.5-inch format with glass substrate. The head has the LD, the waveguide and the TFC heater. The disk rotating speed was set to 5400 RPM. The AE sensor was used for head-disk contact detection.

In order to quantify the head's protrusion due to the laser heating, the TFC TD experiments with different laser currents were performed, similar to what is described in Sections 4.4 and 5.4. For each TD process, the laser current is kept at a constant value. When the head was flying on the disk, the TFC power increased from 0 mW in steps of 0.25 mW. The increase of the TFC power for every 1 mW causes a decrease of the FH of 0.1 nm. This relation between the TFC power and the FH is essentially linear down to a proximity condition where there is some strong increase in the heat transfer between the slider and the disk [39, 56]. Head-disk contact occurs when the FH reaches zero, which was detected by the AE sensor. Then the TFC power was reset to zero. The AE root-mean-squared (RMS) signal was recorded during the process. The TFC TD processes were repeated for different laser currents. A head cleaning process, i.e., flying the head in proximity to the disk for a short time [80], was performed between each two TFC TD experiments to ensure any potential accumulation on the head was removed. The laser current was set to zero for the first process and increased for the following processes until it reached the maximum current, 59 mA. Additionally, between any two laser-on tests, one process with the laser off is performed. This was to ensure that the head's dynamics did not change during the experiment.

Fig. 6.1 shows the AE RMS signal vs. the TFC power for different laser currents. Fig. 6.1(a) shows the laser-on TD processes, while Fig. 6.1(b) shows the laser-off processes as references. Fig. 6.2 is a zoomed-in view of Fig. 6.1. In Figs. 6.1(a) and 6.2(a), it can be seen that the AE RMS signal remains almost constant as the TFC power increases initially. However, it suddenly increases at a certain TFC power, indicating a head-disk contact. The TFC power at this point is the TDP. It can be seen that when the laser current is zero, the TDP is 159 mW, which is the maximum TDP for all the laser current settings. As the laser current increases from zero to 59 mA, the TDP decreases. This is because the laser heating causes additional thermal expansion, i.e., the slider thermal expansion is caused by both TFC heating and laser heating. As a result, the TDP decreases as the laser current increases. In Figs. 6.1(b) and 6.2(b), it can be seen that all curves overlap each other. It indicates that the head's dynamics did not change throughout the entire experiment.

The TDP change caused by the laser heating is calculated by subtracting the laser-on TDP from the reference TDP. The relation between the TDP change and the laser current is shown in Fig. 6.3. A series of five experiments was performed. It is seen from the figure that the TDP change is almost linear with the laser current. When the laser current is at 59 mA, the TDP change is 19 mW. It can be calculated that the TDP-change-laser-current-ratio is 0.3 mW/mA using the linear regression with zero intercept.

During HAMR operation, it is important to take the laser-induced protrusion into consideration when the TFC heater is active. Since the laser heating causes the additional

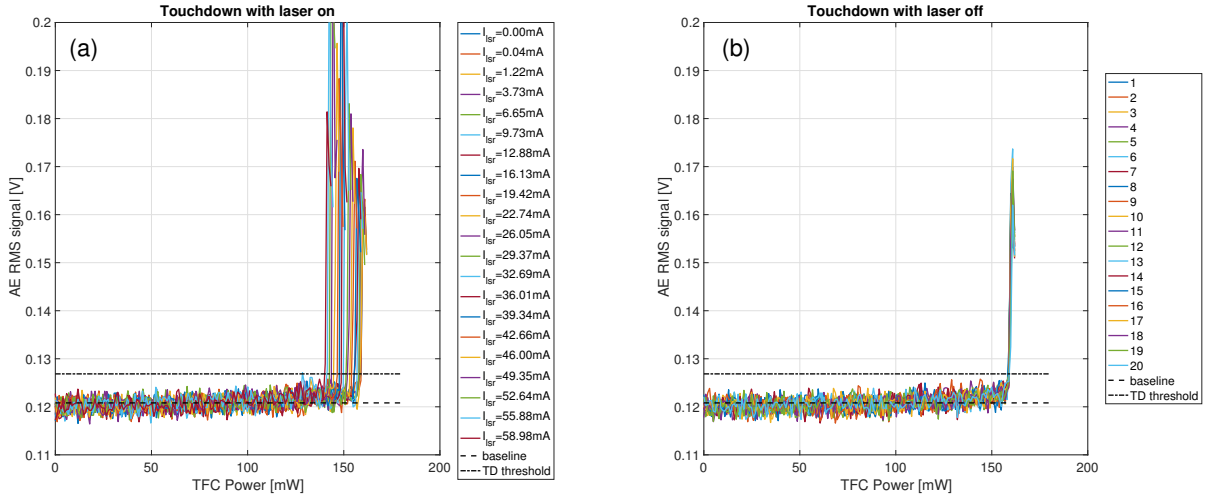

Figure 6.1: The AE RMS signal vs. the TFC power at different laser currents. (a) shows the cases where the laser is on and the laser current ranges from 0 mA to 59 mA. (b) shows the reference cases where the laser is off to ensure repeatability.

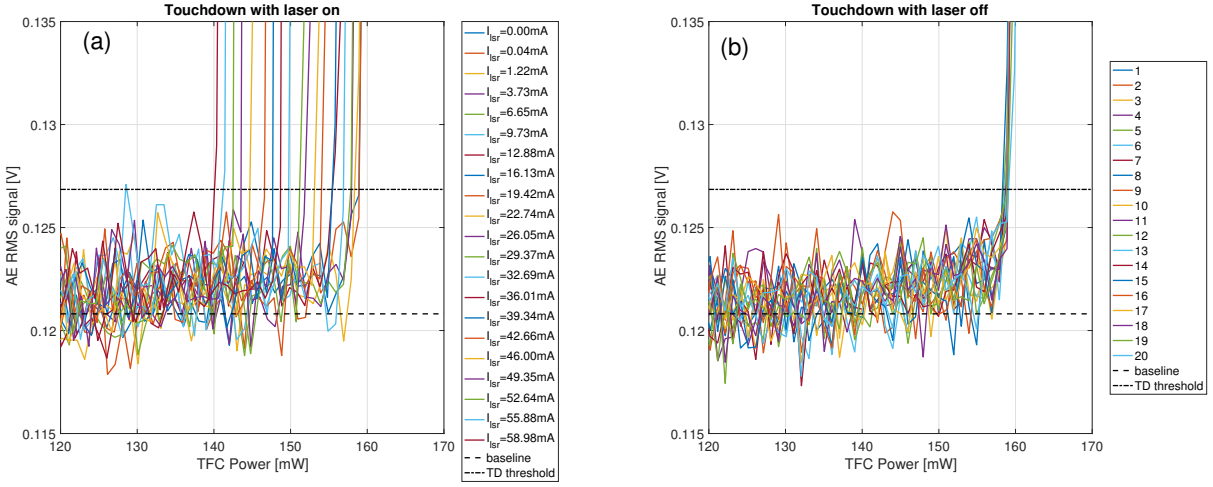

Figure 6.2: The zoomed-in version of Figs. 6.1 (a)(b)

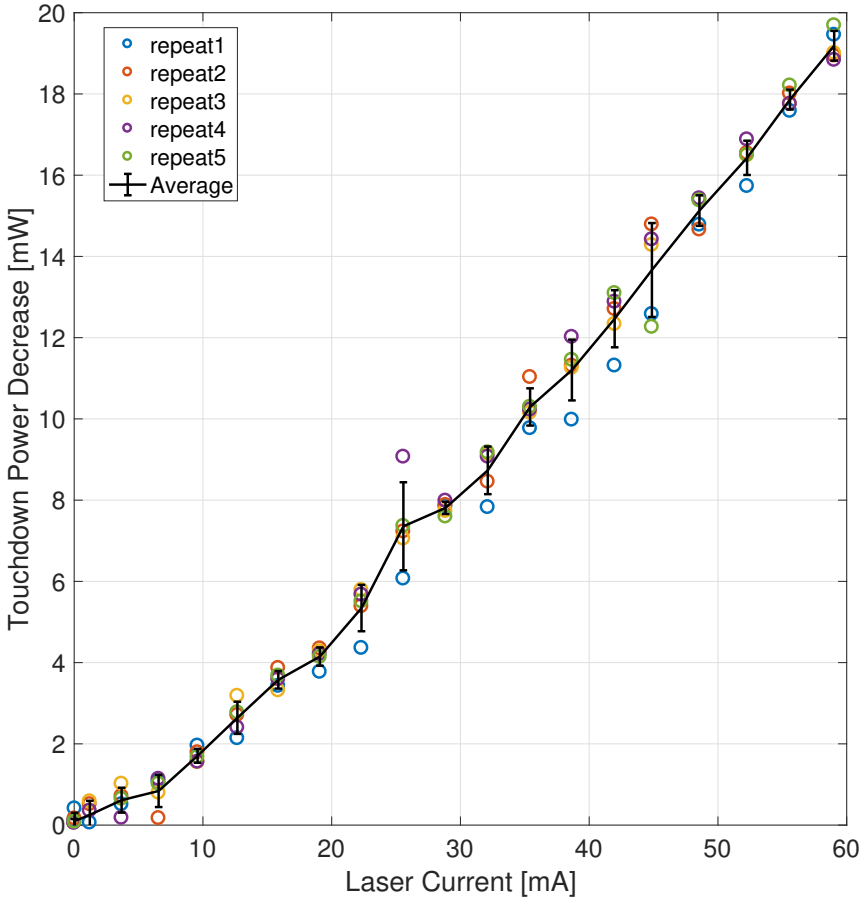

Figure 6.3: The TDP change due to the laser heating.

protrusion, the TFC power needs to be reduced accordingly in order to achieve the desired FH and avoid undesirable head-disk contact.

6.3 The Accumulation of Contamination on the Head

It is been reported that solid contamination appears at the location of the NFT after the head flies on the disk for a while with laser heating [35, 36]. However, the rate at which the contamination forms and how it changes the dynamics of the head is still unreported. By monitoring the AE raw signal change during the heating of the waveguide head, the slow change of the head dynamics can be studied.

In the first part of the experiment, the head flies on the disk at zero TFC power and a constant laser current for a certain amount of time. This is called a FH process. After

the FH process, three repeats of the TFC TD processes were performed in order to clean the head's contamination during which the AE RMS signal was recorded. Different laser currents and laser-on durations were selected during different runs.

Fig. 6.4 shows the AE RMS signal vs the TFC power during the contamination and clean up stages. Different subfigures indicate different constant laser heating processes with different laser currents and laser-on durations, which are indicated on the titles of the subplots. Fig. 6.4(a) shows the TD before any laser heating. The AE RMS curve is normal: it remains almost constant before the TD and the value suddenly rises when the TD happens. However, in Figs. 6.4(b)-(h), it can be seen that the first TFC TD process is abnormal. Before the TDs, the AE RMS curves all have bulge shapes. This indicates that head-disk interaction occurs before TD happens, due to the head's contamination. The second and the third TFC TD processes are normal. This means the contamination is cleaned off with one TD process. It can also be seen that the bulge shape in Fig. 6.4(d) is minimal, which is the case of laser current of 49 mA and the duration of 100 ms. However, Figs. 6.4(e)(f)(g), which have the same laser current but much longer heating duration, show much larger bulge shapes. This means that more contamination forms on the head with longer times of laser heating, causing stronger head-disk interaction. By comparing Fig. 6.4(b) and Fig. 6.4(g), it can be seen that with higher laser current, the formation of the contamination is also more severe.

In the second part of the experiment, the head flies on the disk passively. The laser is turned on for 30 s every 20 min. The laser current is set at 58 mA. The 30 s laser-on period is also a constant laser heating process, during which the AE raw signal is monitored at the sampling rate of 1 MS/s. The TFC TD process is performed between two constant laser heating processes to ensure the head's accumulation is removed. The entire experiment runs for 16 h. The AE raw signal change during the entire experiment is analyzed to study the long-term change of the head dynamics.

Fig. 6.5 shows the AE raw signal during the constant laser heating processes at 0 h, 6 h, 12 h and 16 h. It can be seen that at 0 h, the AE raw signal remains almost constant over the 30 s-laser-on period. This indicates that the system dynamics does not change during this time. However, starting at 6 h, it can be seen that the magnitude of the AE raw signal starts to increase at around 22 s, indicating the dynamics change of the system. This phenomenon continues to show increases at 12 h and 16 h.

This change can be seen more clearly when the AE signal is transformed by the STFT. The STFT has a window size of 30 ms and overlap of 15 ms. The spectrograms of the AE signals are shown in Figs. 6.6. It can be seen in the figures that the resonance of the head is mainly around 100 kHz. This is usually the first pitch mode of the slider. It can also be seen that the magnitude of the resonance at 100 kHz increases during the constant laser heating process at the times 6 h, 12 h and 16 h. This indicates that the interactions between the head and disk increase during this process. This is evidently due to the contamination formed on the head during laser heating. The contamination increases in size as the laser heating continues and finally starts to contact with the disk, causing head-disk interaction. Such an interaction leads to the vibration of the head. The vibration then propagates to

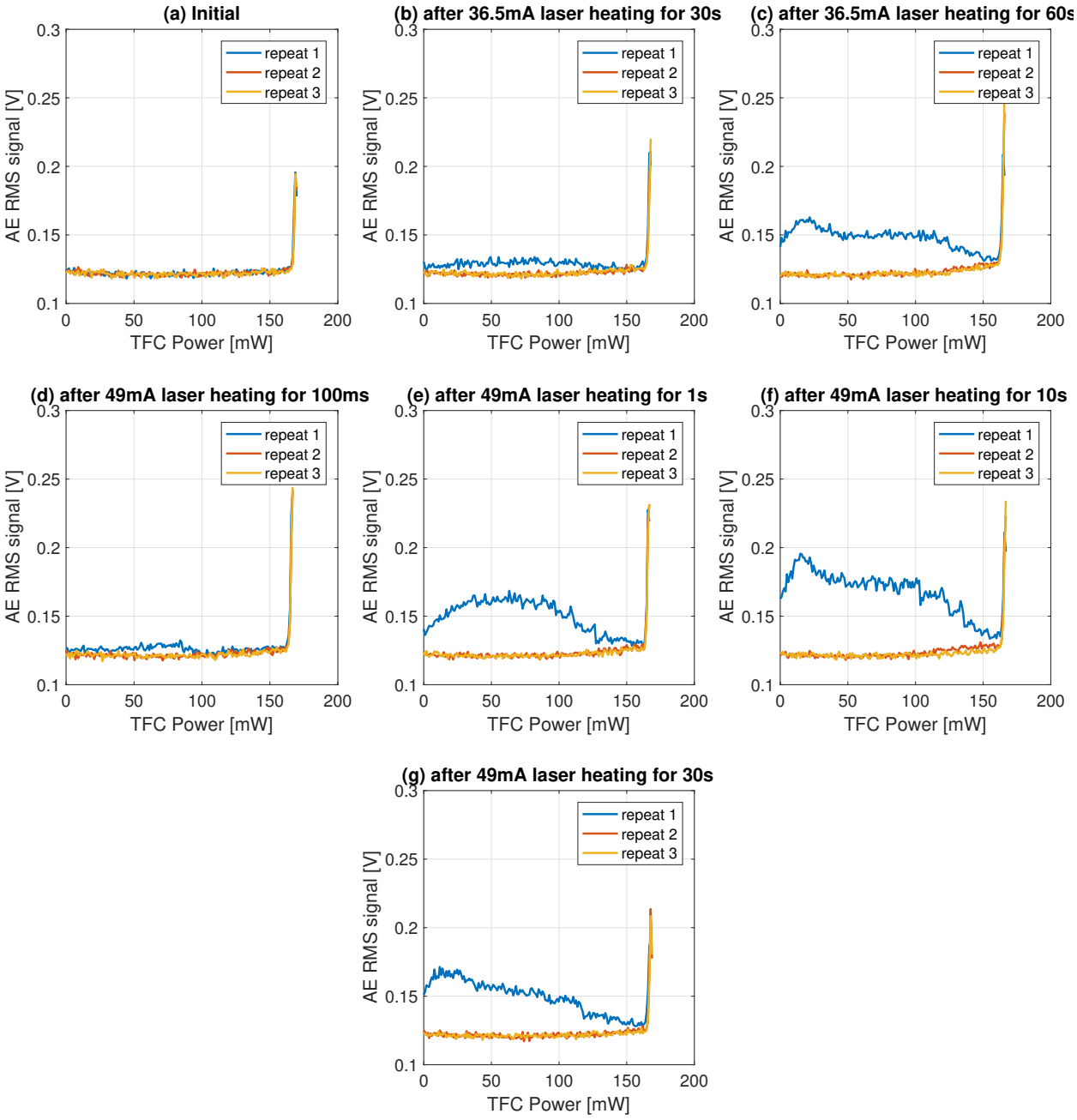

Figure 6.4: The AE RMS signal vs the TFC power during the cleaning processes after the constant laser heating. The constant laser heating conditions in each figure are shown on the figures' titles.

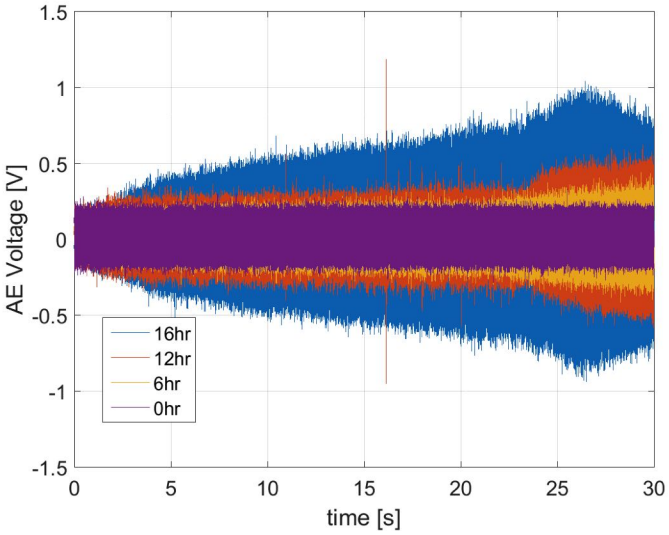

Figure 6.5: The AE raw signal over the 30 s-laser-on period at four different time stamps: 0 h, 6 h, 12 h and 16 h.

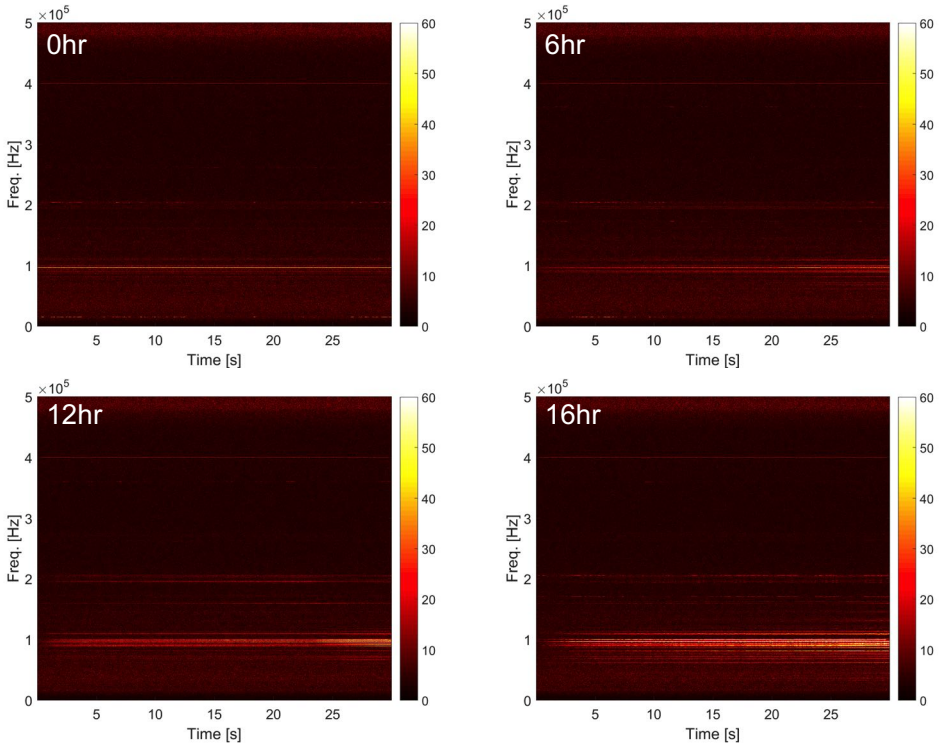

Figure 6.6: The STFT of the AE signal over the 30 s-laser-on period at four different time stamps: 0 h, 6 h, 12 h and 16 h.

the AE sensor, causing AE signal magnification. Also it is seen that in the longer term (from 0 h to 16 h), the magnitude of the resonance at 100 kHz increases. This indicates that the contamination formation rate increases with time. The faster formation results in a larger amount of contamination over the same period of time, causing more severe head-disk interaction.

6.4 Accumulation on the Head during Contact

When the head flies on the disk with zero TFC power, the FH is a few nanometers. It takes a certain amount of time for the contamination to build up on the head and fill the gap, as shown in Section 6.3. However, during the writing process, the TFC heater is usually on such that the writing field from the writer can be efficiently delivered to the media. Since the FH is low, the gap is filled quicker, which can affect the head's behavior more severely. Therefore, it is important to test the case where the head flies in proximity to the disk.

In this part of the experiment, the head remains flying on the disk at zero FH. This is controlled by the TFC heater and the AE sensor. A predetermined touchdown threshold is set on the AE RMS signal. If the detected AE RMS signal is below the threshold, it means that the head and the disk are not in contact yet. Then the TFC power keeps increasing. Once the detected AE RMS signal is above the threshold, the TFC power decreases until the AE RMS signal is below the threshold again. This procedure is repeated. Therefore, the AE RMS signal fluctuates around the threshold line and the head is just in proximity to the disk, and the TFC power is the TDP. While the head maintains zero FH, the laser is turned on and off periodically. The accumulation forms and the head protrudes when the laser is on, so the TDP drops. When the laser is off, the accumulation is cleaned off and the TDP recovers. With this method, the determination of how the TDP changes with the head's flying time can be studied. New heads without previous flying are used in the experiment.

Fig. 6.7 shows the TDPs at different laser currents (0 mA, 20 mA, 35 mA and 49 mA) with respect to time and Fig. 6.8 shows the TDP decrease compared with zero laser current. It can be seen from Fig. 6.7 that the TDPs fluctuate for the first 4 h, then the fluctuation decreases and the TDP is almost constant. Especially for the case at zero laser current, the TDP decreases over time. This can be because the contamination accumulated on the head is not cleaned off well, or the material is left on the disk. Both can cause TDP drop. It can also be seen from Fig. 6.8 that the TDP change tend to decrease over time. This is likely due to the decrease of new contamination formed on the head. It can be seen from both figures that the TDP stabilizes at around 4 h. This could mean that the contamination stops further formation. It is noted that the TDP decrease after the stabilization matches the result in Section 6.2.

The topography of the waveguide area on the slider surface was measured by the AFM before and after the experiment. The measurements are shown in Figs. 6.9, 6.10, 6.11 and 6.12. It is noted that the same head was measured before and after flying. This head is called Head #1. Figs. 6.9 and 6.10 show the measurement results before flying and Figs.

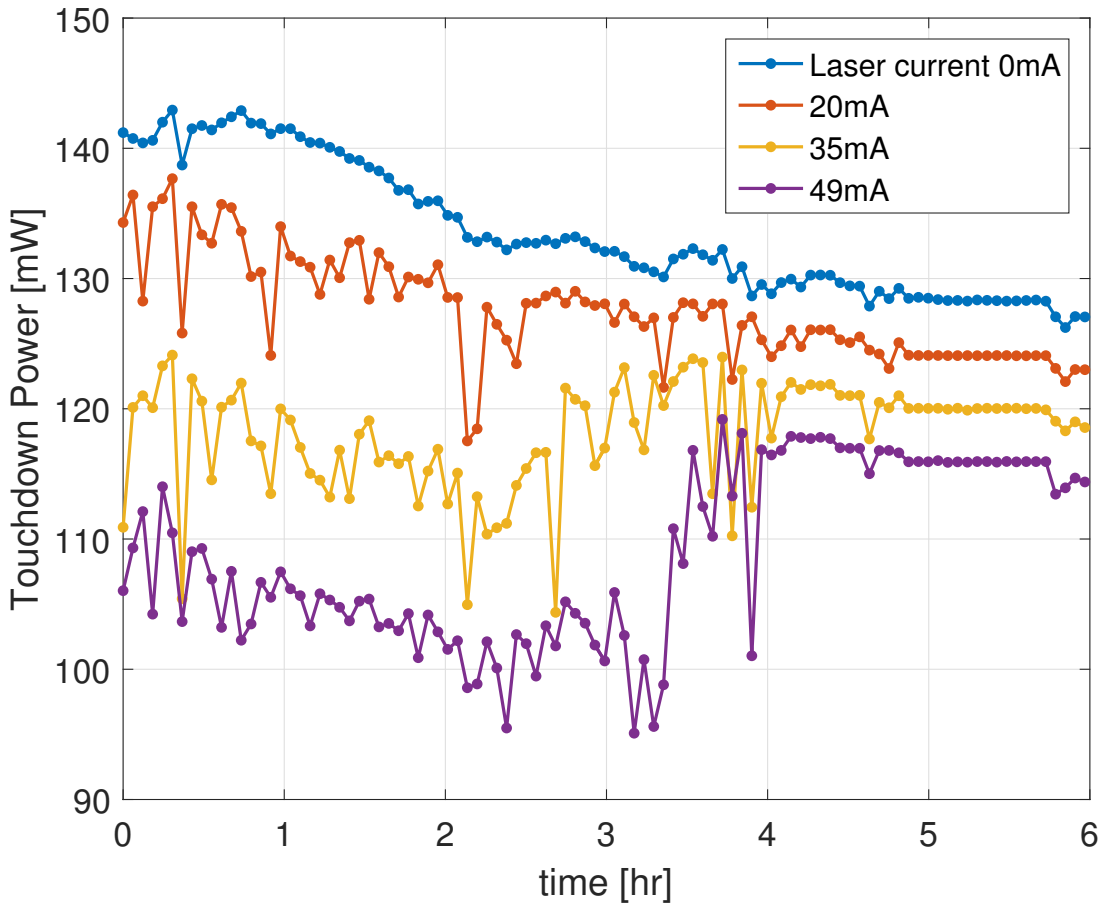

Figure 6.7: Touchdown power vs. time during the constant laser heating process for different laser currents: 0 mA, 20 mA, 35 mA and 49 mA.

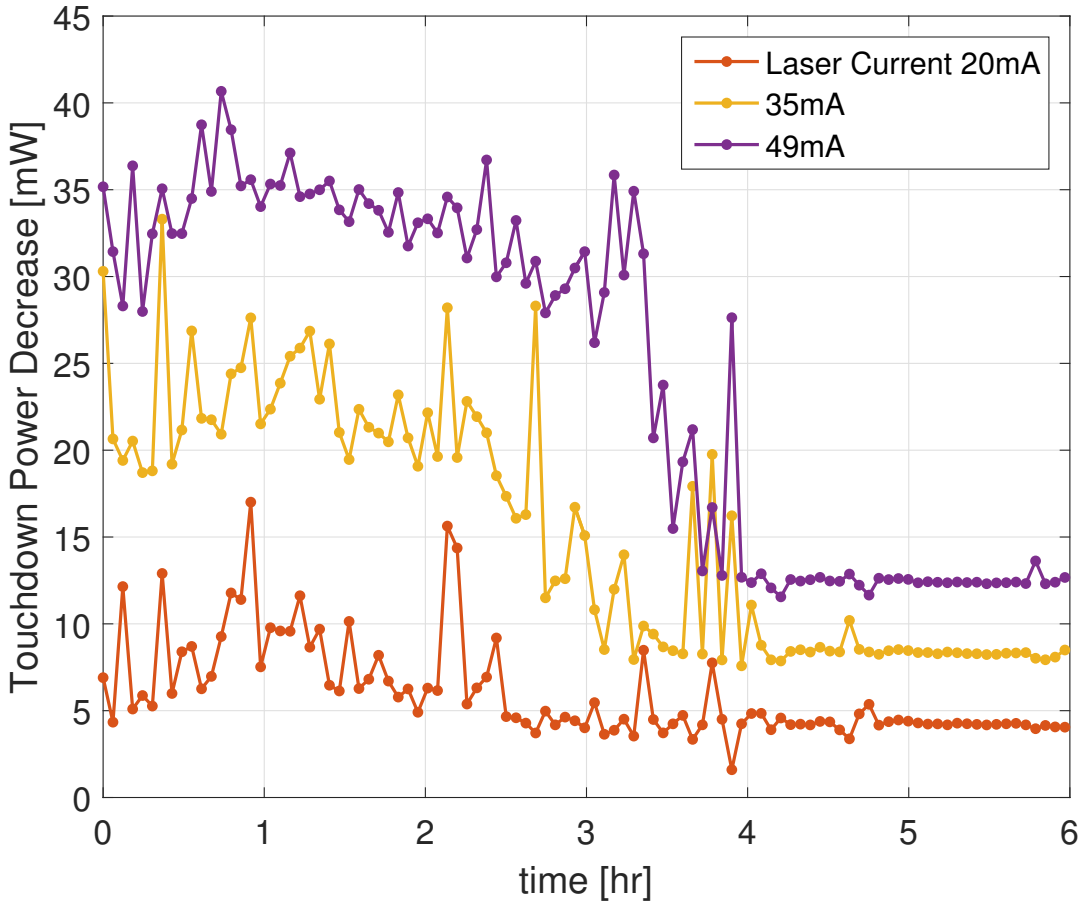

Figure 6.8: Touchdown power decrease vs. time during the constant laser heating process for different laser currents: 20 mA, 35 mA and 49 mA.

6.11 and 6.12 show them afterwards. Figs. 6.10 and 6.12 are the zoomed-in versions of Figs. 6.9 and 6.11, respectively. It can be seen in Figs. 6.9 and 6.10 that the head is somewhat dirty possibly due to its contamination during the head handling. However, as shown in Figs. 6.11 and 6.12, the pattern of the contamination formed on the head is totally different from what's shown in Figs 6.9 and 6.10. Some round-shaped patterns are formed on the surface, with the size of ∼2 µm and the height of ∼1 nm. The material of the pattern needs further investigation. As seen in Fig. 6.12, the contamination forms in the center of the waveguide, with the size of ∼220 nm and the height of ∼5.7 nm. This is similar to what is shown in Ref. [36]. The contamination can block the optical pathway from the waveguide to the media, resulting in inadequate heating of the media and the overheating of the head.

To verify that the contamination was formed due to the laser heating, another head, called Head #2, was also used under the same experimental procedure except that the laser was turned off during flying. The AFM measurements before and after flying are shown in Figs. 6.13, 6.14, 6.15 and 6.16. Figs. 6.13 and 6.14 show the measurement results before flying, and Figs. 6.15 and 6.16 show them afterwards. Figs. 6.14 and 6.16 are the zoomed-in versions of Figs. 6.13 and 6.15, respectively. It can be seen in Figs. 6.13 and 6.14 that the head is clean before flying. From Fig. 6.15, it can be seen that no round-shaped patterns are found on the ABS after flying without laser heating. As seen in Fig. 6.16, the area of the waveguide has no sign of solid contamination, except some debris due to the head-disk contact.

As a conclusion, the contamination formed on the head's surface is largely caused by the laser heating. With the head flying on the disk with the laser on, the contamination forms on both the head's surface and the location of the waveguide. The contamination on the head's surface results in the TDP decrease. Undesirable head-disk contact can happen due this decrease. The contamination formed at the waveguide can block the optical pathway, resulting in underheating of the media and the overheating of the head.

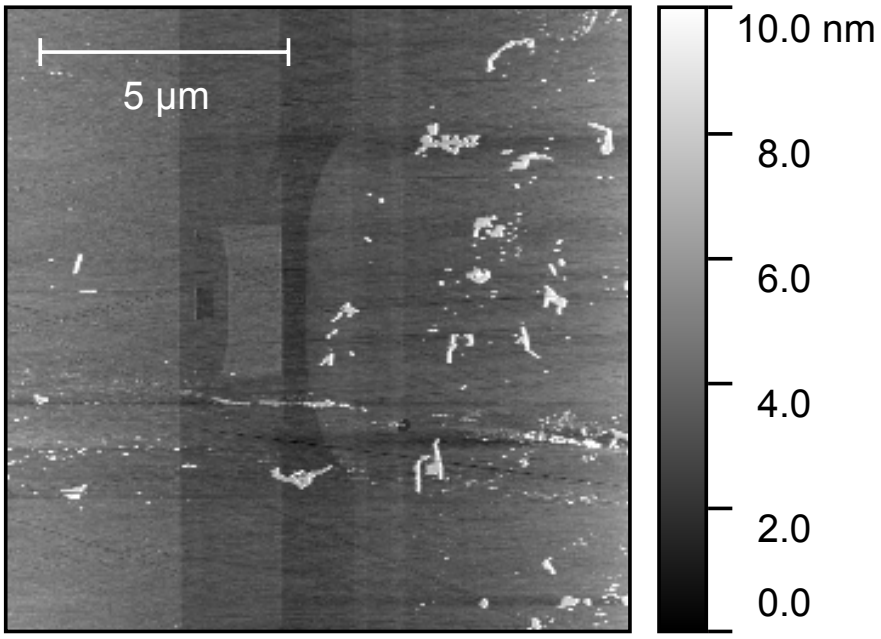

Figure 6.9: The AFM image of Head #1's ABS before flying.

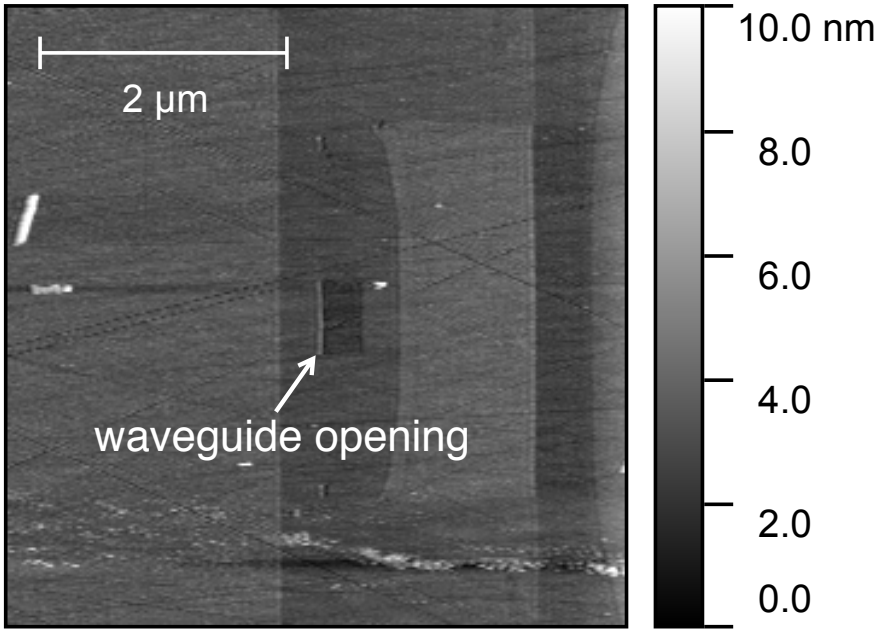

Figure 6.10: A zoom-in of Fig. 6.9

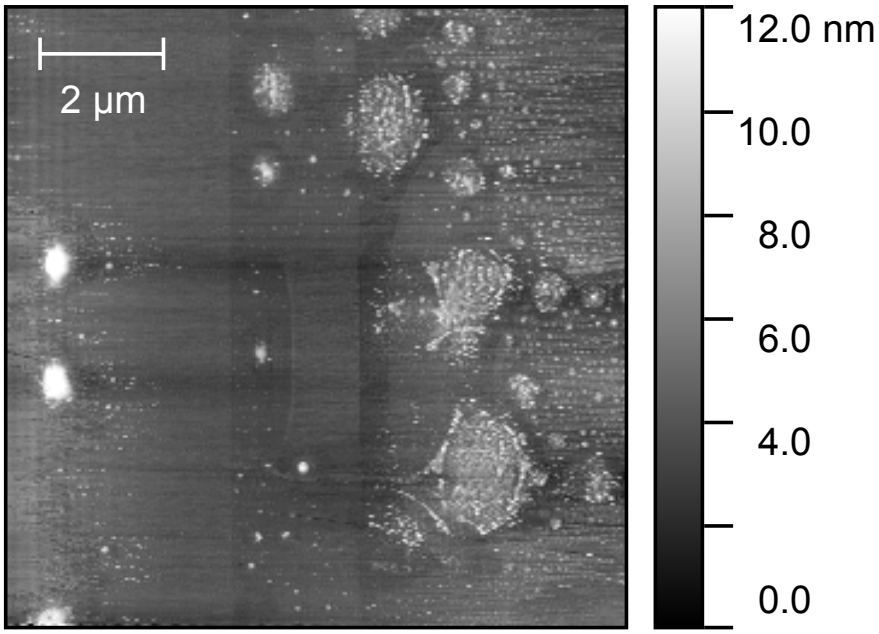

Figure 6.11: The AFM image of Head #1's ABS after flying.

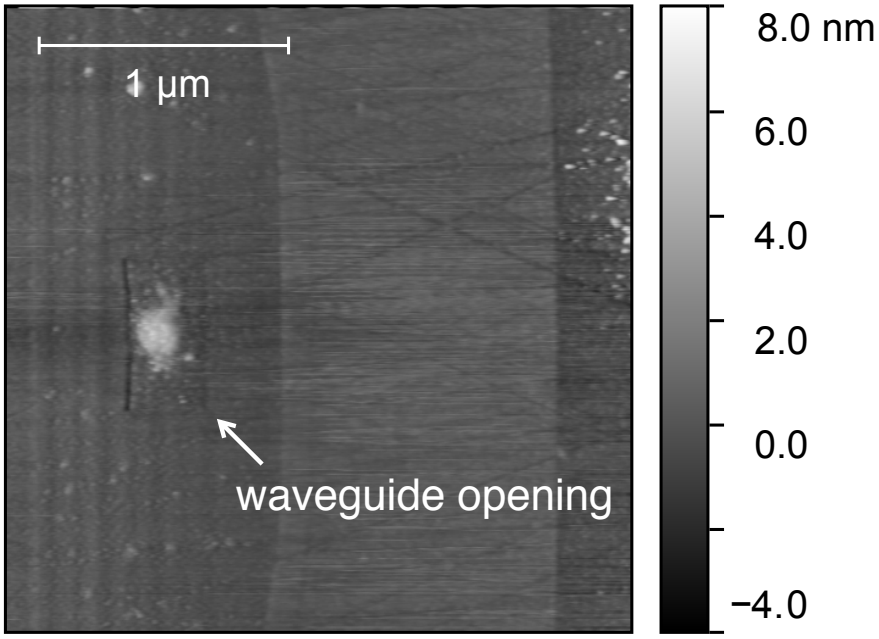

Figure 6.12: A zoom-in of Fig. 6.11

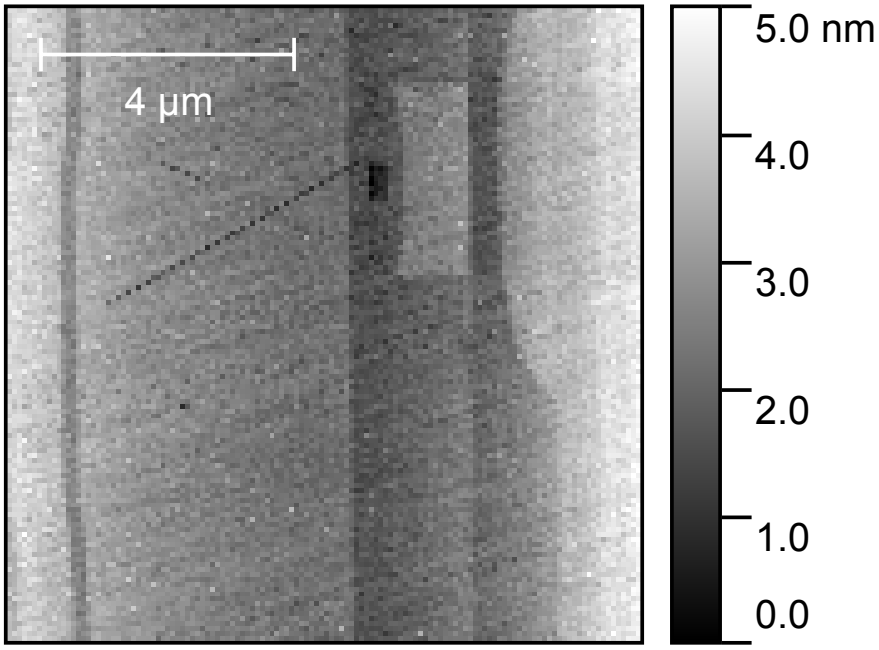

Figure 6.13: The AFM image of Head #2's ABS before flying.

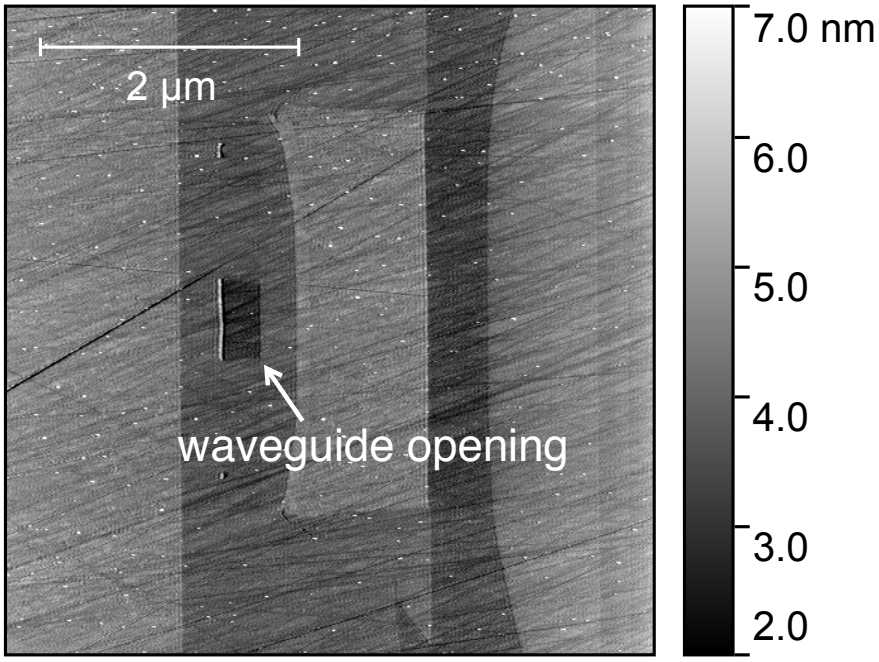

Figure 6.14: A zoom-in of Fig. 6.13

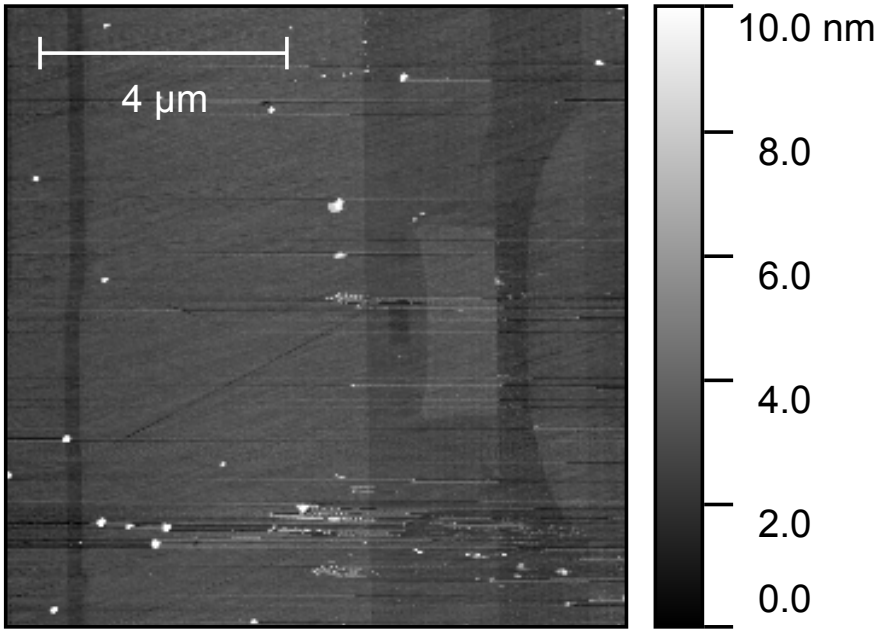

Figure 6.15: The AFM image of Head #2's ABS after flying.

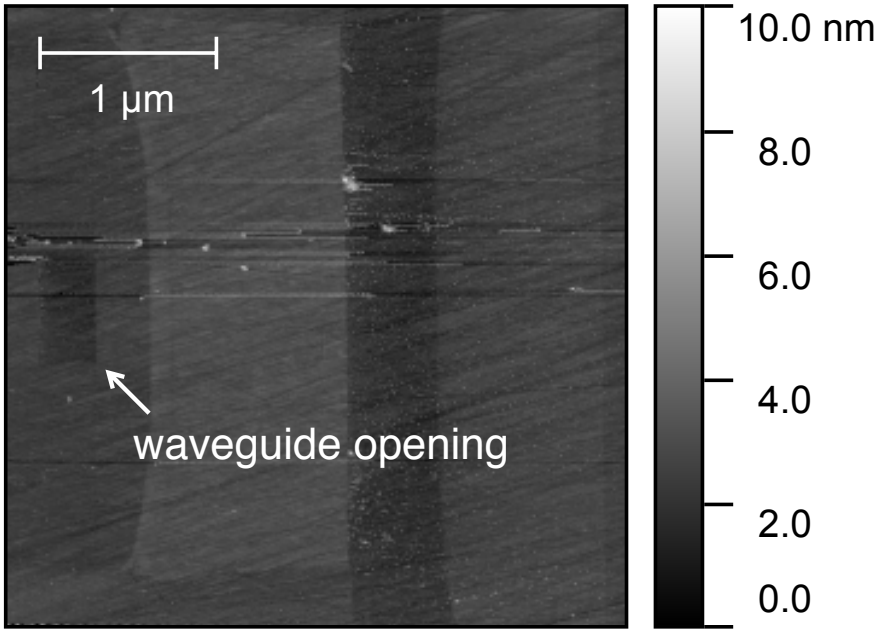

Figure 6.16: A zoom-in of Fig. 6.15

6.5 Summary

In this chapter, waveguide heads were used to study the laser-induced protrusion, slider dynamics change over the laser heating time and the laser induced head contamination. The first experiment shows that laser heating causes head protrusion and results in TD with less TFC power. The TFC power needs to be decreased accordingly in order to maintain the desired FH. The second experiment shows that the dynamics of the slider changes with the laser heating time. It is seen that the head-disk interaction increases in both the short and long time scales. The dominant interaction slider mode is the 1st pitch mode. The third experiment shows that the solid contamination forms on both the head's ABS and in the waveguide area. The contamination that forms on the waveguide can block the optical pathway and the contamination formed on the ABS can reduce the head-disk clearance, causing earlier TD. Overall, multiple unexpected phenomena can happen due to the laser heating. These issues need to be addressed before the waveguide head can be used with a reasonable reliability for HAMR production. Also, these experiments need to be repeated with HAMR heads that have the NFT.

Chapter 7

Lubricant Displacement and Reflow after Laser Heating in HAMR

7.1 Introduction

In current HDDs, about one-nanometer-thick lubricant is applied on the surface of the media to provide protection for the heads and disks, by reducing the friction and wear during accidental slider disk contact [81]. The lubricant films are synthesized from Perfluoropolyether molecules, e.g. Z-tetraol, which are stable enough to protect the disk at and around room temperature for at least five years.

On the other hand, as discussed earlier, high magnetic anisotropy materials need to be used in order to increase storage areal density beyond $1\,\mathrm{Tb/in^2}$. The magnetic state of this media is so stable at room temperature that current magnetic transducers are not able to switch its orientation. Therefore, HAMR technology [4] has been proposed to solve this problem. In HAMR, the magnetic layer is heated up to its Curie temperature with a laser such that the magnetic coercivity of the media is reduced and data writing with the magnetic transducers is possible.

Since the lubricant layer is on top of the COC and magnetic layer, they will also be heated locally to a similar temperature. The harsh heating condition can displace and damage traditional lubricants and reduce their lifetime due to evaporation, decomposition and thermal displacement [82, 83]. However, some of the lubricant displacement can be recovered due to reflow after a period of time. The reflow behavior can help to cure the lubricant displacement and reduce the chance of HDI failure. It is therefore important to understand the mechanisms and characteristics of the lubricant reflow behavior for HAMR systems.

In this chapter, experimental studies of lubricant reflow were performed using the CML-HAMR stage for a Z-tetraol type lubricant. Section 7.2 describes the experimental setup. The observed displacement and reflow behavior of the lubricant is discussed in Section 7.3. Section 7.4 introduces a numerical model for lubricant reflow and compares the numerical

simulation with the experimental results. Section 7.5 summarize the chapter.

7.2 Experimental conditions and procedure

The CML-HAMR stage was used to provide HAMR-like heating conditions on the disk to study the lubricant displacement and reflow behavior. Since HAMR disks were unavailable to us, PMR disks were used in this investigation. The disks were 3.5 in in diameter with aluminum substrates. The lubricant type was Z-tetraol with A20H additives, 60% bonding ratio and thickness of 0.95 nm.

A free space laser spot generated for the optical module was focused on the spinning disk, similar to the conditions as mentioned in Section 4.2. However, different from the back-heating experiment, the laser is focused directly onto the tested surface of the disk instead of passing through the substrate. The laser heats the disk and provides a HAMR-like condition. This illumination procedure contains three controllable parameters: laser power incident on the spinning disk (P_L), disks spinning speed (ω) and number of disk revolutions (repetitions) during laser illumination (n). P_L was controlled by optical filters between the laser generator and disk; ω and n were controlled by an in-house designed electronic controller using a FPGA board. The optical encoder in the spindle was used to count the number of revolutions of the disk, so the laser illumination repetitions (n) can be precisely controlled. The relationship between repetitions and laser illumination time is shown in Fig. 7.1.

The disk was exposed to the laser at a constant laser power while it was spinning at a constant speed for different repetitions at different tracks. The repetitions were from 1 to 1000 revs. Within two minutes after the laser exposure, the disk was measured by a Candela

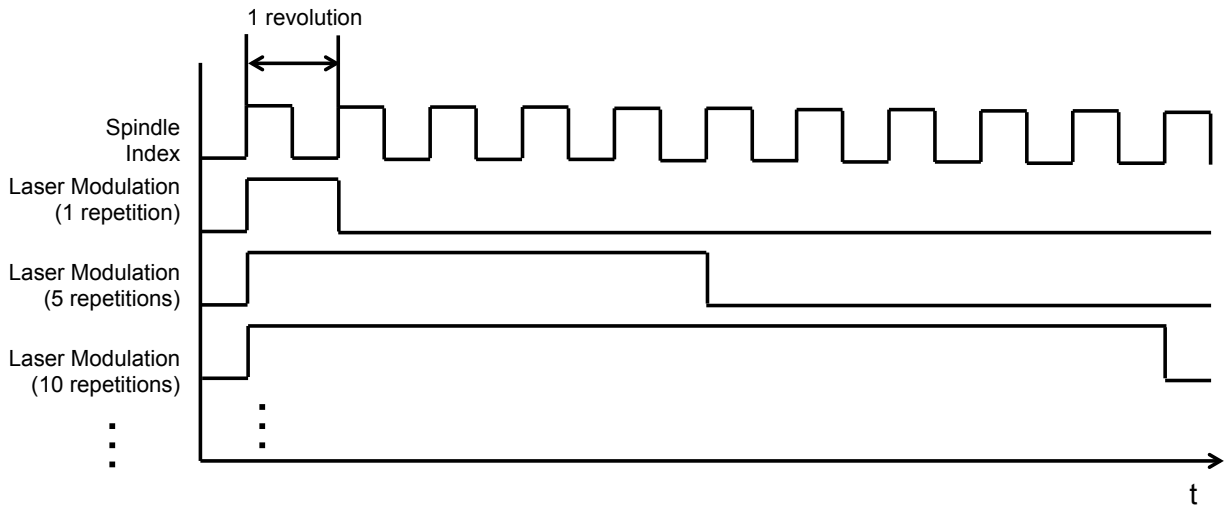

Figure 7.1: Modulation of laser by spindle index.

optical surface analyzer (OSA). The Q-Phase channel was used to measure the lubricant thickness change [84]. Scans by the OSA were taken periodically at room temperature at intervals of about 95 seconds up to about 22 minutes in total such that the lubricant profile could be recorded at different times. A scan was also taken again after 24 hours to see the final state of the lubricant.

7.3 Lubricant reflow process

Because of the spindle run-out, the raw Q-phase image of the lubricant showed some curvature and background. A script was developed to post process the images and eliminate the run-out curvature and non-uniform background. Examples of the processed OSA images are shown in Fig. 7.2.

As can be seen in Fig. 7.2(a), the parallel lines represent the tracks exposed to the laser for different numbers of revolutions. The increase of reflectivity in the Q-Phase indicates a lubricant thickness decrease. This is mainly due to lubricant displacement. Higher revolutions causes significantly more lubricant displacement as shown in Fig. 7.2 where the tracks on the top have a larger change of reflectivity. Figures 7.2(b)(c) show the OSA Q-phase images after some time has elapsed. Compared with Fig. 7.2(a), the reflectivity changes of the tracks in Figs. 7.2(b)(c) become smaller, indicating that the lubricant reflows back to the depleted region. Fig. 7.2(d) shows the reflection of the lubricant at steady state after 24 hours. It shows no apparent reflection when $n \leq 100$, which means that the lubricant has flowed back to its original state. The average of the lubricant displacement profile is shown in Fig. 7.3. It gives a clearer indication that the lubricant displacement tends to ease in the measured time frame.

The lubricant displacement and reflow profiles can be obtained from the OSA Q-phase image at different times. Fig. 7.4 shows the maximum lubricant displacement depth as a function of time for one set of experiments. The experimental parameters of the figure were $\omega = 600\,\mathrm{RPM}$ and $P_L = 165\,\mathrm{mW}$. Illumination repetitions were 100, 50 and 5, respectively.

As shown in Fig. 7.4, the initial lubricant displacement is more severe when the disk is illuminated for more repetitions. To exclude the effect of different initial lubricant displacement on the reflow, we normalized the lubricant displacement by its initial value as shown in Fig. 7.4(b). The lubricant displacement decreases as time elapses, which indicates that the lubricant reflows back to the depleted area. The reflow rate is initially fast and decreases with time. Almost 80% of the lubricant recovers within about 20-minutes of relaxation at room temperature [66].

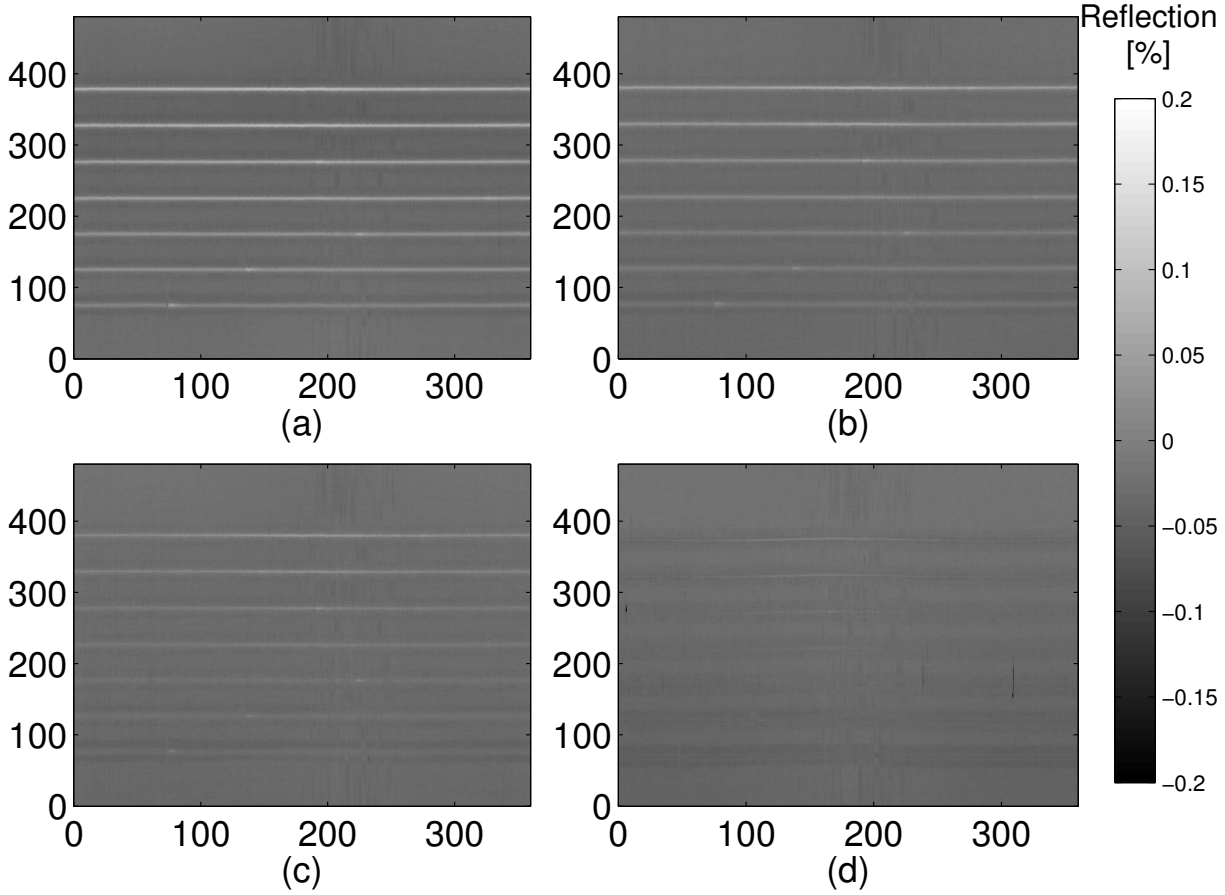

Figure 7.2: OSA scanning images of relative reflectivity on a disk after certain repetitions of illumination by laser at: (a) 0 minutes, (b) 3 minutes, (c) 9 minutes and (d) 24 hours respectively. The x-axis is the angular position in units of degrees and the y-axis is the relative radial position in units of µm. The relative reflectivity slowly fades as time elapses. The repetition number from top to bottom for the seven tracks are 1000, 500, 100, 50, 10, 5, 1, respectively.

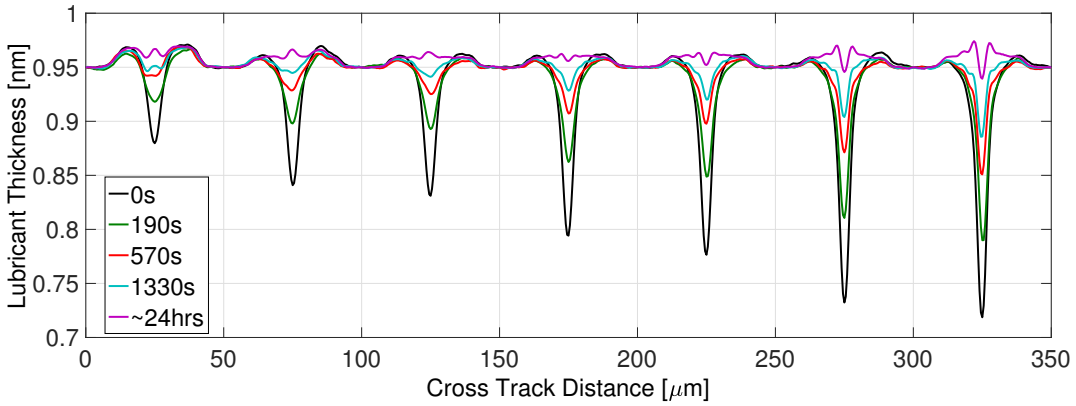

Figure 7.3: The average displacement of the lubricant. The repetition number from left to right for the seven peaks are 1, 5, 10, 50, 100, 500, 1000, respectively.

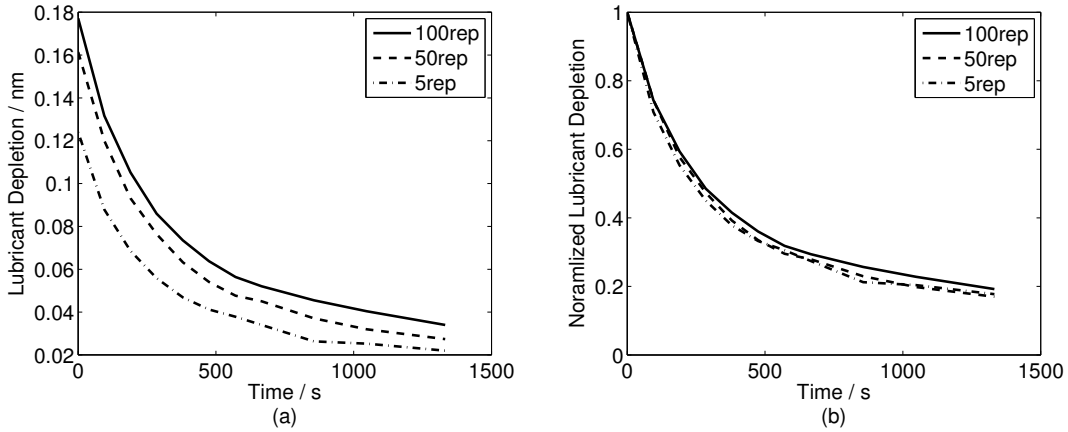

Figure 7.4: Lubricant relaxation after laser displacement. (a) The three different lines show different laser illumination repetitions. Less repetitions result in shallower initial lubricant displacement. The reflow trends are similar for the three different conditions. (b) Lubricant displacement normalized with respect to initial value. The displacement is set to 1 at time zero. Similar trends are shown.

7.4 Comparison between simulation and experiments

Simulations of lubricant reflow were carried out to compare them with the experimental results [65]. The lubricant reflow was described using continuum theory with a modified (effective) viscosity [85]. Within the continuum approach, the dimensions of the thin film on the disk surface make it possible to use lubrication theory and thus we obtain the governing equations described in the equation,

$$\frac{\partial h}{\partial t} + \frac{1}{3\mu}\frac{\partial}{\partial x}\left[h^3 \frac{\mathrm{d}\Pi(h)}{\mathrm{d}h}\frac{\partial h}{\partial x}\right] = 0 \tag{7.1}$$

where $h = h(x,t)$ is the film thickness, μ is the effective lubricant viscosity, $\Pi(h)$ is the disjoining pressure arising from van der Waals interactions between the lubricant and the solid substrate [86]. This disjoining pressure is of the form $\Pi(h) = Ah^{-3}$, where A is the Hamaker constant. The initial condition, as seen in Fig. 7.5(a), was given by the lubricant displacement profile obtained in the experiments at time zero. As boundary conditions we considered zero volume flow at the right and left boundaries. This condition is equivalent to setting $\frac{\mathrm{d}h}{\mathrm{d}x} = 0$ at the boundaries. It can be observed that Eq. 7.1 depends only on the ratio of the Hamaker constant to lubricant viscosity. This ratio was adjusted to give the best match to the experimental results. The simulation results of lubricant reflow are shown in Fig. 7.5.

It can be seen from Fig. 7.5(b) that the simulation results fit adequately the experimental data. However, there exist regions of some discrepancy. In the first 400 seconds of reflow, the simulation results show a faster recovery rate than the experiments. After this time, the

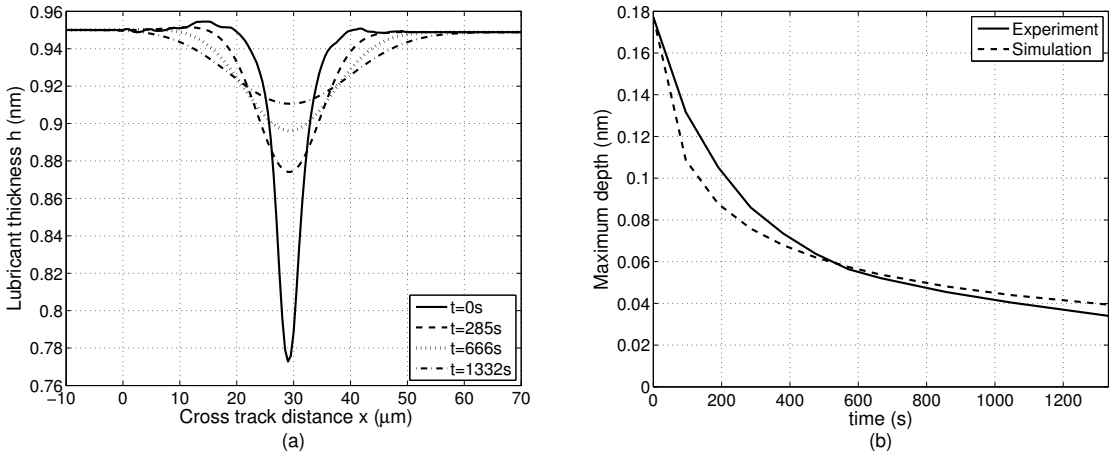

Figure 7.5: (a) Film thickness profile at selected times obtained from simulations. (b) Depth of the maximum displacement point in the film as obtained from experiments and results. The experiment parameters are $\omega = 600\,\mathrm{RPM}$, $P_L = 165\,\mathrm{mW}$ and $n = 100$. The simulation parameters are $\mu = 1.5\,\mathrm{Pa\,s}$ and $1 \times 10^{-21}\,\mathrm{J}$.

reflow in the simulation slows down relative to the experiments. This discrepancy may be explained by noting that the lubricant viscosity of thin films can be thickness dependent as discussed in [87]. This phenomenon was not included in the present simulation model.

7.5 Summary

In this chapter, the thermal displacement behavior of Z-tetraol due to a free laser beam heating condition as well as the recovery behavior after heating were studied. The initial lubricant displacement was different for different laser heating conditions, i.e., a longer heating duration causes more lubricant displacement. However, a similar trend was found regardless of initial lubricant displacement. Almost 80% of the lubricant reflows back within 20 minutes at room temperature. Simulation results show a reasonably good agreement with experiments.

It is noted that the real HAMR laser conditions incorporate an NFT as a heating method to achieve heated spots of tens of nanometers rather than a few microns. So the NFT heating has a spot size a few orders of magnitude smaller and its duration is a few orders of magnitude shorter than our free laser beam heating. Nevertheless the lubricant behavior under the conditions reported here gives insight into lubricant depletion and reflow for HAMR systems.

Chapter 8

Summary and Future Works

8.1 Summary

In this study, the head-disk interface (HDI) of the heat assisted magnetic recording (HAMR) system was experimentally studied using the Computer Mechanics Laboratory (CML) - HAMR stage. Different aspects of the HDI were investigated, including the embedded contact sensor (ECS) contact detection, the head's temperature change during laser heating, the heat transfer change with respect to the fly-height (FH), the HDI change caused by the embedded laser heating and the lubricant depletion and reflow due to the laser heating.

In Chapter 1, the basic principle of the hard disk drive (HDD) and its amazing development was briefly introduced. The trilemma of adequate signal-to-noise-ratio (SNR), thermal stability and write-ability in the HDD was discussed, and HAMR technology was introduced. In HAMR, the trilemma is conquered by locally and momentarily heating the media to the Curie temperature during writing such that the write-ability is achieved. However, since high-temperature heating is involved, material deformation and transfer can happen, which needs investigation.

In Chapter 2, the electrical elements in the recording head were introduced. These include the thermal fly-height control (TFC) heater, the ECS and the laser power delivery system (LPDS). The TFC heater makes use of the material's thermal expansion to control the slider's air bearing surface (ABS) topography and thus the FH. The ECS utilizes the resistance change as a function of temperature to detect the head-disk contact. Different TD detection methods using the ECS were experimentally investigated. It was concluded that the ECS temperature change rate with the TFC power can be used as the detection method if early detection is desired. The LPDS is the key part of the HAMR head where the optical energy is generated from the laser diode (LD) and focused by the near field transducer (NFT). The lollipop type NFT and the bowtie type NFT were modeled and numerically studied. It was found that the coupling efficiency of the bowtie NFT is 3.0% and that of the lollipop NFT is 5.7%. The waveguide head without the NFT was tested. The LD's equivalent resistance - current relationship was characterized and it was found that the LD's

consumed power is 180 mW when the laser current is 58 mA.

In Chapter 3, two experimental stages were introduced. The CML-HAMR stage is a comprehensive stage including an optical module, a spinstand module and a signal generation/acquisition module. The stage is capable of simulating the HAMR scenario. The optical stage can generate a beam of laser light up to 1 W at the wavelength of 780 nm and focus it to full-width-half-maximum (FWHM) of $\sim$2 µm $\times$ 5 µm. The spinstand module can control the spinning of the disk at different speeds and the positions of the HGA. The signal generation/acquisition module is designed for generating and recording the electrical signal to/from the system. It's maximum sampling frequency is 1 MS/s. Different modules of LabView-based software were written in order to perform the various experiments. Most of the experiments in this dissertation were performed on the CML-HAMR stage. The ECS calibration stage is a special stage used for ECS resistance-temperature calibration. With it, the temperature coefficient of resistance of the ECS can be calibrated. It was found that the temperature coefficient of resistance of the ECS of the heads used in the experiments is 3.5×10^{-3}/K.

In Chapter 4, the "back-heating" experiment was performed in order to estimate the head's temperature during HAMR laser heating. The experiment was performed on the CML-HAMR stage with a beam of free-space laser focusing on the back side of a one-sided disk with a PMR head flying on the other side. The experiment showed that the ECS on the head's ABS is both heated by the TFC heater and the laser light, which can be decoupled. It shows that the ECS temperature rise due to the laser heating (θ_E^L) is linear with the disk temperature rise (θ_D), which can be calibrated by use of a phase change material. The head-disk temperature rise ratio is calculated to be 0.308, 0.292, 0.280 and 0.269 when the FH is 0 nm, 1 nm, 2 nm and 3 nm, respectively. It is estimated, based on the linear extrapolation, that the ECS temperature rise is 139 K, 132 K, 127 K and 122 K when the disk is heated to the Curie temperature, where the temperature rise is 452 K.

In Chapter 5, the self-heating effect of the ECS was investigated. The ECS can heat itself when its current bias is relatively high. It was discovered that the ECS temperature rise due to the self heating is linear with the electric power supplied to it. The self heating rate, defined as the ratio of the ECS temperature rise to the ECS power, was measured to be 200.2 K/mW. When the ECS current is less than or equal to 0.5 mA, the ECS self heating effect can be neglected. A ECS-TFC heating experiment was also performed at different FHs and disk rotating speeds. The normalized ECS self heating temperature rise, an indicator of the heat transfer in the HDI, was measured. It was concluded that the heat transfer coefficient across the HDI strongly depends on the width of the gap, especially when the gap size is smaller than 1 nm. The experimental result was compared with the result in Ref. [76] and their differences were discussed.

In Chapter 6, the head disk interaction during the laser heating was studied using the waveguide head. It shows that the laser heating can cause additional head surface protrusion. This lowers the FH and results in early TD. It was concluded that the ratio of touchdown power (TDP) reduction to the laser current is 0.3 mW/mA. This additional protrusion needs compensation on the TFC power to avoid excessive head wear. The dynamics of the head

also changes during the laser heating. A set of constant laser heating experiments were also performed. It was found that the acoustic emission (AE) signal's magnitude increased in both short term and long term. The short-time Fourier transform (STFT) shows that the magnification is mainly at 100 kHz, corresponding to the 1st pitch mode. The increase of the AE signal was likely due to the contamination formed on the head. This accumulation on the head was also investigated. It was found from the atomic force microscope (AFM) images that solid contamination forms in the center of the waveguide caused by the laser heating. There were also round shape contamination spots formed on the head's ABS after laser heating, which do not exist in the reference case. It is concluded that the laser heating can cause excessive contaminant accumulation on the head, adversely affecting the head's lifetime.

In Chapter 7, the lubricant reflow after laser heating was studied. In the experiment, a beam of free space laser focused on the rotating disk at different laser powers, disk rotating speeds and repetitions. Then the disk was brought to the OSA for lubricant scanning. It was found that 80% of the lubricant displacement recovered within 20 minutes. A simulation of this process was also performed. The experiment and the simulation match each other reasonably well.

Overall, several different aspects of the HDI in HAMR were studied in this dissertation, including the heat transfer in the HDI, the material transfer and the lubricant reflow. Various new phenomena occur in HAMR conditions. Due to the fact that the HAMR heating is at the nanoscale, both spatially and temporally, the HAMR related experiments are especially challenging to carry out, and some new and unexpected phenomena are hard to explain. It is hoped that this dissertation serves as a basis and suggestion for experiments to be done for HAMR and can help accelerate the development of the HAMR technology.

8.2 Future Works

In late 2017, Seagate announced that it had started shipping HAMR HDDs to selected customers for integration tests [88]. It was also stated that the areal density of the HAMR drives had reached 2 Tbpsi. It has been gratifying to witness the development advancement of HAMR over the last five years. There have been many technical difficulties to overcome in order to realize such a complex technology, including the design and optimization of the head and media structure, carbon overcoat (COC) and lubricant issues, the reliability of the NFT, etc. With continuous hardworking of the scientists and engineers, it is hoped and expected that HAMR drives can improve over time and finally come on the market.

The critical details of HAMR design have remained confidential information within the industry. At the time of this writing, fully functional HAMR heads and media are still not available to us for study. Even the waveguide heads were provided just about one year ago. It is expected that with HAMR products now being available on a limited scale, more HAMR related material can be provided to university laboratories.

Since the HAMR technology has now been shown to be feasible, more future studies can be performed to increase its reliability and reduce its cost. Following is a non-exhaustive list of potential future works:

1. The heat transfer mechanism in the nanoscale gap is still not fully understood, but it is important to the reliability of the NFT. More experiments can be performed using current settings as described in Chapters 4 and 5 with heads that have dual heaters and dual ECS's. The additional heater will give more control over the thermal profile of the head, and with two ECS's, the thermal gradient on the head can be measured.

2. The mechanism of the formation of the contamination on the head during laser heating can be further investigated using the waveguide heads. The HAMR heads are also important for this study when industry is able to provide them. More frequent AFM scans of the head during laser heating can help reveal more about the time frame of the contamination formation. Numerical modeling can also help to understand its mechanism.

3. The depletion and the degradation of the lubricant and the COC on the media needs to be studied further. In current work, the disk was heated by a free space laser. In the future, the laser heating can be applied by either the waveguide head or the HAMR head. With different length scales, the behaviour of the lubricant and the COC could show different phenomena. It is also important to compare the experimental results with the modeling results.

4. The deformation of the disk caused by the laser heating should also be studied further. Although the head and the disk are in relative motion, the laser spot on the media remains with the head. Therefore, it is important to know the protrusion caused by the laser heating and how it affects the head disk contact.

5. Recently it was proposed that the magnetic material can be heated to a temperature somewhat lower than Curie temperature during writing. This may have benefits by reducing the NFT's temperature. However, it is unknown how much the heating temperature can be reduced. Therefore, it is important to investigate the relationship between the demagnetization of the media and its temperature.

Finally, the author wants to express his sincere hope that the technical challenges of HAMR can be conquered and the product can be released to the public soon.

Bibliography

[1] David Reinsel, John Gantz, and John Rydning. *Data Age 2025: The Evolution of Data to Life-Critical*. Tech. rep. [Online; accessed 7-May-2018]. International Data Corporation, 2017. URL: https://www.seagate.com/www-content/our-story/trends/files/Seagate-WP-DataAge2025-March-2017.pdf.

[2] *Global shipments hard disk drives (HDD) 1976-2020*. [Online; accessed 7-May-2018]. URL: https://www.statista.com/statistics/398951/global-shipment-figures-for-hard-disk-drives/.

[3] M. H. Kryder et al. "Heat Assisted Magnetic Recording". In: *Proceedings of the IEEE* 96.11 (Nov. 2008), pp. 1810–1835. ISSN: 0018-9219. DOI: 10.1109/JPROC.2008.2004315.

[4] WA Challener et al. "Heat-assisted magnetic recording by a near-field transducer with efficient optical energy transfer". In: *Nature Photonics* 3.4 (2009), p. 220. DOI: 10.1038/nphoton.2009.26.

[5] Robert E Rottmayer et al. "Heat-Assisted Magnetic Recording". In: *IEEE Transactions on Magnetics* 42.10 (Oct. 2006), pp. 2417–2421. ISSN: 0018-9464. DOI: 10.1109/TMAG.2006.879572.

[6] William A Challener. *Heat assisted magnetic recording head with a planar waveguide*. US Patent 6,944,112. Sept. 2005.

[7] Roger Wood, Yimin Hsu, and Marilee Schultz. *Perpendicular Magnetic Recording Technology*. Tech. rep. [Online; accessed 7-May-2018]. HGST, Western Digital Company, 2007. URL: https://www.hgst.com/sites/default/files/resources/PMR_white_paper_final.pdf.

[8] D. Weller et al. "A HAMR Media Technology Roadmap to an Areal Density of 4 Tb/in^2". In: *IEEE Transactions on Magnetics* 50.1 (Jan. 2014), pp. 1–8. ISSN: 0018-9464. DOI: 10.1109/TMAG.2013.2281027.

[9] Bo Liu et al. "Femto slider: fabrication and evaluation". In: *IEEE Transactions on Magnetics* 39.2 (Mar. 2003), pp. 909–914. ISSN: 0018-9464. DOI: 10.1109/TMAG.2003.808919.

[10] Chun Lian Ong et al. "Dual track Wallace fly height measurement method to monitor slider motion in 2 dimension at near contact regime". In: *Microsystem Technologies* 22.6 (June 2016), pp. 1177–1180. ISSN: 1432-1858. DOI: 10.1007/s00542-015-2686-1.

[11] Michel Julliere. "Tunneling between ferromagnetic films". In: *Physics Letters A* 54.3 (1975), pp. 225–226. ISSN: 0375-9601. DOI: 10.1016/0375-9601(75)90174-7.

[12] Sining Mao et al. "Commercial TMR heads for hard disk drives: characterization and extendibility at 300 gbit/in^2". In: *IEEE Transactions on Magnetics* 42.2 (Feb. 2006), pp. 97–102. ISSN: 0018-9464. DOI: 10.1109/TMAG.2005.861788.

[13] *2014: HDD areal density reaches 1 terabit/sq. in.* [Online; accessed 7-May-2018]. 2014. URL: http://www.computerhistory.org/storageengine/hdd-areal-density-reaches-1-terabit-sq-in/.

[14] Bruno Marchon et al. "The head-disk interface roadmap to an areal density of Tbit/in^2". In: *Advances in Tribology* 2013 (2013). DOI: 10.1155/2013/521086.

[15] *IBM 350 disk storage unit*. [Online; accessed 7-May-2018]. URL: http://www-03.ibm.com/ibm/history/exhibits/storage/storage_350.html.

[16] Albert S. Hoagland. *IBM 350 RAMAC*. [Online; accessed 7-May-2018]. Mar. 2013. URL: http://s3.computerhistory.org/groups/ibm-350-ramac.pdf.

[17] *1956: First commercial hard disk drive shipped*. [Online; accessed 7-May-2018]. URL: http://www.computerhistory.org/storageengine/first-commercial-hard-disk-drive-shipped/.

[18] Wikipedia contributors. *IBM 305 RAMAC — Wikipedia, The Free Encyclopedia*. [Online; accessed 7-May-2018]. 2017. URL: https://en.wikipedia.org/w/index.php?title=IBM_305_RAMAC&oldid=816349004.

[19] *HGST Ultrastar He^{12} Data Sheet - 3.5-Inch Helium Platform Enterprise Hard Disk Drives*. [Online; accessed 7-May-2018]. Feb. 2018. URL: https://www.hgst.com/sites/default/files/resources/Ultrastar-He12-datasheet.pdf.

[20] Masayuki Kurita et al. "Active flying-height control slider using MEMS thermal actuator". In: *Microsystem Technologies* 12.4 (Mar. 2006), pp. 369–375. ISSN: 1432-1858. DOI: 10.1007/s00542-006-0104-4.

[21] Jinglin Zheng et al. "Effects of Altitude on Thermal Flying-Height Control Actuation". In: *Tribology Letters* 40.3 (Dec. 2010), pp. 295–299. ISSN: 1573-2711. DOI: 10.1007/s11249-010-9661-x.

[22] Tim Feldman and Garth Gibson. "Shingled magnetic recording: Areal density increase requires new data management". In: *USENIX; login: Magazine* 38.3 (2013). [Online; accessed 7-May-2018]. URL: https://www.usenix.org/system/files/login/articles/05_feldman_022-030_final.pdf.

[23] Jonathan Darrel Coker et al. *Shingled magnetic recording (SMR) disk drive with verification of written data*. US Patent 8,665,545. Mar. 2014.

[24] Jiaping Yang, Cheng Peng Henry Tan, and Eng Hong Ong. "Thermal analysis of helium-filled enterprise disk drive". In: *Microsystem Technologies* 16.10 (Oct. 2010), pp. 1699–1704. ISSN: 1432-1858. DOI: 10.1007/s00542-010-1121-x.

[25] Shiying Zhou and Masayoshi Tomizuka. "Enhanced anti-windup compensation for the dual stage hard disk drive systems with amplitude saturation". In: *2016 IEEE International Conference on Advanced Intelligent Mechatronics (AIM)*. IEEE. July 2016, pp. 822–827. DOI: 10.1109/AIM.2016.7576870.

[26] *Breaking Capacity Barriers With Seagate Shingled Magnetic Recording*. [Online; accessed 7-May-2018]. URL: https://www.seagate.com/tech-insights/breaking-areal-density-barriers-with-seagate-smr-master-ti/.

[27] Minghui Zheng, Shiying Zhou, and Masayoshi Tomizuka. "Identification of Resonance Frequencies in Dual-Stage Hard Disk Drives: A Practical Strategy". In: *ASME 2017 Dynamic Systems and Control Conference*. American Society of Mechanical Engineers. 2017, V002T23A001. DOI: 10.1115/DSCC2017-5096.

[28] Shiying Zhou et al. "Control of Dual-Stage HDDs With Enhanced Repetitive Disturbance Rejection". In: *ASME 2017 Conference on Information Storage and Processing Systems collocated with the ASME 2017 Conference on Information Storage and Processing Systems*. American Society of Mechanical Engineers. 2017, V001T03A002–V001T03A002. DOI: 10.1115/ISPS2017-5432.

[29] Shiying Zhou. "Adaptive Feedforward and Anti-windup Compensation for Amplitude and Rate Saturation with Application to Precision Control". PhD thesis. UC Berkeley, 2017. URL: https://escholarship.org/uc/item/7xr7761p.

[30] Edward Grochowski and Roger F Hoyt. "Future trends in hard disk drives". In: *IEEE Transactions on Magnetics* 32.3 (May 1996), pp. 1850–1854. ISSN: 0018-9464. DOI: 10.1109/20.492876.

[31] Wikipedia contributors. *Superparamagnetism — Wikipedia, The Free Encyclopedia*. [Online; accessed 7-May-2018]. 2018. URL: https://en.wikipedia.org/w/index.php?title=Superparamagnetism&oldid=832216911.

[32] H J Richter. "The transition from longitudinal to perpendicular recording". In: *Journal of Physics D: Applied Physics* 40.9 (2007), R149. DOI: 10.1088/0022-3727/40/9/R01.

[33] D. Weller et al. "High K_u materials approach to 100 Gbits/in^2". In: *IEEE Transactions on Magnetics* 36.1 (Jan. 2000), pp. 10–15. ISSN: 0018-9464. DOI: 10.1109/20.824418.

[34] Jia-Yang Juang and Jinglin Zheng. "Thermal analysis of continuous and patterned multilayer films in the presence of a nanoscale hot spot". In: *AIP Advances* 6.10 (2016), p. 105102. DOI: 10.1063/1.4964497.

[35] Shaomin Xiong et al. "Material Transfer Inside Head Disk Interface for Heat Assisted Magnetic Recording". In: *Tribology Letters* 65.2 (Apr. 2017), p. 74. ISSN: 1573-2711. DOI: 10.1007/s11249-017-0860-6.

[36] J. D. Kiely et al. "Write-Induced Head Contamination in Heat-Assisted Magnetic Recording". In: *IEEE Transactions on Magnetics* 53.2 (Feb. 2017), pp. 1–7. ISSN: 0018-9464. DOI: 10.1109/TMAG.2016.2618842.

[37] Dallas W Meyer, Paul E Kupinski, and Joseph C Liu. *Slider with temperature responsive transducer positioning*. US Patent 5,991,113. Nov. 1999.

[38] Brian E Schultz. *Thermal Fly-height Control (TFC) Technology in HGST Hard Disk Drives*. Tech. rep. [Online; accessed 7-May-2018]. HGST, Western Digital Company, 2007. URL: https://www.hgst.com/sites/default/files/resources/TFC_whitepaper041807.pdf.

[39] J. Y. Juang et al. "Numerical and Experimental Analyses of Nanometer-Scale Flying Height Control of Magnetic Head With Heating Element". In: *IEEE Transactions on Magnetics* 44.11 (Nov. 2008), pp. 3679–3682. ISSN: 0018-9464. DOI: 10.1109/TMAG.2008.2002612.

[40] Hui Li et al. "Simulation of Flying Height and Response Time of Thermal Flying Height Control Sliders With Thermal Insulators". In: *IEEE Transactions on Magnetics* 46.6 (June 2010), pp. 1292–1294. ISSN: 0018-9464. DOI: 10.1109/TMAG.2010.2040025.

[41] Jin Liu, Junguo Xu, and Jianhua Li. "Simulation studies of contact sensor for disk defect mapping". In: *Microsystem Technologies* 19.9 (Sept. 2013), pp. 1441–1448. ISSN: 1432-1858. DOI: 10.1007/s00542-013-1838-4.

[42] Jianhua Li et al. "Thermal mechanics of a contact sensor used in hard disk drives". In: *Microsystem Technologies* 19.9 (Sept. 2013), pp. 1607–1614. ISSN: 1432-1858. DOI: 10.1007/s00542-013-1870-4.

[43] J. Xu et al. "Contact/Clearance Sensor for HDI Subnanometer Regime". In: *IEEE Transactions on Magnetics* 50.3 (Mar. 2014), pp. 114–118. ISSN: 0018-9464. DOI: 10.1109/TMAG.2013.2286619.

[44] J. Xu et al. "Pit Detection Using a Contact Sensor". In: *IEEE Transactions on Magnetics* 49.6 (June 2013), pp. 2715–2718. ISSN: 0018-9464. DOI: 10.1109/TMAG.2013.2251867.

[45] Chuanwei Zhang et al. "Effect of a void on the heat transfer in the head disk interface". In: *Microsystem Technologies* 21.12 (Dec. 2015), pp. 2597–2603. ISSN: 1432-1858. DOI: 10.1007/s00542-015-2501-z.

[46] William A. Challener et al. "Miniature planar solid immersion mirror with focused spot less than a quarter wavelength". In: *Opt. Express* 13.18 (Sept. 2005), pp. 7189–7197. DOI: 10.1364/OPEX.13.007189.

[47] P. F. Liao and A. Wokaun. "Lightning rod effect in surface enhanced Raman scattering". In: *The Journal of Chemical Physics* 76.1 (1982), pp. 751–752. DOI: 10.1063/1.442690.

[48] S. Bhargava and E. Yablonovitch. "Lowering HAMR Near-Field Transducer Temperature via Inverse Electromagnetic Design". In: *IEEE Transactions on Magnetics* 51.4 (Apr. 2015), pp. 1–7. ISSN: 0018-9464. DOI: 10.1109/TMAG.2014.2355215.

[49] Bair V. Budaev and David B. Bogy. "On the lifetime of plasmonic transducers in heat assisted magnetic recording". In: *Journal of Applied Physics* 112.3 (2012), p. 034512. DOI: 10.1063/1.4745050.

[50] G. Baffou, R. Quidant, and C. Girard. "Heat generation in plasmonic nanostructures: Influence of morphology". In: *Applied Physics Letters* 94.15 (2009), p. 153109. DOI: 10.1063/1.3116645.

[51] Nan Zhou et al. "Plasmonic near-field transducer for heat-assisted magnetic recording". In: *Nanophotonics* 3.3 (2014), pp. 141–155. DOI: 10.1515/nanoph-2014-0001.

[52] Yueqiang Hu et al. "Nanoscale thermal analysis for heat-assisted magnetic recording". In: *Journal of Applied Physics* 122.13 (2017), p. 134303. DOI: 10.1063/1.4996749.

[53] Yueqiang Hu et al. "A Numerical Investigation of the Nanoscale Heat Transfer in Heat Assisted Magnetic Recording". In: *ASME 2017 Conference on Information Storage and Processing Systems collocated with the ASME 2017 Conference on Information Storage and Processing Systems*. American Society of Mechanical Engineers. 2017, V001T01A002. DOI: 10.1115/ISPS2017-5411.

[54] Yueqiang Hu et al. "Head flying characteristics in heat assisted magnetic recording considering various nanoscale heat transfer models". In: *Journal of Applied Physics* 123.3 (2018), p. 034303. DOI: 10.1063/1.5016873.

[55] Li Chen, David B Bogy, and Brian Strom. "Thermal dependence of MR signal on slider flying state". In: *IEEE Transactions on Magnetics* 36.5 (Sept. 2000), pp. 2486–2489. ISSN: 0018-9464. DOI: 10.1109/20.908482.

[56] Jia-Yang Juang and David B Bogy. "Air-bearing effects on actuated thermal pole-tip protrusion for hard disk drives". In: *Journal of Tribology* 129.3 (2007), pp. 570–578. DOI: 10.1115/1.2736456.

[57] Arvind Narayanaswamy and Gang Chen. "Thermal near-field radiative transfer between two spheres". In: *Phys. Rev. B* 77 (7 Feb. 2008), p. 075125. DOI: 10.1103/PhysRevB.77.075125.

[58] Sheng Shen, Arvind Narayanaswamy, and Gang Chen. "Surface Phonon Polaritons Mediated Energy Transfer between Nanoscale Gaps". In: *Nano Letters* 9.8 (2009), pp. 2909–2913. DOI: 10.1021/nl901208v.

[59] Bair V. Budaev and David B. Bogy. "Computation of radiative heat transport across a nanoscale vacuum gap". In: *Applied Physics Letters* 104.6 (2014), p. 061109. DOI: 10.1063/1.4865404.

[60] Bair V. Budaev and David B. Bogy. "Heat transport by phonon tunneling across layered structures used in heat assisted magnetic recording". In: *Journal of Applied Physics* 117.10 (2015), p. 104512. DOI: 10.1063/1.4914871.

[61] Bair V. Budaev and David B. Bogy. "On thermal radiation across nanoscale gaps". In: *Zeitschrift für angewandte Mathematik und Physik* 66.4 (Aug. 2015), pp. 2061–2068. ISSN: 1420-9039. DOI: 10.1007/s00033-015-0502-5.

[62] Haoyu Wu et al. "Nanoscale heat transfer in the head-disk interface for heat assisted magnetic recording". In: *Applied Physics Letters* 108.9 (2016), p. 093106. DOI: 10.1063/1.4943111.

[63] Haoyu Wu and David Bogy. "A Numerical Study of the Nanoscale Heat Transfer in the Head-Disk Interface for Heat Assisted Magnetic Recording". In: *ASME 2016 Conference on Information Storage and Processing Systems*. American Society of Mechanical Engineers. 2016, V001T01A003. DOI: 10.1115/ISPS2016-9518.

[64] Norio Tagawa, Hiroshi Tani, and Kenji Ueda. "Experimental Investigation of Local Temperature Increase in Disk Surfaces of Hard Disk Drives Due to Laser Heating During Thermally Assisted Magnetic Recording". In: *Tribology Letters* 44.1 (July 2011), p. 81. ISSN: 1573-2711. DOI: 10.1007/s11249-011-9830-6.

[65] Haoyu Wu et al. "Lubricant reflow after laser heating in heat assisted magnetic recording". In: *Journal of Applied Physics* 117.17 (2015), 17E310. DOI: 10.1063/1.4914073.

[66] Shaomin Xiong, Haoyu Wu, and David Bogy. "Lubricant depletion under various laser heating conditions in Heat Assisted Magnetic Recording (HAMR)". In: *Optical Data Storage 2014*. Vol. 9201. International Society for Optics and Photonics. 2014, p. 920109. DOI: 10.1117/12.2062071.

[67] Mohammad Soroush Ghahri Sarabi and David B. Bogy. "Simulation of the Performance of Various PFPE Lubricants Under Heat Assisted Magnetic Recording Conditions". In: *Tribology Letters* 56.2 (Nov. 2014), pp. 293–304. ISSN: 1573-2711. DOI: 10.1007/s11249-014-0409-x.

[68] S. Xiong and D. B. Bogy. "Investigation of the Local Temperature Increase for Heat Assisted Magnetic Recording (HAMR)". In: *IEEE Transactions on Magnetics* 50.4 (Apr. 2014), pp. 1–6. ISSN: 0018-9464. DOI: 10.1109/TMAG.2013.2290760.

[69] Ion-Hong Chao et al. "A coupled electromagnetic and thermal model for picosecond and nanometer scale plasmonic lithography process". In: *Journal of Micro and Nano-Manufacturing* 2.3 (2014), p. 031003. ISSN: 2166-0468. DOI: 10.1115/1.4027589.

[70] Yung-Kan Chen, Jinglin Zheng, and David B. Bogy. "Light contact and surfing state dynamics of air bearing sliders in hard disk drives". In: *Applied Physics Letters* 100.24 (2012), p. 243104. DOI: 10.1063/1.4729055.

[71] Yung-Kan Chen et al. "Angstrom Scale Wear of the Air-Bearing Sliders in Hard Disk Drives". In: *Tribology Letters* 54.3 (June 2014), pp. 273–278. ISSN: 1573-2711. DOI: 10.1007/s11249-014-0307-2.

[72] Nan Zhou, Luis M Traverso, and Xianfan Xu. "Power delivery and self-heating in nanoscale near field transducer for heat-assisted magnetic recording". In: *Nanotechnology* 26.13 (2015), p. 134001. DOI: 10.1088/0957-4484/26/13/134001. URL: http://stacks.iop.org/0957-4484/26/i=13/a=134001.

[73] Haoyu Wu and David Bogy. "Use of an embedded contact sensor to study nanoscale heat transfer in heat assisted magnetic recording". In: *Applied Physics Letters* 110.3 (2017), p. 033104. DOI: 10.1063/1.4974304.

[74] Haoyu Wu and David Bogy. "A Heat Transfer Study in the Head Disk Interface and an Insight to Heat Assisted Magnetic Recording Design". In: *ASME 2017 Conference on Information Storage and Processing Systems collocated with the ASME 2017 Conference on Information Storage and Processing Systems*. American Society of Mechanical Engineers. 2017, V001T01A007. DOI: 10.1115/ISPS2017-5430.

[75] Masaru Furukawa et al. "Temperature Study of Embedded Contact Sensor for HDDS by Using Scanning Thermal Microscopy". In: *ASME 2014 Conference on Information Storage and Processing Systems*. American Society of Mechanical Engineers. 2014, V001T01A009. ISBN: 978-0-7918-4579-0. DOI: 10.1115/ISPS2014-6935.

[76] Y. Ma et al. "Controlled heat flux measurement across a closing nanoscale gap and its comparison to theory". In: *Applied Physics Letters* 108.21 (2016), p. 213105. DOI: 10.1063/1.4952449.

[77] Jia-Yang Juang. "Transient Characteristics of Nanoscale Air Bearings Subjected to Joule Heating". In: *Tribology Letters* 53.1 (Jan. 2014), pp. 255–260. ISSN: 1573-2711. DOI: 10.1007/s11249-013-0263-2.

[78] Y. Ma et al. "Measurement and Simulation of Nanoscale Gap Heat Transfer Using a Read/Write Head With a Contact Sensor". In: *IEEE Transactions on Magnetics* 53.2 (Feb. 2017), pp. 1–5. ISSN: 0018-9464. DOI: 10.1109/TMAG.2016.2604209.

[79] Joanna Bechtel Dahl. "Heat Assisted Magnetic Recording Head-Disk Interface: Numerical Simulation of Air Bearing and Lubricant Mechanics". PhD thesis. University of California, Berkeley, 2013. ISBN: 9781303832833.

[80] J. Aoyama et al. "A Head Cleaning Procedure for Heat-Assisted Magnetic Recording". In: *IEEE Transactions on Magnetics* 53.11 (Nov. 2017), pp. 1–4. ISSN: 0018-9464. DOI: 10.1109/TMAG.2017.2706981.

[81] Marchon Bruno. "Thin-Film Media Lubricants: Structure, Characterization, and Performance". In: *Developments in Data Storage*. Wiley-Blackwell, 2011. Chap. 8, pp. 144–166. ISBN: 9781118096833. DOI: 10.1002/9781118096833.ch8.

[82] S. Xiong and D. B. Bogy. "Experimental Study of Head-Disk Interface in Heat-Assisted Magnetic Recording". In: *IEEE Transactions on Magnetics* 50.3 (Mar. 2014), pp. 148–154. ISSN: 0018-9464. DOI: 10.1109/TMAG.2013.2287696.

[83] Joanna Bechtel Dahl and David B. Bogy. "Lubricant Flow and Evaporation Model for Heat-Assisted Magnetic Recording Including Functional End-Group Effects and Thin Film Viscosity". In: *Tribology Letters* 52.1 (Oct. 2013), pp. 27–45. ISSN: 1573-2711. DOI: 10.1007/s11249-013-0190-2.

[84] Steven W Meeks, Walter E Weresin, and Hal J Rosen. "Optical surface analysis of the head-disk-interface of thin film disks". In: *Journal of Tribology* 117.1 (1995), pp. 112–118. DOI: 10.1115/1.2830584.

[85] B. Marchon et al. "The physics of disk lubricant in the continuum picture". In: *IEEE Transactions on Magnetics* 41.2 (Feb. 2005), pp. 616–620. ISSN: 0018-9464. DOI: 10.1109/TMAG.2004.838044.

[86] Alejandro Rodriguez Mendez and David B. Bogy. "Lubricant Flow and Accumulation on the Slider's Air-Bearing Surface in a Hard Disk Drive". In: *Tribology Letters* 53.2 (Feb. 2014), pp. 469–476. ISSN: 1573-2711. DOI: 10.1007/s11249-013-0285-9.

[87] T.E. Karis et al. "Lubricant Spin-Off from Magnetic Recording Disks". In: *Tribology Letters* 11.3 (Nov. 2001), pp. 151–159. ISSN: 1573-2711. DOI: 10.1023/A:1012553415639.

[88] Mark Re. *HAMR: the Next Leap Forward is Now*. [Online; accessed 7-May-2018]. URL: https://blog.seagate.com/craftsman-ship/hamr-next-leap-forward-now/.